

Master thesis and internship[BR]- Master's thesis : Design of a coaxial counter-rotating rotor for an emergency drone[BR]- Internship

Auteur : Shebli, Rami

Promoteur(s) : Hillewaert, Koen

Faculté : Faculté des Sciences appliquées

Diplôme : Master en ingénieur civil en aérospatiale, à finalité spécialisée en "aerospace engineering"

Année académique : 2023-2024

URI/URL : <http://hdl.handle.net/2268.2/20867>

Avertissement à l'attention des usagers :

Tous les documents placés en accès ouvert sur le site le site MatheO sont protégés par le droit d'auteur. Conformément aux principes énoncés par la "Budapest Open Access Initiative"(BOAI, 2002), l'utilisateur du site peut lire, télécharger, copier, transmettre, imprimer, chercher ou faire un lien vers le texte intégral de ces documents, les disséquer pour les indexer, s'en servir de données pour un logiciel, ou s'en servir à toute autre fin légale (ou prévue par la réglementation relative au droit d'auteur). Toute utilisation du document à des fins commerciales est strictement interdite.

Par ailleurs, l'utilisateur s'engage à respecter les droits moraux de l'auteur, principalement le droit à l'intégrité de l'oeuvre et le droit de paternité et ce dans toute utilisation que l'utilisateur entreprend. Ainsi, à titre d'exemple, lorsqu'il reproduira un document par extrait ou dans son intégralité, l'utilisateur citera de manière complète les sources telles que mentionnées ci-dessus. Toute utilisation non explicitement autorisée ci-avant (telle que par exemple, la modification du document ou son résumé) nécessite l'autorisation préalable et expresse des auteurs ou de leurs ayants droit.



MASTER'S THESIS SUBMITTED IN PARTIAL FULFILLMENT OF THE REQUIREMENTS FOR THE DEGREE OF
MASTER OF SCIENCE IN AEROSPACE ENGINEERING PRESENTED BY:

RAMI SHEBLI

UNIVERSITY OF LIÈGE - FACULTY OF APPLIED SCIENCES

Design of a coaxial counter-rotating rotor for an emergency drone

Thesis supervisors

Professor Koen Hillewaert
University of Liège

Christophe Greffe
GeneriX

Jury members

Professor Koen Hillewaert, Christophe Greffe, Professor Gregoris Dimitriadis

Liège, Academic year 2023-2024

Abstract

The design and optimization of coaxial rotors are crucial for enhancing the performance and efficiency of aerial vehicles, particularly in applications requiring high thrust-to-weight ratios and precise control. This thesis aimed to optimize the aerodynamic performance of coaxial rotor blades by refining their geometry, focusing on the modification of twist and chord distributions.

Initially, in this research, ROTARE, a BEMT code developed by PhD candidate Thomas Lambert, was validated for single-rotor analysis, forming a strong foundation for the validation of the coaxial rotor case and confirming the reliability of ROTARE for the optimization process. The study then progressed through two main optimization phases. In the first phase, the optimal operating conditions—specifically the combination of RPM and collective pitch of the upper and lower rotors—were identified to achieve a target thrust of 6 kg and a thrust to power ratio T/P of approximately 12.5 g/W without altering the blade geometry. This phase involved systematic sweeps and iterative adjustments to maximize rotor efficiency.

The second phase focused on geometry optimization, where both the twist and chord distributions were independently optimized. The twist optimization led to a 4% improvement in the thrust-to-power ratio, but this gain was not considered significant. Similarly, the chord optimization alone did not yield significant performance improvements. The detailed analysis revealed that these strategies, when applied in isolation, were insufficient to achieve major gains in efficiency.

The study was conducted on four real-life blades, SAB280, ALZRC325, ALZRC380, and BL450, which are usually used for drone applications, with the ALZRC380mm blade emerging as the most efficient. The ALZRC380mm blade achieved a thrust-to-power ratio of approximately 15 g/W at a thrust of 6 kg, outperforming the other blades, which achieved T/P between 11 g/W and 12.5 g/W. This superior performance is attributed to the ALZRC380mm blade's larger chord length and increased overall blade length, enhancing lift generation and improving the lift-to-drag ratio.

The analysis was applied in detail to the SAB280 blade, covering upper rotor rotational speeds ranging from 500 to 6000 RPM and collective pitches between 1° and 17° . The optimal configuration of the SAB280mm blade, which achieves a thrust of 6 kg and a T/P of 11 g/W that is below the target value, was determined at an upper rotor rotation speed of 3000 RPM and a collective pitch of 13° , paired with a lower rotor rotation speed of approximately 2600 RPM and a collective pitch of approximately 18.5° . It turned out that all blades achieved their c_T/c_P ratio and T/P peak at upper collective pitch angle values approximately between 4° and 5° .

It turned out that while the twist and chord optimizations provided small improvements, their combination would ensure significant performance gains. This approach, particularly when aligned with a well-defined thrust distribution strategy could lead to an optimal chord distribution that, when combined with an optimized twist, enhances overall rotor performance. This research opens avenues for further exploration, including integrating multiple airfoil profiles along the blade span and developing simpler, more cost-effective manufacturing approaches.

Keywords: Coaxial rotors, ROTARE, optimization, blade geometry, twist distribution, chord distribution, thrust efficiency, airfoil profiles, rotor performance.

Acknowledgments

I would like to express my deepest gratitude to my advisors, Prof. Koen Hillewaert and Mr. Christophe Greffe, for their steady support, guidance, and invaluable mentorship throughout my research journey. Their profound expertise, patience, and encouragement have been pivotal in my academic growth, pushing me to achieve this complete work. I am sincerely grateful for their instrumental role in enabling me to investigate into and explore this subject.

I would also like to extend my thanks to Thomas Lambert, PhD candidate in Aerospace Engineering at the University of Liège, for his support and guidance during my internship. His assistance has significantly contributed to several key results of my research. His insights and expertise were invaluable.

Additionally, I would like to take this opportunity to acknowledge the contributions of all the teachers, professors, and teaching assistants I have encountered along the way. I am humbled and immensely grateful for their support, guidance, and encouragement, which have been crucial in shaping the outcome of this master dissertation. Their dedication to education and mentorship has left a lasting impact on my academic journey.

Last but not least, I extend my deepest thanks to my friends, family, and loved ones for their love and support. Their constant encouragement and inspiration have played a crucial role in the completion of this work. I am truly grateful to everyone who has helped me achieving this, especially as it has been my goal since I arrived in Belgium back in 2015. I am humbly proud of myself and deeply thankful to everyone, as I never imagined I could achieve this without their support.

Nomenclature

Acronyms

APC	Advanced Precision Composites
BEMT	Blade Element Momentum Theory
BET	Blade Element Theory
CFD	Computational Fluid Dynamics
MST	Multiple Stream Tubes
MT	Momentum Theory
NACA	National Advisory Committee for Aeronautics
RPM	Revolutions Per Minute
SMST	Simplified Multiple Stream Tubes
UAV	Unmanned Aerial Vehicle
UIUC	University of Illinois at Urbana-Champaign

Subscripts

$()_0$	Upstream of the rotor
$()_{1+}$	Just below the rotor disk
$()_{1-}$	Just above the rotor disk
$()_1$	At the rotor disk
$()_\infty$	Far wake
$()_A$	Axial direction
$()_{l,0}$	Upstream of the lower rotor
$()_l$	Lower rotor
$()_R$	Radial direction
$()_T$	Tangential direction

$()_{u,1}$	At the upper rotor disk
$()_{u,\infty}$	Wake below the upper rotor
$()_u$	Upper rotor
$()_x$	Direction along the chord
$()_{y_{\text{hub}}}$	At the rotor hub
$()_z$	Direction perpendicular to the chord

Symbols

α	Angle of attack
α_0	Zero-lift angle
χ	Twist angle
\dot{m}	Mass flow rate
η	Efficiency
κ	Contraction ratio
Ω	Angular velocity
ω	Rotational speed
ϕ	Inflow angle
ρ	Air density
θ	Collective pitch angle
c	Chord length
c_d	Drag coefficient
c_l	Lift coefficient
c_m	Moment coefficient
c_p	Power coefficient
c_T	Thrust coefficient
D	Propeller diameter
dD	Incremental drag
dF_x	Force component in the x-direction
dF_z	Force component in the z-direction

dL	Incremental lift
dM	Incremental pitching moment
dP	Incremental power
dQ	Incremental torque
dT	Incremental thrust
F	Prandtl's loss factor
J	Advance ratio
K_P	Power correction factor
K_T	Thrust correction factor
N	Number of blades
n	Rotational speed (revolutions per second)
N_{crit}	Critical amplification factor
N_{rot}	Rotational speed in revolutions persecond
P	Total power
Q	Total torque
R	Outer radius of the blade
r	Radial position along the blade
R_0	Inner radius of the blade
Re	Reynolds number
T	Total thrust
U	Resultant velocity
U_A	Axial component of resultant velocity
u_i	Swirl induced velocity
U_R	Radial component of resultant velocity
U_T	Tangential component of resultant velocity
V	Forward speed
v_i	Induced velocity
V_∞	Free stream velocity
y	Radial distance from the rotational axis
PANE	Number of panels in XFOIL analysis

List of Figures

1.1	Early aircraft models using coaxial rotor system.	2
1.2	Kamov helicopter design evolution.	3
1.3	Ingenuity NASA Mars Helicopter[27].	4
2.1	Forces, angles, and velocities acting on a blade section. Adapted from [36]	12
2.2	Streamtube of the flow over a rotor disk.	13
2.3	Flow model of a rotor in hovering flight. Adapted from [37]	15
2.4	Flow model used for the BEMT analysis of a coaxial rotor system with the lower rotor operating in the slipstream of the upper rotor. Adapted from [38]	22
2.5	Velocities in the multiple stream tubes model for coaxial rotors. Adapted from [32].	23
2.6	Representation of the detailed radii and width used in the calculation of the tube radius. Adapted from [32]	25
3.1	Photo showing the APC propellers tested.	33
3.2	Comparison of the quality of polars for NACA 4412 at various Reynolds numbers, using two different N_{crit} values.	34
3.3	Comparison of power and thrust coefficients for APC 9x6E propeller using different solvers.	35
3.4	Comparison of ROTARE predictions and UIUC measurements for the APC 9x6E propeller in the operational conditions at $Re = [5e4, 1e6]$ and $RPM = 4000$	37
3.5	Comparison of ROTARE predictions and UIUC measurements for the APC 9x6E propeller in the static case at $J = 0$	38
3.6	Comparison of ROTARE predictions, UIUC measurements, and results from a BEMT code in the literature [28] for the APC 14x12E propeller in the operational conditions at $Re = [5e4, 1e6]$ and $RPM = 3500$	39
3.7	Comparison of ROTARE predictions with experimental data from Biermann et al.[14] for the ClarkY airfoil at different pitch angles, $\theta = [15^\circ - 45^\circ]$	41
4.1	Configuration set-up of the simulated blade.	44
4.2	SAB 280mm blade and its corresponding airfoil shape, Selig S8035.	45
4.3	Flowchart of the optimization process.	46
4.4	Flowchart summarizing the steps for achieving torque cancellation between the upper and lower rotors.	48
4.5	Lower rotor collective pitch angle variation for the SAB 280mm blade. Blade parameters: $L = 280\text{ mm}$, $c = 25\text{ mm}$, airfoil: Selig S8035, $r_0 = 100\text{ mm}$, $r_{end} = 290\text{ mm}$	56

4.6	Lower rotor RPM variation for the SAB 280mm blade. Blade parameters: $L = 280$ mm, $c = 25$ mm, airfoil: Selig S8035, $r_0 = 100$ mm, $r_{\text{end}} = 290$ mm.	57
4.7	RPM ratio variation for the SAB 280mm blade. Blade parameters: $L = 280$ mm, $c = 25$ mm, airfoil: Selig S8035, $r_0 = 100$ mm, $r_{\text{end}} = 290$ mm.	58
4.8	Variation of c_T/c_P and T/P for the SAB 280mm blade. Blade parameters: $L = 280$ mm, $c = 25$ mm, airfoil: Selig S8035, $r_0 = 100$ mm, $r_{\text{end}} = 290$ mm.	58
4.9	Total thrust coefficient c_T variation for the SAB 280mm blade. Blade parameters: $L = 280$ mm, $c = 25$ mm, airfoil: Selig S8035, $r_0 = 100$ mm, $r_{\text{end}} = 290$ mm.	59
4.10	Total power coefficient c_P variation for the SAB 280mm blade. Blade parameters: $L = 280$ mm, $c = 25$ mm, airfoil: Selig S8035, $r_0 = 100$ mm, $r_{\text{end}} = 290$ mm.	60
4.11	Variation of total thrust generation and total power consumption for the SAB 280mm blade. Blade parameters: $L = 280$ mm, $c = 25$ mm, airfoil: Selig S8035, $r_0 = 100$ mm, $r_{\text{end}} = 290$ mm.	61
4.12	Thrust generation and power consumption for the SAB 280mm blade. Blade parameters: $L = 280$ mm, $c = 25$ mm, airfoil: Selig S8035, $r_0 = 100$ mm, $r_{\text{end}} = 290$ mm.	62
4.13	Thrust-to-power ratio T/P for the SAB 280mm blade at $\theta_{\text{upper}} = 1^\circ - 17^\circ$. Blade parameters: $L = 280$ mm, $c = 25$ mm, airfoil: Selig S8035, $r_0 = 100$ mm, $r_{\text{end}} = 290$ mm.	63
4.14	Thrust-to-power ratio T/P variation for the ALZRC380 blade. Blade parameters: $L = 380$ mm, $c = 33.5$ mm, airfoil: St. CYR 172 (Royer), $r_0 = 100$ mm, $r_{\text{end}} = 480$ mm.	65
4.15	c_T/c_P as a function of upper rotor collective pitch angle for the ALZRC380 blade at $[RPM = 500 - 6000]$. Blade parameters: $L = 380$ mm, $c = 33.5$ mm, airfoil: St. CYR 172 (Royer), $r_0 = 100$ mm, $r_{\text{end}} = 480$ mm.	65
5.1	Polars of the airfoil Selig S8035 for the SAB280mm blade. Blade fixed parameters: $c = 25$ mm, blade length $L = 280$ mm, $r_0 = 100$ mm, and $r_{\text{end}} = 290$ mm.	68
5.2	Velocity triangle of the blade element for the SAB280mm blade. Blade fixed parameters: $c = 25$ mm, blade length $L = 280$ mm, $r_0 = 100$ mm, and $r_{\text{end}} = 290$ mm.	68
5.3	Flow chart of the twist optimization process.	70
5.4	Twist distribution for the SAB280mm blade at $RPM_{\text{upper}} = 3000$, $\theta_{\text{upper}} = 13^\circ$, $RPM_{\text{lower}} = 2600$ and $\theta_{\text{lower}} = 18.5^\circ$. Blade fixed parameters: $c = 25$ mm, blade length $L = 280$ mm, $r_0 = 100$ mm, and $r_{\text{end}} = 290$ mm, featuring a Selig S8035 airfoil.	71
5.5	Local dT/dP vs. span for the SAB280mm blade at $RPM_{\text{upper}} = 3000$, $\theta_{\text{upper}} = 13^\circ$, $RPM_{\text{lower}} = 2600$ & $\theta_{\text{lower}} = 18.5^\circ$ (Non-twisted), $RPM_{\text{lower}} = 2500$ & $\theta_{\text{lower}} = 16.4^\circ$ (Twisted). Blade fixed parameters: $c = 25$ mm, blade length $L = 280$ mm, $r_0 = 100$ mm, and $r_{\text{end}} = 290$ mm, featuring a Selig S8035 airfoil.	72
5.6	Local thrust, power, and drag vs. span for the SAB280mm blade at $RPM_{\text{upper}} = 3000$, $\theta_{\text{upper}} = 13^\circ$, $RPM_{\text{lower}} = 2600$ & $\theta_{\text{lower}} = 18.5^\circ$ (Non-twisted), $RPM_{\text{lower}} = 2500$ & $\theta_{\text{lower}} = 16.4^\circ$ (Twisted). Blade fixed parameters: $c = 25$ mm, blade length $L = 280$ mm, $r_0 = 100$ mm, and $r_{\text{end}} = 290$ mm, featuring a Selig S8035 airfoil.	73
5.7	Local aerodynamics for the SAB280mm blade at $RPM_{\text{upper}} = 3000$, $\theta_{\text{upper}} = 13^\circ$, $RPM_{\text{lower}} = 2600$ & $\theta_{\text{lower}} = 18.5^\circ$ (Non-twisted), $RPM_{\text{lower}} = 2500$ & $\theta_{\text{lower}} = 16.4^\circ$ (Twisted). Blade fixed parameters: $c = 25$ mm, blade length $L = 280$ mm, $r_0 = 100$ mm, and $r_{\text{end}} = 290$ mm, featuring a Selig S8035 airfoil.	74
5.8	Performance improvement with twist for the SAB280mm blade. Blade fixed parameters: $c = 25$ mm, $L = 280$ mm, $r_0 = 100$ mm, and $r_{\text{end}} = 290$ mm, featuring a Selig S8035 airfoil.	75

5.9	Performance improvement with twist for the SAB280mm blade. Blade fixed parameters: $c = 25$ mm, blade length $L = 280$ mm, $r_0 = 10$ cm, and $r_{\text{end}} = 290$ mm, featuring a Selig S8035 airfoil. The numbers 1 to 17 on the curves correspond to the collective pitch angles θ_{upper} of the upper rotor.	76
5.10	Comparison for different chord values at constant chord for the SAB280mm blade. Blade fixed parameters: $c = 25$ mm and $c = 40$ mm, blade length $L = 280$ mm, $r_0 = 100$ mm, and $r_{\text{end}} = 290$ mm, featuring a Selig S8035 airfoil.	78
5.11	Effect of chord linear tapering on performance at $RPM = 3000$ for the SAB280mm blade. Blade fixed parameters: $c_{\text{root}} = 30$ mm, $c_{\text{tip}} = 15$ mm, $L = 280$ mm, $r_0 = 100$ mm, and $r_{\text{end}} = 290$ mm, featuring a Selig S8035 airfoil.	79
A.1	Blade SAB 280 mm [6] and closest airfoil shape S8035 [9].	85
A.2	Blade BL450 325 mm [31] and closest airfoil shape Gottingen GOE 411 [8].	86
A.3	Blade ALZRC 325 mm [5] and closest airfoil shape Eppler E171 [7].	86
A.4	Blade ALZRC 380 mm [4] and closest airfoil shape St. CYR 172 [10].	87
B.1	Variation of c_T/c_P and T/P with upper rotor collective pitch for the BL450 325mm blade. Blade parameters: $L = 325$ mm, $c = 32$ mm, airfoil: Gottingen GOE 411, $r_0 = 100$ mm, $r_{\text{end}} = 425$ mm.	92
B.2	Thrust-to-power ratio T/P for the BL450 325mm blade at $\theta_{\text{upper}} = 1^\circ - 17^\circ$. Blade parameters: $L = 325$ mm, $c = 32$ mm, airfoil: Gottingen GOE 411, $r_0 = 100$ mm, $r_{\text{end}} = 425$ mm.	93
B.3	c_T/c_P and T/P variation for the BL450 blade with twisted blade configuration. Blade parameters: $L = 325$ mm, $c = 32$ mm, airfoil: Gottingen GOE 411, $r_0 = 100$ mm, $r_{\text{end}} = 425$ mm.	94
B.4	Performance improvement with twisted blade configuration for the BL450 325mm blade. Blade parameters: $L = 325$ mm, $c = 32$ mm, airfoil: Gottingen GOE 411, $r_0 = 100$ mm, $r_{\text{end}} = 425$ mm. The numbers 1 to 17 on the curves correspond to the collective pitch angles θ_{upper} of the upper rotor.	95
B.5	c_T/c_P and T/P variations for the ALZRC 325mm blade. Blade parameters: $L = 325$ mm, $c = 32.5$ mm, airfoil: Eppler E171, $r_0 = 100$ mm, $r_{\text{end}} = 425$ mm.	96
B.6	Thrust-to-power ratio T/P for the ALZRC 325mm blade at $\theta_{\text{upper}} = 1^\circ - 17^\circ$. Blade parameters: $L = 325$ mm, $c = 32.5$ mm, airfoil: Eppler E171, $r_0 = 100$ mm, $r_{\text{end}} = 425$ mm.	97
B.7	c_T/c_P and T/P variation for the ALZRC 325mm blade with twisted blade configuration. Blade parameters: $L = 325$ mm, $c = 32.5$ mm, airfoil: Eppler E171, $r_0 = 100$ mm, $r_{\text{end}} = 425$ mm.	98
B.8	Performance improvement with twisted blade configuration for the ALZRC 325mm blade. Blade parameters: $L = 325$ mm, $c = 32.5$ mm, airfoil: Eppler E171, $r_0 = 100$ mm, $r_{\text{end}} = 425$ mm. The numbers 1 to 17 on the curves correspond to the collective pitch angles θ_{upper} of the upper rotor.	99
B.9	c_T/c_P and T/P variation for the ALZRC 380mm blade. Blade parameters: $L = 380$ mm, $c = 33.5$ mm, airfoil: St. CYR 172 (Royer), $r_0 = 100$ mm, $r_{\text{end}} = 480$ mm.	100
B.10	Thrust-to-power ratio T/P variation for the ALZRC 380mm blade at $\theta_{\text{upper}} = 1^\circ - 17^\circ$. Blade parameters: $L = 380$ mm, $c = 33.5$ mm, airfoil: St. CYR 172 (Royer), $r_0 = 100$ mm, $r_{\text{end}} = 480$ mm.	101

B.11 c_T/c_P and T/P variation for the ALZRC 380mm blade with twisted blade configuration. Blade parameters: $L = 380$ mm, $c = 33.5$ mm, airfoil: St. CYR 172 (Royer), $r_0 = 100$ mm, $r_{\text{end}} = 480$ mm.	102
B.12 Performance improvement with twisted blade configuration for the ALZRC 380mm blade. Blade parameters: $L = 380$ mm, $c = 33.5$ mm, airfoil: St. CYR 172 (Royer), $r_0 = 100$ mm, $r_{\text{end}} = 480$ mm. The numbers 1 to 17 on the curves correspond to the collective pitch angles θ_{upper} of the upper rotor.	103

List of Tables

2.1	Thrust, moment, and power coefficients definitions for helicopter rotor applications expressed in the US and international conventions.	19
2.2	Comparison between ROTARE’s solvers [32].	28
3.1	Thrust, power, and torque coefficients definitions for helicopter rotor and propeller applications expressed in US convention.	32
B.1	Summary of the RPM and collective pitch variations for the upper and lower rotors across the full range of configurations for the blade SAB280.	88

Contents

1	Introduction	2
1.1	History	2
1.2	Motivations	4
1.3	Outline of the thesis	5
2	Theoretical Background	7
2.1	Blade Element Momentum Theory	7
2.1.1	Blade Element Theory (BET)	10
2.1.2	Momentum Theory (MT)	13
2.2	Extension to Coaxial Rotor Model	21
2.2.1	Flow Model	21
2.3	Numerical Implementation	27
2.3.1	ROTARE Software	27
2.3.2	Solver	28
3	Validation of ROTARE	31
3.1	Comparison with UIUC propeller measurements	31
3.1.1	Results	35
3.2	Comparison with <i>Clark Y</i> propellers measurements	40
3.2.1	Results	40
3.3	Conclusion	42
4	Optimal design point	43
4.1	Introduction	43
4.2	Blade configuration Set-up	44
4.3	Strategy	45
4.3.1	Torque cancellation	46
4.3.2	Non-Dimensionalization	48
4.3.3	Systematic Sweep	49
4.3.4	Exact rotor configuration	51
4.3.5	Similitude method	52
4.4	Implementation	55
4.5	Results	55
4.5.1	Variation of θ_{lower} with $\text{RPM}_{\text{upper}}$ and θ_{upper}	55
4.5.2	Variation of $\text{RPM}_{\text{lower}}$ with $\text{RPM}_{\text{upper}}$ and θ_{upper}	56

4.5.3	Analysis of c_T/c_P and T/P Curves	57
4.5.4	Thrust and Power Distribution	60
4.5.5	T/P vs. Thrust	62
4.6	Conclusion	63
5	Geometry optimization	66
5.1	Introduction	66
5.2	Strategy	67
5.2.1	Introduction of twist in the blade airfoil	67
5.2.2	Results	70
5.2.3	Chord distribution of the blade	76
6	Conclusion	81
6.1	Further perspectives and future improvement suggestions	83
6.1.1	Optimal thrust distribution strategy	83
6.1.2	Integration of multiple airfoil profiles	83
6.1.3	Fixed pitch between upper and lower rotors	84
A	Appendix	85
B	Results	88
	Bibliography	104

Chapter 1

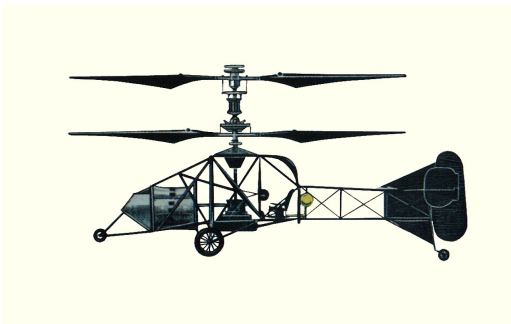
Introduction

1.1 History

The history of coaxial rotor systems can be traced back to the early 20th century when pioneering aviators began experimenting with innovative helicopter designs. The concept of coaxial rotors, however, is older than these developments, as it was first proposed by the Russian engineer Mikhail Lomonosov in 1754. Lomonosov's preliminary concepts established the foundation for the evolution of rotorcraft technology, although the practical realization of these ideas would not emerge until much later [43].

In the 1930s, notable advancements were achieved by two pioneering engineers, Igor Sikorsky, a Russian-born engineer, and Louis Breguet, a French engineer. Both engineers developed prototypes featuring coaxial rotors, with the objective of addressing the issue of torque imbalance associated with single-rotor helicopters. The utilization of two counter-rotating rotors mounted on the same axis effectively negated the necessity for a tail rotor in these pioneering designs. This innovation resulted in enhanced stability and control, representing a significant advancement in the field of helicopter engineering technology [37], [46].

During the 1940s, further advancements in coaxial rotor technology were made by pioneers such as Stanley Hiller. Hiller's Hiller XH-44, developed during this period, utilized coaxial rotors to create a compact and efficient helicopter design. The Hiller XH-44 was instrumental in demonstrating the practical benefits of coaxial rotors, paving the way for future developments in both military and civilian rotorcrafts [44].



(a) Breguet-Dorand Gyroplane [45].



(b) Hiller XH-44 [44].

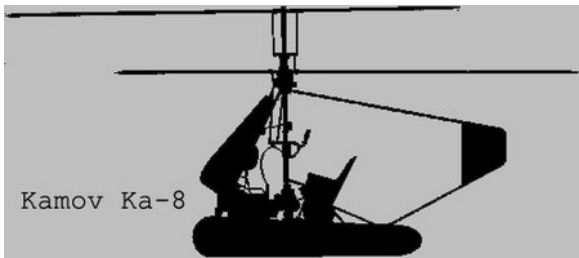
Figure 1.1: Early aircraft models using coaxial rotor system.

In the same decade, the Kamov Design Bureau in the Soviet Union made significant contributions to the de-

velopment of coaxial helicopters. During World War II, Kamov produced the Ka-8 and later the Ka-10, which showcased the practicality and efficiency of the coaxial rotor configuration. These models were among the first to be produced in significant numbers and used operationally, further proving the viability of coaxial rotors in various applications [24].

The Ka-8, a single-seat helicopter designed for light observation, and the Ka-10, an improved version with enhanced performance and reliability, were crucial in establishing the coaxial rotor as a fundamental component of 20th-century helicopter design. The success of these models demonstrated the advantages of coaxial rotors, including enhanced lift capacity, stability, and maneuverability in confined spaces. Such characteristics made them especially well-suited to naval operations, where spatial limitations are a crucial factor [54].

As technology advanced, the Kamov Design Bureau continued to refine coaxial rotor systems, leading to the development of more sophisticated models like the Kamov Ka-27 and Ka-52. These helicopters have been widely used in both military and civilian roles, benefiting from the unique advantages provided by coaxial rotors. The Ka-27 is distinguished by its reputation for excellence in anti-submarine warfare and its capacity to operate from modest naval vessels. The Ka-52 "Alligator" is celebrated for its combat effectiveness and adaptability [2],[3].



(a) Ka-8 [54].



(b) Ka-10 [12].



(c) Ka-27 [2].



(d) Ka-52 [3].

Figure 1.2: Kamov helicopter design evolution.

1.2 Motivations

In recent years, coaxial rotor systems have found applications beyond traditional helicopters. They are now widely used in unmanned aerial vehicles (UAVs) due to their compact size, stability, and efficiency. The NASA Mars Helicopter Ingenuity (See Figure 1.3), for example, employs a coaxial rotor design to navigate the thin Martian atmosphere. This innovative use of coaxial rotors highlights their adaptability and the ongoing relevance of this technology in cutting-edge aerospace applications. As just mentioned, many companies have explored the use of drones or Unmanned Aerial Vehicles (UAVs) for package delivery, aerial surveying, and military applications. A significant challenge for rotary-winged drones is determining the optimal components for specific applications [25]. The configuration of propellers and motors varies according to mission requirements, with differences in number, positioning, and selection. Coaxial rotors, defined as a pair of counter-rotating rotors rotating about a common shaft axis, offer several advantages that are particularly relevant for UAVs [37].

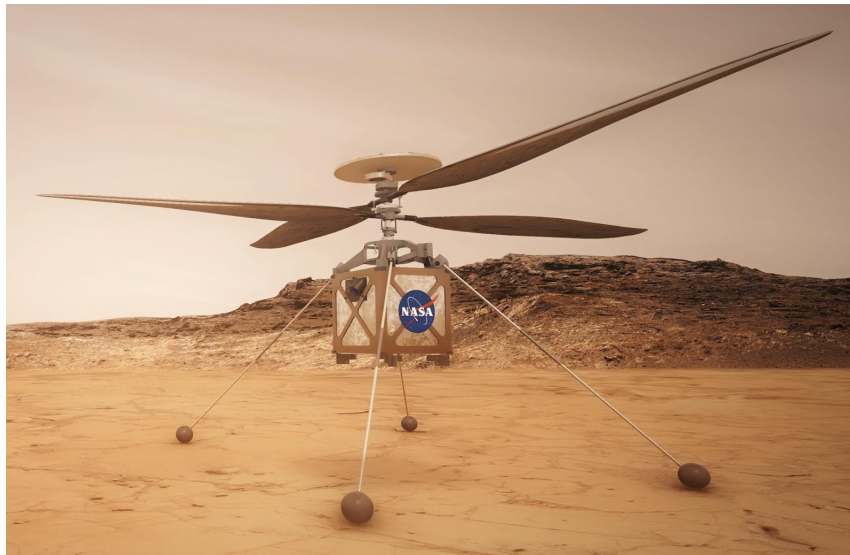


Figure 1.3: Ingenuity NASA Mars Helicopter[27].

Coaxial drones are a promising alternative to small UAVs due to their potential to overcome limitations, particularly in terms of energy efficiency and performance. The coaxial configuration allows for increased lift and thrust efficiency, which can lead to improved endurance and payload capacity. Additionally, the compact design of coaxial drones makes them suitable for operations in confined spaces and urban environments where space is limited. Their ability to reduce drag and improve aerodynamic performance further enhances their viability for a wide range of applications, from commercial to military use. As research and development in this area continue, coaxial drones are expected to play an increasingly significant role in the future of UAV technology.

Finally, an additional advantage of the counter-rotating coaxial rotor system lies in the fact of eliminating the need for a tail rotor used for anti-torque purposes, it allows all power to be directed toward generating useful vertical lift and enhancing performance. This design also reduces the overall rotor size, as each rotor contributes to vertical thrust. However, the interaction between the two rotors and their wakes creates a more complex flow field compared to a single rotor system. These benefits highlight the advantages of coaxial rotors in improving lift and performance efficiency [37].

1.3 Outline of the thesis

Observation drones have predominantly adopted the quadrotor design due to its simplicity of construction and ease of control. However, inherent limitations in performance and endurance persist with quadrotors. This research investigates the potential of coaxial contrarotating variable pitch rotors, similar to helicopter designs, which offer the promise of significantly improved drone performance and endurance.

Coaxial rotor systems present significant advantages, including compactness and ease of deployment (e.g., tube launch methods). However, optimizing blade design and control mechanisms for optimal efficiency remains a critical challenge due to the complexity of interactions between the upper and lower propellers. These interactions complicate theoretical models that often rely on simplified blade geometries. While some progress has been made in propeller characterization, further research is needed to fully understand the effects of various propeller parameters. Addressing these challenges is crucial to fully unlocking the potential of coaxial drones in diverse applications.

Moreover, the design of coaxial rotors also addresses aerodynamic inefficiencies encountered by small UAV designers. The coaxial configuration allows for higher pitch angles on the advancing blades without compromising roll trim, thereby balancing lift between the upper and lower rotors [48].

Developing a system to automatically optimize the design of coaxial rotor-based UAVs for different mission requirements is highly valuable. The complex aerodynamics involved in coaxial configurations necessitate advanced computational models and extensive empirical testing to accurately predict and enhance performance. Therefore, addressing these challenges is crucial to fully unlocking the potential of coaxial drones in diverse applications.

The optimization will be conducted using a blade element momentum theory (BEMT) code called ROTARE [33], which is briefly introduced in section 2.3.1.

The first part of the research presents a theoretical background that summarizes the principles and concepts used to construct the BEMT code and clarifies theoretically how a coaxial system works and how it is interpreted.

The second part of the research presents the validation of the BEMT code, specifically focusing on a single rotor system using ROTARE. This validation includes comparing the performances obtained by ROTARE of several APC propellers with the experimental measurements of the University of Illinois at Urbana-Champaign (UIUC) for the same APC propellers. A further comparison is also done between the results obtained by ROTARE of a Clark Y propeller and experimental data of the same propeller obtained by Biermann et al.[14].

This research focuses on validating the BEMT code for a single rotor system. However, a complete validation, which is beyond the scope of this study, was thoroughly addressed in another master's thesis. The single rotor validation is included here only as part of the researcher's contribution. Additionally, the coaxial rotor system has been detailed and validated in a separate master's thesis. For more comprehensive insights, readers are encouraged to refer to Robin Tamburrini's thesis, dedicated to the validation of ROTARE, which will be published in September 2024

The third part of the research is dedicated to the strategies used for the optimization of the rotor blade's performance. This optimization process consists of two main parts. The first part seeks to identify the optimal design configuration of the upper and lower rotor blades for a desired thrust, without altering the blade

geometry.

The second part involves dynamic optimization, examining the impact of modifying the blade geometry, including twist and chord variations. This section aims to demonstrate the advantages and implications of these modifications on the aerodynamic performance of different blade types.

The optimization and performance computation will be conducted on real-life blades, the details of which can be found in *Appendix A*.

The blade element code's role in computing the performance of the coaxial rotor will significantly help in optimizing the coaxial drone's performance, which is the primary focus of this research.

Finally, this research aims to demonstrate the feasibility and advantages of using a validated blade element code to optimize the performance of coaxial rotor systems, particularly for emergency drone applications. The comprehensive approach to validation and optimization presented here will contribute to the broader understanding and development of efficient, high-performance UAVs equipped with coaxial rotor systems.

Chapter 2

Theoretical Background

2.1 Blade Element Momentum Theory

The Blade Element Momentum Theory (BEMT) is a hybrid analytical method initially developed for propellers by Weick [53]. This approach incorporates Froude's differential theory for single propellers in axial motion, with further contributions from Drzewiecki [19] and Tokaty [51]. Gessow [20] later adapted BEMT for analyzing single helicopter rotors, as detailed by Gessow and Myers [21], and Leishman [37] outlined the numerical aspects. BEMT has become a widely accepted method for helicopter rotor analysis in axial flight, though it has rarely been formalized for coaxial rotor systems, with Valkov [52] being one of the few exceptions.

Nowadays, BEMT is a well-established methodology for estimating the radial and azimuthal blade aerodynamic loading over the rotor disk, providing a comprehensive understanding of the complex flow interactions occurring in coaxial rotor systems. It is one of the most prevalent and preferred tools in rotor analysis and design. BEMT's versatility allows its application across various domains of rotating wing systems, including helicopters, propellers, wind turbines, and more [32].

A significant advantage of BEMT is its efficiency, as it is based on robust physical principles and relies minimally on empirical parameters, aside from airfoil section data. BEMT integrates two fundamental theories: Momentum Theory (MT) and Blade Element Theory (BET). While Momentum Theory alone does not offer sufficient detail for rotor blade design, Blade Element Theory facilitates the determination of forces acting on the rotor blades. Neither of these theories is sufficient independently; however, BEMT, by combining both MT and BET, provides a more comprehensive analysis. Moreover, BEMT is based on the principle of dividing rotor blades into smaller elements and individually analyzing the aerodynamic forces on each element. It assumes that blade elements operate within a 2D flow field, unaffected by adjacent elements and rotor annuli [37].

Several assumptions are made in BEMT application [37], [32], [26] :

1. The flow around the rotor is assumed to be in a steady state, with flow properties at any point remaining constant over time.
2. The flow is considered incompressible and inviscid, with negligible viscous shear between fluid elements.
3. The resulting flow field is assumed to be axisymmetric, implying uniform airflow and aerodynamic forces at every azimuth angle around the rotor disk.

Additionally, BEMT assumes a uniform inflow velocity across the rotor disk, disregarding non-uniformities

caused by other rotors such as in coaxial configurations, for example.

BEMT removes several assumptions required by MT, thereby enhancing its predictive power. It allows for the calculation of aerodynamic load distributions over the blades, estimates of non-ideal induced losses and tip losses, and the assessment of rotor-on-rotor interference effects without the need for prior specification, unlike MT [35], [34]. Moreover, the magnitudes of these losses vary with rotor operating conditions, such as net system thrust and thrust sharing between upper and lower rotors, rather than being scalable as assumed in simpler theories.

For coaxial rotor systems (Discussed in detail in section 2.2), the flow model, assumes that the lower rotor operates partially within the fully developed slipstream of the upper rotor, particularly in the vena contracta, where there is a maximum change in slipstream velocity before the wake flow reaches the lower rotor. Therefore, a primary challenge encountered in BEMT calculations concerns the accurate definition of the upstream velocity experienced by the lower rotor, which actually necessitates an evaluation of the contraction of the top rotor's wake to precisely evaluate the stream tube deformation and the associated velocities [38].

Several assumptions were made to facilitate the study of the coaxial model in this research[38],[32]:

1. The formalization of BEMT equations for coaxial rotors assumes that the slipstream wake from the upper rotor influences the flow into the lower rotor, but not vice versa. Whereas in general, the lower rotor does influence the upper rotor where an additional velocity is induced over the entire upper rotor. This is not taken into account in the equations since both rotors are studied as if they were in isolation, and this will help to remove the need for an iterative process throughout the entire system when combining both rotor's effects.
2. The lower rotor operates within a uniform downwash coming from the upper rotor which will simplify hugely the study.
3. The flow velocities of the two rotors are calculated independently, and interference effects are combined through superposition, a reasonable assumption except for very closely spaced rotors. However, this does not imply that the lower rotor has no impact on the upper rotor's performance. Since the inflow and spanwise loading distributions of both rotors are influenced by the overall trim state of the coaxial system (i.e., thrust sharing or torque balance), reciprocal effects between the rotors are inevitable. In scenarios where the rotors are closely spaced, both rotors would share the same inflow and experience similar performance levels. Finally and as mentioned previously, the impact of the lower rotor on the upstream velocity of the upper rotor will not be taken into account to simplify the study.
4. The analysis is limited to the hover flight scenario for the coaxial system. This also signifies that the aerodynamic forces and moments experienced by the elements are independent of the azimuthal position of the blade.
5. Any section of the lower rotor that falls within the hub region experiences only external velocity because the blades don't extend to the center of the rotation but to the edge of the hub, which has an influence on the wake geometry (See Figure 2.5).

It is important to note that actual blades can experience deformations, flapping, or lead-lag motions relative to their rotational axis. However, this research focuses exclusively on rigid blades, where the motion is dictated solely by rotational speed, simplifying the equations involved.

Finally, this chapter will present the BEMT equations utilized to compute helicopter rotor performance in the context of single rotor models operating in hover. Then, the equations will be extended to coaxial systems using the additional assumptions mentioned above.

2.1.1 Blade Element Theory (BET)

The blade element theory (BET) is a foundational method for analyzing helicopter rotor aerodynamics. This theory provides detailed methodologies for predicting rotor performance by discretizing the rotor blade into small sections and considering the aerodynamic forces acting on each section [36].

BET was first suggested by Stefan Drzewiecki in the late 19th and early 20th centuries for the analysis of airplane propellers. Notably, Frederick W. Lanchester also made significant contributions to solving the problem during this period. In the early 20th century, considerable scientific debate occurred about the proper theoretical aerodynamic analysis of propellers and helicopter rotors, primarily between Drzewiecki and Louis Bréguet. These discussions laid the groundwork for modern rotor analysis techniques [36].

The principles of BET assume no mutual influence of adjacent blade elements; these sections are idealized as 2-D airfoils. However, the effects of a non-uniform “induced inflow” across the blade, sourced from the rotor wake, are accounted for through modifications to the angle of attack at each blade element. Additionally, BET involves discretizing the rotor blade into infinitesimal sections, known as blade elements. Each blade element is treated as a quasi-2D airfoil, generating aerodynamic forces and moments independently of other sections (See Figure 2.1). The aerodynamic loads on each blade element are determined by considering local velocities and angles of attack. These loads are then integrated to determine the overall rotor thrust and power [13], [26].

Figure 2.1 shows a sketch of the flow environment and aerodynamic forces at a blade element section. The aerodynamic forces are assumed to arise solely from the velocity and angle of attack normal to the leading edge of the blade section.

The resultant local flow velocity U at any blade element at a radial distance y from the rotational axis has an out-of-plane component U_A normal to the rotor as a result of climb V_∞ and induced v_i inflow and an in-plane component U_T which is the difference between the rotation speed Ωy and the swirl induced velocity u_i , parallel to the rotor because of blade rotation, relative to the disk plane. Moreover, the resultant local flow velocity has a radial component U_R that acts along the blade, typically neglected in axial flows in accordance with the sweep independence principle [36].

$$U_A = V_\infty + v_i \quad (2.1)$$

$$U_T = \Omega y - u_i \quad (2.2)$$

$$U_R = 0 \quad (2.3)$$

The resultant velocity is therefore:

$$U = \sqrt{U_A^2 + U_T^2} \quad (2.4)$$

The effective angle of attack, α , is derived by subtracting the inflow angle, ϕ and the airfoil’s zero-lift angle α_0 from the pitch angle, θ :

$$\alpha = \theta - \phi - \alpha_0 \quad (2.5)$$

The inflow angle (or induced angle of attack) ϕ is derived as follows:

$$\phi = \tan^{-1} \left(\frac{U_T}{U_A} \right) \quad (2.6)$$

The aerodynamic coefficients definitions are then used to determine the resultant incremental lift dL , incremental drag dD , and pitching moment dM per unit span:

$$dL = \frac{1}{2} \rho U^2 c_l c dy \quad (2.7)$$

$$dD = \frac{1}{2} \rho U^2 c_d c dy \quad (2.8)$$

$$dM = \frac{1}{2} \rho U^2 c_m c y dy \quad (2.9)$$

where ρ is the air density, c is the chord length, and c_l , c_d , and c_m are the lift, drag, and moment coefficients, respectively. The lift dL and drag dD are perpendicular and parallel to the resultant flow velocity respectively, and thus the forces acting on the blade, as can be seen in Figure 2.1, can be resolved as follows:

$$dF_z = dL \cos \phi - dD \sin \phi \quad \text{and} \quad dF_x = dL \sin \phi + dD \cos \phi \quad (2.10)$$

Therefore, the contributions to the thrust, torque, and power of the rotor are:

$$dT = N dF_z \quad (2.11)$$

$$dQ = N dF_x y \quad (2.12)$$

$$dP = \Omega dQ = N dF_x \Omega y \quad (2.13)$$

where N is the number of blades of the rotor.

Substituting the results for dF_x and dF_z gives:

$$dT = N(dL \cos \phi - dD \sin \phi) \quad (2.14)$$

$$dQ = N(dL \sin \phi + dD \cos \phi) y \quad (2.15)$$

$$dP = \Omega dQ = N(dL \sin \phi + dD \cos \phi) \Omega y \quad (2.16)$$

Finally, the forces and moments acting on the entire blade are determined through the integration of the elementary loads over the blade radius:

$$T = \frac{N}{2\pi} \int_{R_0}^R (dL \cos \phi - dD \sin \phi) dy \quad (2.17)$$

$$Q = \frac{N}{2\pi} \int_{R_0}^R (dL \sin \phi + dD \cos \phi) y dy \quad (2.18)$$

And the total propulsive power is then given by:

$$P = \Omega Q \quad (2.19)$$

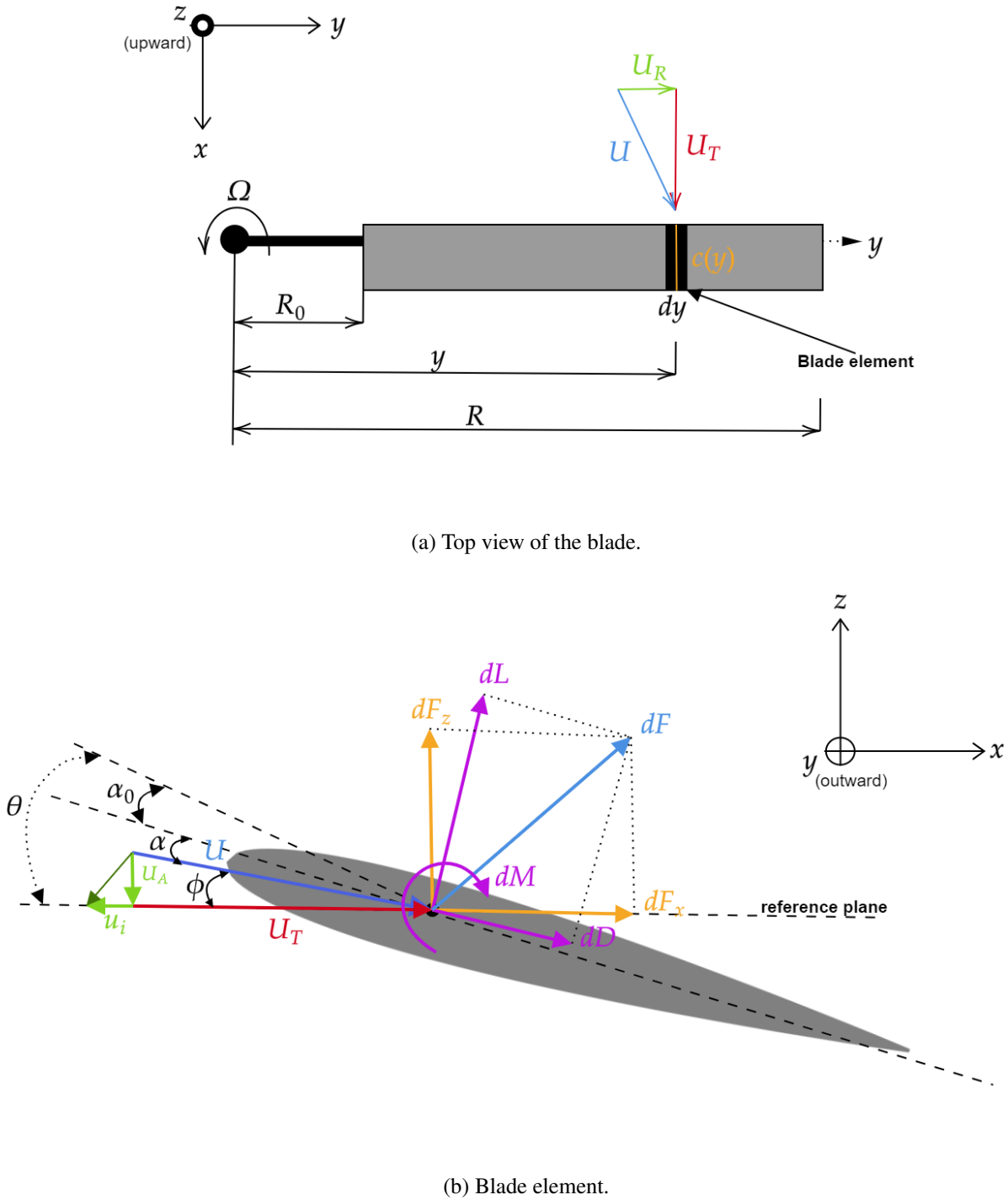


Figure 2.1: Forces, angles, and velocities acting on a blade section. Adapted from [36]

BEMT extends BET by linking it with momentum theory, providing a more comprehensive determination of induced velocities and angle of attack distributions that are needed to be able to compute the aerodynamic loads for each element presented above. This hybrid approach incorporates the effects of the rotor wake and interactions between blade elements and the airframe (See section 2.1.2).

2.1.2 Momentum Theory (MT)

The momentum theory, also known as the actuator disk theory, is a fundamental principle in aerodynamics used to describe the performance of propellers and rotors. Initially formulated by William Froude in the late 19th century and later refined by his brother Robert Edmund Froude and other engineers, the theory outlines that an idealized, infinitely thin disk can be used to model the thrust produced by a propeller or rotor [26], [39].

The initial formulation of the momentum theory assumes an inviscid and incompressible flow, with the flow velocity increasing across the disk and a corresponding decrease in pressure, leading to the generation of thrust. The theory simplifies the complex flow dynamics around the propeller into a one-dimensional flow model, allowing for the calculation of thrust and power requirements based on the conservation of mass, momentum, and energy. Thus, this theory applies the conservation laws of fluid mechanics to evaluate the performance of an idealized rotor. Moreover, the geometry of the rotor blades is completely ignored here, and the focus relies only on the stream tube that traverses the rotor disk as it is represented in Figure 2.2.

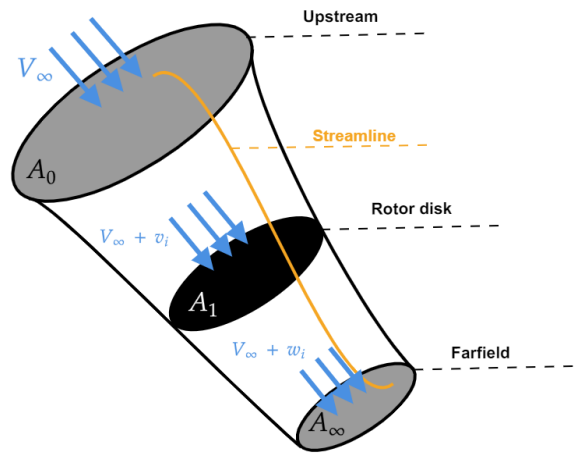


Figure 2.2: Streamtube of the flow over a rotor disk.

MT was later expanded by Betz and then Glauert to include the effects of rotation in the slipstream, leading to the general momentum theory. This expanded formulation considers the rotational motion imparted to the airflow by the rotor blades, which creates a swirling slipstream behind the propeller. The inclusion of rotational effects provides a more accurate description of the flow field and improves the predictions of the rotor blades' performance [13], [23].

In momentum theory, the rotor is conceptualized as an actuator disk, hence the name actuator disk theory. The actuator disk theory simplifies the analysis of rotor blades' behavior by abstracting away the complexities of their physical shape. Instead, it focuses on the global flow passing through the rotor. This theory allows for basic design choices concerning the propeller loading and dimensions, starting from the required thrust and desired propulsive efficiency.

The key assumptions [13], [23],[26],[32], made in the actuator disk theory are:

- Constant flow velocity and pressure over each section normal to the throughflow in the rotor stream tube.
- An infinite rotational speed of the propeller, resulting in zero torque and no change in the tangential velocity.

- The conservation of mass equations applied to the stream tube between the sections leads to a constant axial velocity across the rotor and a jump in the static pressure at the level of the rotor propellers.

Consequently, this approach reflects the ideal power output of a rotor, failing to represent the losses in the wake, which impact the coaxial configurations since it doesn't account for the tangential velocity component affecting the lower rotor. Therefore, the following equations will represent an approximate solution of the general momentum theory for a single rotor case.

The general momentum theory([32], [39]) addresses the detailed solutions of the four fundamental conservation laws in fluid dynamics. These laws are the conservation of mass, linear momentum, angular momentum, and energy within a defined control volume that surrounds the rotor and its wake and has a surface area A , as shown in Figure 2.3. Assuming steady, incompressible flow with no viscous losses in a frame moving with the rotor, a general equation governing the conservation of mass applied to the control volume can be written as:

$$\oint_{CV} \rho \mathbf{U} \cdot \mathbf{n} dA = 0 \quad (2.20)$$

where $\mathbf{U} = (U_A, U_T, U_R)$ is the local velocity in the axial, azimuthal, and radial directions, dA is the differential area at a radius y that extends until the surface of the control volume, \mathbf{n} is the unit normal vector to the surface of the control volume, and ρ is the density of the fluid.

Because the force on the fluid is supplied by the rotor, by Newton's third law, the fluid must exert an equal and opposite force on the rotor. This force is the rotor thrust T and is computed using the conservation of linear momentum:

$$\mathbf{T} = \oint_{CV} \rho \mathbf{U} \mathbf{U} \cdot \mathbf{n} dA + \oint_{CV} p \mathbf{n} dA \quad (2.21)$$

Moreover, the power consumed (work) by the rotor can be expressed using the equation governing the conservation of energy in the flow:

$$\mathbf{P} = \oint_{CV} \left(p + \frac{1}{2} \rho v^2 \right) \mathbf{v} \cdot \mathbf{n} dA \quad (2.22)$$

where P denotes the power consumed by the rotor.

Eq.2.22 states simply that the work done on the fluid by the rotor acts like a gain in kinetic energy of the fluid in the rotor slipstream per unit time.

Finally, the torque equation can also be derived from Eq.2.21 by multiplying the thrust force by the radius y :

$$\mathbf{Q} = \oint_{CV} \rho \mathbf{y} \times \mathbf{U} \mathbf{U} \cdot \mathbf{n} dA + \oint_{CV} p \mathbf{y} \times \mathbf{n} dA \quad (2.23)$$

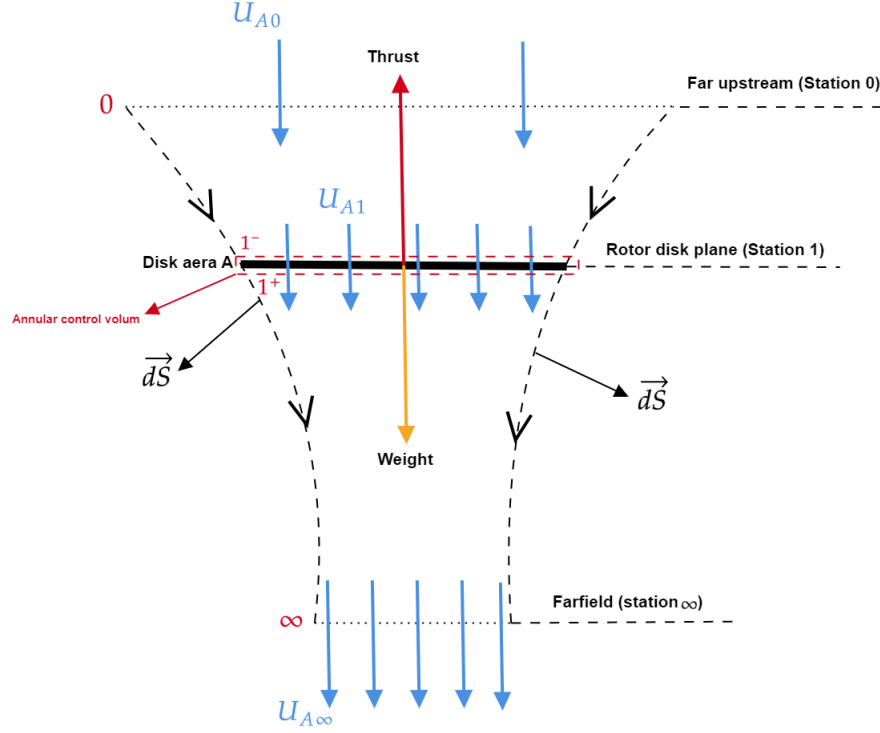


Figure 2.3: Flow model of a rotor in hovering flight. Adapted from [37]

As shown in Figure 2.3, the rotor disk has an area A and a total thrust T . Station 0 denotes the plane far upstream of the rotor, wherein the hovering case the fluid is quiescent (i.e., $V_0 = 0$). Stations 1^- and 1^+ are the planes just above and below the rotor disk, respectively, and the "far" wake is denoted by station ∞ . At station 1^- , the flow is accelerated due to the rotor exercising work and thus contracts to match the disk diameter. At station 1^+ , contraction further continues downstream until it reaches equilibrium in the far field (station ∞). At the plane of the rotor, between stations 1^- and 1^+ , assume the velocity v_i , the axial induced velocity which is the velocity imparted to the mass of air contained in the control volume at the rotor disk. At station ∞ and thus in the far wake, the velocity will be increased over that at the plane of the rotor and this velocity is denoted by w_i .

Momentum theory relies on the conservation principles of momentum and mass flow across these three main sections of the streamtube: far upstream of the rotor (Station 0), at the rotor (Station 1), and far downstream of the disk (Station ∞). Upstream of the rotor, the axial velocity $U_{A,0} = V_\infty$, corresponds to the perpendicular component of the freestream.

As the flow moves downstream and encounters the rotor, it accelerates to $U_{A,1} = V_\infty + v_i$. Further downstream, the velocity increases to $U_{A,\infty} = V_\infty + w_i$. Across all sections normal to the streamtube, both flow velocity and pressure are assumed constant. The rotor primarily induces a jump in static pressure within the tube.

The induced velocity, v_i , at the rotor disk is a critical component in BEMT. It modifies the inflow angle and thus the angle of attack of each blade element. The induced velocity at the rotor disk can be estimated using momentum theory. The basic principle involves applying the conservation equations (Eq.2.20, Eq.2.21 and Eq.2.22) to the annular control volume around the rotor disk.

From the assumption that the flow is quasi-steady and by the principle of conservation of mass (Eq.2.20), the mass flow rate, \dot{m} , must be constant within the boundaries of the rotor wake (control volume). Therefore, the mass flow rate is:

$$\dot{m} = \iint_{CV} \rho \mathbf{U} \cdot d\mathbf{A} = \iint_{+1} \rho \mathbf{U} \cdot d\mathbf{A} \quad (2.24)$$

and the 1-D incompressible flow assumption reduces this equation to:

$$\dot{m} = \rho A_\infty w_i = \rho A_1 v_i = \rho A v_i \quad (2.25)$$

where A is the area of the rotor disk.

The thrust produced by the rotor is related to the rate of change of momentum of the air passing through the rotor disk (Eq.2.21):

$$T = \iint_\infty \rho (\mathbf{U} \cdot d\mathbf{A}) \mathbf{U} - \iint_0 \rho (\mathbf{U} \cdot d\mathbf{A}) \mathbf{U} \quad (2.26)$$

Because in hovering flight the velocity well upstream of the rotor is quiescent, the second term on the right-hand side of Eq.2.26 is zero. Therefore, for the hover problem, the rotor thrust can be written as the scalar equation:

$$T = \iint_\infty \rho (\mathbf{U} \cdot d\mathbf{A}) \mathbf{U} = \dot{m} w_i \quad (2.27)$$

From the principle of conservation of energy (Eq.2.22), the work done on the rotor is equal to the gain in energy of the fluid per unit of time. The work done per unit time, or the power consumed by the rotor, is $T v_i$, and this results in the equation:

$$T v_i = \iint_\infty \frac{1}{2} \rho (\mathbf{U} \cdot d\mathbf{A}) \mathbf{U}^2 - \iint_0 \frac{1}{2} \rho (\mathbf{U} \cdot d\mathbf{A}) \mathbf{U}^2 \quad (2.28)$$

In hover ($V_0 = 0$), the second term on the right-hand side of the above equation is zero so that:

$$T v_i = \iint_\infty \frac{1}{2} \rho (\mathbf{U} \cdot d\mathbf{A}) \mathbf{U}^2 = \frac{1}{2} \dot{m} w_i^2 \quad (2.29)$$

From Eqs.2.27 and 2.29, it is clear that:

$$v_i = \frac{1}{2} w_i \quad (2.30)$$

or that $w_i = 2v_i$. This, therefore, gives a simple relationship between the induced velocity in the plane of the rotor and the induced velocity far downstream.

Additionally, The relationship between the induced velocity at the rotor disk and the induced velocity far in the wake can also be derived from the pressure variation through the rotor flow field in the hover state. Bernoulli's equation can be applied along a streamline above and below the rotor disk (Station 1^- and 1^+). Since there is an energy addition by the rotor, a pressure jump occurs across the disk. Although Bernoulli's

equation cannot be directly applied between points in the flow across the disk due to this pressure jump, the uniformity of the pressure jump over the rotor disk allows its application to all streamlines within the control volume. In the case of incompressible flow, Bernoulli's equation serves as an alternative to the energy equation, rendering one of them redundant.

As discussed before (See Figure 2.3), far upstream of the rotor (Station 0), the diameter of the streamtube exceeds that of the rotor disk. The rotor accelerates the flow and contracts the streamtube to match the disk diameter. Downstream, the contraction continues until the static pressure inside the tube equilibrates with the far field pressure (Station ∞).

The rotor thrust is equal to the force applied on the disk due to the pressure difference:

$$T = A(p_{1+} - p_{1-}) \quad (2.31)$$

where $A = \pi R^2$ is the rotor disk area, and p_{1-} and p_{1+} denote the pressures before and after the rotor, respectively.

Simultaneously, the axial momentum balance across the streamtube says that:

$$T = \dot{m}(U_{A,\infty} - U_{A,0}) \quad (2.32)$$

where $\dot{m} = \rho A U_{A,1}$ is the air mass flow rate through the rotor. Equating Eq.2.31 with Eq.2.32 gives:

$$p_{1+} - p_{1-} = \rho U_{A,1}(U_{A,\infty} - U_{A,0}) \quad (2.33)$$

Moreover, in order to determine the static pressure change across the rotor disk, the Bernoulli equation is first applied between stations 0 and 1^- :

$$p_0 + \frac{1}{2}\rho U_{A,0}^2 = p_{1-} + \frac{1}{2}\rho U_{A,1}^2 \quad (2.34)$$

Then, the same thing is applied between stations 1^+ and ∞ :

$$p_{1+} + \frac{1}{2}\rho U_{A,1}^2 = p_\infty + \frac{1}{2}\rho U_{A,\infty}^2 \quad (2.35)$$

Given the equality of static pressures far up- and downstream of the rotor ($p_0 = p_\infty$), the system simplifies to:

$$p_{1+} - p_{1-} = \frac{1}{2}\rho(U_{A,\infty}^2 - U_{A,0}^2) \quad (2.36)$$

Combining this result with Eq.2.33, the velocity at the rotor disk becomes the arithmetic mean of the upstream and downstream velocities:

$$U_{A,1} = \frac{1}{2}(U_{A,\infty} + U_{A,0}) \quad (2.37)$$

Combining Eq.2.37 and what was mentioned before about the flow velocities that are assumed to be constant across all the sections normal to the stream tube, it results in:

$$V_\infty + v_i = \frac{1}{2}(V_\infty + w_i + V_\infty) \quad (2.38)$$

$$v_i = \frac{1}{2}w_i \quad (2.39)$$

The induced velocity in the farfield is twice the magnitude of the induced velocity at the rotor disk.

The advantage of deriving the relationship between the induced velocity far in the wake and at the rotor disk using the method of pressure variation is that it can also be used to derive the differential thrust and differential mass flow on each annular section that will be useful to determine the inflow angle by equating them to Eqs. 2.11, 2.12, 2.12.

Thus, by dividing the rotor streamtube into concentric annular sections, each with an area $dA = 2\pi y dy$. The differential mass flow rate through each annulus is:

$$\begin{aligned} d\dot{m} &= \rho U_{A,1} dA \\ &= 2\pi\rho(V_\infty + v_i)y dy \end{aligned} \quad (2.40)$$

The thrust produced by each annulus is proportional to the momentum change in the fluid passing through it:

$$dT = d\dot{m}(U_{A,\infty} - U_{A,0}) \quad (2.41)$$

and by using the results obtained from the pressure difference analysis:

$$\begin{aligned} U_{A,\infty} - U_{A,0} &= V_\infty + w_i - V_\infty \\ &= w_i \\ &= 2v_i \end{aligned} \quad (2.42)$$

Which finally gives:

$$\begin{aligned} dT &= 2\pi\rho(V_\infty + v_i)y dy 2v_i \\ &= 4\pi\rho(V_\infty + v_i)v_i y dy \end{aligned} \quad (2.43)$$

A similar derivation for the differential torque considering the tangential velocity gives:

$$\begin{aligned} dQ &= d\dot{m}(U_{T,\infty} - U_{T,0})y \\ &= 2\pi\rho(V_\infty + v_i)y dy (U_{T,\infty} - U_{T,0})y \\ &= 4\pi\rho(V_\infty + v_i)u_i y^2 dy \end{aligned} \quad (2.44)$$

Corrections for tip and root losses, such as the Prandtl-Glauert factor introduced by Prandtl [40],[49], are applied to account for the aerodynamic inefficiencies introduced by the finite blade length, such as the inefficiencies present near the blade tip due to tip vortices that affect the lift and drag. The Prandtl-Glauert tip loss factor, F , helps in adjusting the theoretical models to better match the real-world performance of rotors and is defined as:

$$F = \frac{2}{\pi} \arccos(\exp(-f_{\text{tip}}f_{\text{root}})) \quad (2.45)$$

where

$$f_{\text{tip}} = \frac{N(1-r)}{2r|\sin\phi|}$$

and

$$f_{\text{root}} = \frac{N(r - r_0)}{2r|\sin \phi|}$$

Note that r represents here the non-dimensional radius y/R .

Taking this loss factor into account in the momentum equations results in a decrease in lift generation due to diminished inflow angle. To accurately consider the effect of tip vortices on the components of the induced velocity, the tip loss factor is divided into two different loss factors, the thrust and power loss factors, K_T and K_P , [49] where:

$$K_T = 1 - (1 - F)|\cos \phi|$$

and

$$K_P = 1 - (1 - F)|\sin \phi|$$

Taking these two loss factors into account in the momentum equations of the mass flow and thrust gives:

$$dT = d\dot{m}(U_{A,\infty} - U_{A,0})K_T \quad (2.46)$$

$$= 4\pi\rho K_T (V_\infty + v_i)v_i y dy \quad (2.47)$$

$$dQ = d\dot{m}(U_{T,\infty} - U_{T,0})yK_P \quad (2.48)$$

$$= 4\pi\rho K_P (V_\infty + v_i)u_i y^2 dy \quad (2.49)$$

In the application of this research, the loss factor will not be considered for the sake of simplicity and because the primary performance metrics (e.g., thrust, torque, efficiency) are the main focus so the losses are discarded for the initial optimization. Also, neglecting the loss factors will reduce the computational complexity, allowing for faster simulations. However, its derivation method is presented because it is important to know what this parameter means since it is typically taken into consideration for most applications.

Furthermore, to simplify the comparison between the different blades further in this research, the performance metric will be the ratio $\frac{c_P}{c_T}$ that will be maximized in order to get the optimal configuration at which the rotor should operate. Thus, the conventional definitions of helicopter coefficients are used. Moreover, the U.S. convention will be adopted here, as most of the experimental cases in the validation section are based on data from the U.S. The key difference between the U.S. convention and the international standard is that the U.S. definition of the coefficient does not include the $\frac{1}{2}$ factor in the denominator, which is present in other conventions[37],[32]. The definitions of both conventions are represented in Table 2.1.

	International convention	US convention
Thrust Coefficient	$\frac{T}{\frac{1}{2}\rho A(\Omega R)^2}$	$\frac{T}{\rho A(\Omega R)^2}$
Power Coefficient	$\frac{P}{\frac{1}{2}\rho A(\Omega R)^3}$	$\frac{P}{\rho A(\Omega R)^3}$
Torque Coefficient	$\frac{Q}{\frac{1}{2}\rho A\Omega^2 R^3}$	$\frac{Q}{\rho A\Omega^2 R^3}$

Table 2.1: Thrust, moment, and power coefficients definitions for helicopter rotor applications expressed in the US and international conventions.

Finally, the advance ratio (μ) in this research will be equal to zero since we're considering only steady

conditions (Hover), but its definition for helicopters is the following:

$$\mu = \frac{V_{\infty}}{\Omega R} \quad (2.50)$$

2.2 Extension to Coaxial Rotor Model

Figure 2.4 illustrates the flow model used in the BEMT analysis of a coaxial rotor system, where the lower rotor operates within the slipstream of the upper rotor. The model includes five stations: station 0 (far upstream of the upper rotor), station 1 (at the upper rotor disk), station u, ∞ (in the wake of the upper rotor), station 2 (at the lower rotor disk), and station l, ∞ (far downstream of the lower rotor). $U_{u,0}$ and $U_{l,0}$ denote the upstream velocities for the upper and lower rotors, respectively. U_u and U_l indicate the velocities at the rotor disk level, while $U_{u,\infty}$ and $U_{l,\infty}$ represent the velocities far downstream of the rotors. U_l^* represents the induced velocity at the lower rotor disk in the outer region of the upper rotor wake, unaffected by the upper rotor's wake, and is not equal to U_l . The orange areas depict the infinitesimal circles representing the upper and lower rotors, as used in the BEMT analysis.

Concerning the coaxial rotor systems, the primary challenge that the BEMT encounters is the definition of the upstream velocity of the lower rotor $U_{l,0}$, since it is positioned directly in the wake of the upper rotor. To accurately determine the upstream velocity of the lower rotor, the contraction of the wake of the upper rotor needs to be evaluated as well as the deformation of the streamtubes and its associated velocities.

As clearly shown in Figures 2.4 and 2.5, the velocity profile for the second rotor can thus be decomposed as:

$$U_{l,0}(y) = \begin{cases} V_\infty & \text{if } 0 \leq y_l < y_{\text{hub}}, \\ U_{u,\infty} & \text{if } y_{\text{hub}} \leq y_l \leq y_{u,\infty}, \\ V_\infty & \text{if } y_{u,\infty} < y_l. \end{cases} \quad (2.51)$$

Where the indices $()_u$ and $()_l$ denote the upper and lower rotors, respectively, while $()_{u,\infty}$ signifies the wake of the upper rotor.

As explained previously, the upper rotor performance is computed as if it were isolated, so the simulation starts by solving it through regular BEMT. Once the velocity profile preceding the lower rotor is determined, it can be applied as the upstream velocity acting on the lower rotor. Afterward, BEMT is employed to solve the lower rotor as per standard practice, albeit utilizing the newly calculated values for the axial velocity upstream of each element, denoted as $U_{l,0}$.

2.2.1 Flow Model

As said before, it is important to understand the flow model to accurately determine the upstream velocity of the lower rotor, which is the velocity immediately preceding the lower rotor. Therefore, in this research, a multiple stream tubes (MST) model was considered in the blade configuration [32] as represented in Figure 2.5.

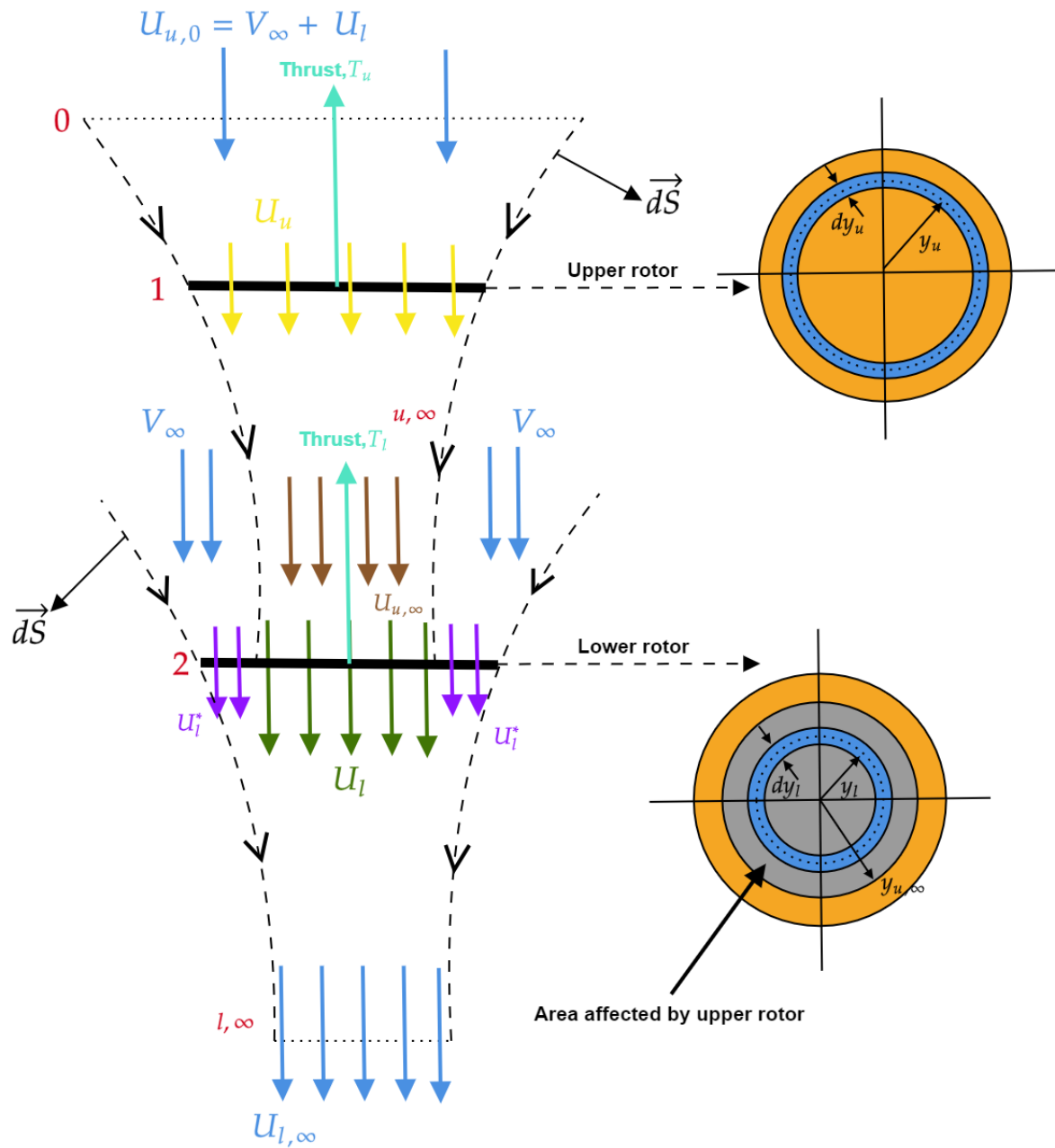


Figure 2.4: Flow model used for the BEMT analysis of a coaxial rotor system with the lower rotor operating in the slipstream of the upper rotor. Adapted from [38]

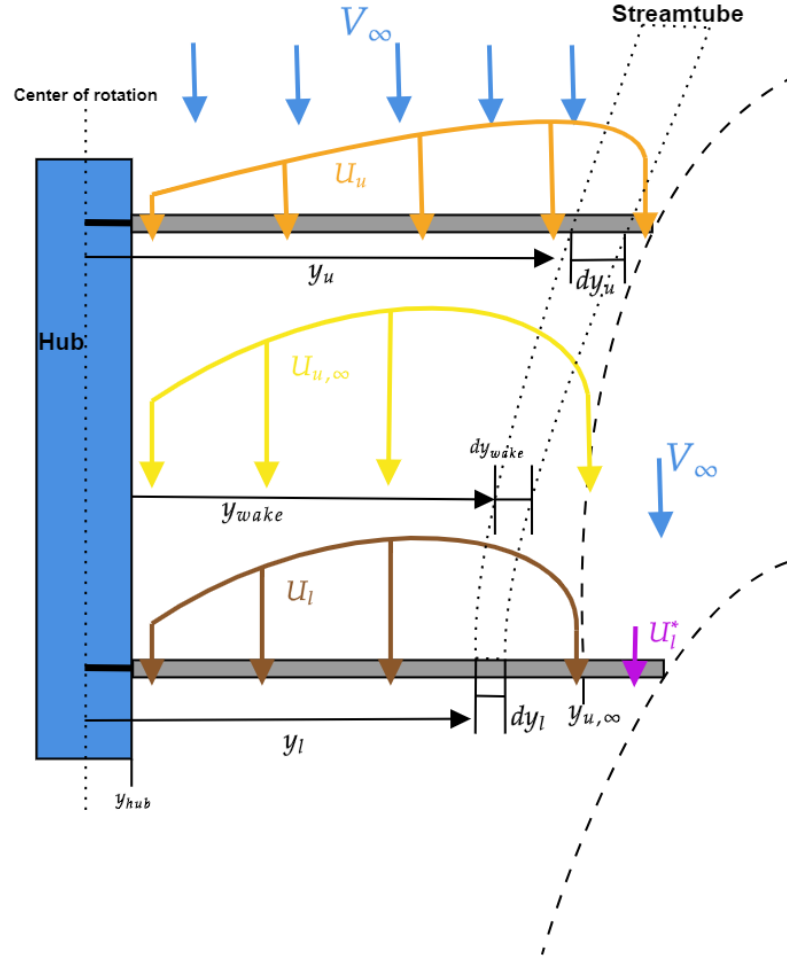


Figure 2.5: Velocities in the multiple stream tubes model for coaxial rotors. Adapted from [32].

This model, newly proposed by Thomas Lambert, a PhD candidate from the University of Liège, is unique and not found in the existing literature. It has demonstrated computational efficiency through its accurate results in ROTARE, especially when compared to results from other experiments.

In the multiple stream tube (MST) model, each streamtube contracts in relation to the thrust it generates, resulting in a non-uniform velocity within the wake of the upper rotor. This model requires consideration of several factors (see Figure 2.5):

- The radii y_{wake} represent the distance from an arbitrary section in the wake below the upper rotor, and it is no longer constant.
- The width of the radii dy_{wake} is no longer uniform since it depends on the thrust it produces.
- The swirl velocity is considered here to provide a better understanding of the slipstream behavior, which results in a non-zero parallel velocity $V_{||} \neq 0$.

Applying the principle of mass flow conservation between the disk and the wake below the upper rotor for a single annulus gives:

$$d\dot{m}_{u,\infty} = d\dot{m}_{u,1} \quad (2.52)$$

where $()_{u,1}$ signifies the station at the upper rotor disk and $()_{u,\infty}$ signifies the station in the wake below the upper rotor.

$$dA_{u,\infty}U_{u,\infty} = dA_{u,1}U_{u,1} \quad (2.53)$$

Using the definition of the rotor disk area $dA = 2\pi y dy$ used previously, the equation becomes:

$$\begin{aligned} 2\pi y_{u,\infty} dy_{u,\infty} U_{u,\infty} &= 2\pi y_{u,1} dy_{u,1} U_{u,1} \\ y_{u,\infty} dy_{u,\infty} &= y_{u,1} dy_{u,1} \frac{U_{u,1}}{U_{u,\infty}} \\ y_{u,\infty} dy_{u,\infty} &= y_{u,1} dy_{u,1} \kappa \end{aligned} \quad (2.54)$$

Where $\kappa(y) = \frac{U_{u,1}}{U_{u,\infty}}$ represents the contraction ratio specific to each annulus. As stated previously, when the lower rotor is positioned in the far wake of the upper rotor, this contraction ratio can be directly determined through the application of momentum theory.

It is evident from Eq. 2.54 that the contraction influences both the mean radius of the annulus ($y_{u,\infty}$) and its width ($dy_{u,\infty}$).

To simplify the equation and streamline the solution process, PhD candidate Thomas Lambert proposed a simplified multiple stream tube (SMST) model [32]. In this model, only the mean radii of the tubes undergo contraction, while their width remains constant. This approach also allows for the direct determination of each stream tube's center position once the contraction ratio is known.

In the general MST model, tube radius and width calculations are carried out iteratively, beginning with the innermost tube and moving outward, as illustrated in Figure 2.6. The impermeability of the tubes ensures that each tube fits perfectly against the preceding one. Similarly, the rotor hub is assumed to be impermeable, necessitating a straight alignment of the inner wall of the first tube against it. This boundary condition directly links the mean radius and width of the tubes.

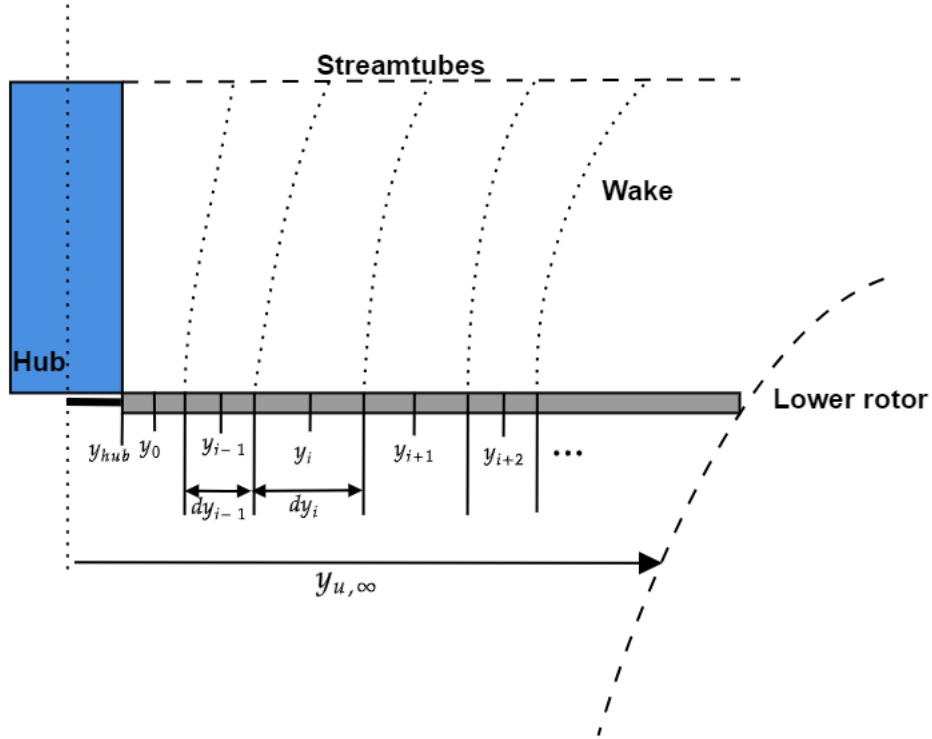


Figure 2.6: Representation of the detailed radii and width used in the calculation of the tube radius. Adapted from [32]

For any given annulus indexed as i , the following relation can be established:

$$y_i - \frac{dy_i}{2} = y_{i-1} + \frac{dy_{i-1}}{2} \quad (2.55)$$

$$y_i = y_{i-1} + \frac{dy_{i-1}}{2} + \frac{dy_i}{2}$$

where,

$$y_{hub} = y_0 - \frac{dy_0}{2} \quad (2.56)$$

Knowing Eq.2.54, and applying Eq.2.55 on $y_{u,\infty,i}$ for the tube i :

$$y_{u,1,i} dy_{u,1,i} \kappa = y_{u,\infty,i} dy_{u,\infty,i}$$

$$y_{u,1,i} dy_{u,1,i} \kappa = \left(y_{u,\infty,i-1} + \frac{dy_{u,\infty,i-1}}{2} + \frac{dy_{u,\infty,i}}{2} \right) dy_{u,\infty,i} \quad (2.57)$$

$$2y_{u,1,i} dy_{u,1,i} \kappa = dy_{u,\infty,i}^2 + 2dy_{u,\infty,i} \left(y_{u,\infty,i-1} + \frac{dy_{u,\infty,i-1}}{2} \right)$$

Rearranging the equation gives:

$$\begin{aligned} dy_{u,\infty,i}^2 + 2dy_{u,\infty,i}\left(y_{u,\infty,i-1} + \frac{dy_{u,\infty,i-1}}{2}\right) - 2y_{u,1,i}dy_{u,1,i}\kappa &= 0 \\ dy_{u,\infty,i}^2 + 2\left(y_{u,\infty,i-1} + \frac{dy_{u,\infty,i-1}}{2}\right)dy_{u,\infty,i} - 2y_{u,1,i}dy_{u,1,i}\kappa &= 0 \end{aligned} \quad (2.58)$$

Solving Eq.2.58 for $dy_{u,\infty,i}$:

$$\rho = 4\left(y_{u,\infty,i-1} + \frac{dy_{u,\infty,i-1}}{2}\right)^2 + 8y_{u,1,i}dy_{u,1,i}\kappa \quad (2.59)$$

The roots of Eq.2.58 are:

$$\begin{aligned} dy_{u,\infty,i} &= \frac{-2\left(y_{u,\infty,i-1} + \frac{dy_{u,\infty,i-1}}{2}\right) + \sqrt{4\left(y_{u,\infty,i-1} + \frac{dy_{u,\infty,i-1}}{2}\right)^2 + 8y_{u,1,i}dy_{u,1,i}\kappa}}{2} \\ &= -\left(y_{u,\infty,i-1} + \frac{dy_{u,\infty,i-1}}{2}\right) + \sqrt{\left(y_{u,\infty,i-1} + \frac{dy_{u,\infty,i-1}}{2}\right)^2 + 2y_{u,1,i}dy_{u,1,i}\kappa} \end{aligned} \quad (2.60)$$

Thus, Eq.2.60 is the solution for the width of the tube i , which only depends on the contraction ratio, the known parameters of the tube at the disk, and the contraction of the preceding tube $i - 1$.

Starting with the innermost radius, the process is repeated iteratively for each successive annulus, moving outward until the outermost one is reached. These calculated velocities, using the contraction ratio κ , are then matched to their corresponding radial positions. Once assigned, the velocities are mapped to the lower rotor's discretization and serve as the external velocity impacting the affected elements. Meanwhile, all other elements are subjected only to the freestream velocity V_∞ .

Finally, in the code used for the simulations in this research, the contraction ratio is assumed to be of the value $\frac{1}{2}$ based on ideal flow consideration where only half of the area of the lower rotor operates in an effective climb velocity induced by the upper rotor [38].

2.3 Numerical Implementation

All models presented previously were implemented in an open-source Matlab code called ROTARE, which focuses on modeling single and coaxial rotors in hover and axial flow.

The integrals defined earlier in the blade element theory (section 2.1.1) were evaluated in ROTARE using the straightforward trapezoidal rule, which has the ability to give accurate results while keeping the computation efficient at the same time.

Concerning the analysis of coaxial rotors, it is currently supported for either hovering rotors or axial flows only. In those cases, the first rotor is evaluated exactly as if it were in isolation. The axial and swirl velocity induced by the first rotor is then passed to the second rotor as inlet velocity. The contraction of the wake is then calculated based on the distance between the two rotors, and the velocity profile is adapted accordingly. The second rotor is then evaluated as if it were in isolation as well but with the new inlet velocity profile.

2.3.1 ROTARE Software

ROTARE is an advanced, open-source Matlab code implementation of the Blade Element Momentum Theory (BEMT). It is specifically designed for the analysis and design of a wide range of rotors, including those found in diverse applications such as helicopters, aircraft propellers, wind turbines, and tidal turbines.

ROTARE was primarily developed for academic purposes at the University of Liège, Belgium, by Thomas Lambert during his Ph.D. The code was subsequently extended to include a variety of solvers and numerous enhancements to the underlying methodology, as well as the capacity to accommodate more complex geometries. The software has since evolved into a comprehensive tool for analysis in a diverse array of fields.

Moreover, ROTARE is capable of modeling blade geometries with varying twist, chord, and airfoil for both single and coaxial rotors according to specific design requirements. Currently, the software can simulate both single isolated and coaxial rotors. Such cases may be studied in steady conditions (e.g., a hovering helicopter) or in axial flows (e.g., the propeller of an aircraft or the rotary wing of a helicopter in climb). However, it is still undergoing significant development, necessitating the validation of the model for the case of a coaxial rotor and a single rotor. This process is essential to ensure the software's viability [33].

Furthermore, ROTARE is capable of accommodating real-world considerations such as corrections for tip and hub losses, as well as other corrections and extensions, including those considering the effects of spinners and the influence of compressibility, which makes the analysis more accurate [33].

Finally, ROTARE addresses the resolution of the non-linear blade element equations by implementing four different solvers, all based on the same set of initial equations. These solvers differ in their approach to the equations, with the additional assumptions or modifications to the nonlinear system of equations (mostly the momentum equations) serving to simplify the formulation or facilitate the convergence of the solution. A comparison of these solvers is represented in Table 2.2.

	Leishman	IndFact	IndVel	Stahlhut
Assumptions	Small angles $V \ll U$ Drag \ll Lift	-	-	-
Applications	Hover/ideal and slow axial flow	Any	Any	Any
Convergence	Guaranteed	Medium	Medium	Easy
CPU time	Fastest	High	High	Medium

Table 2.2: Comparison between ROTARE's solvers [32].

2.3.2 Solver

The integration of the four different solvers mentioned in section 2.3.1 in ROTARE provides a deeper understanding of the theory and its applications. However, the results of this research are obtained using only one of the four solvers, the *IndVel* solver. It consists of a pure resolution of the initial system, without any major rewrite or additional assumptions. It has the benefit of being directly usable in any flow condition. This solver focuses on the iterative resolution for the induced velocities directly instead of solving for the induction factors following these steps:

1. Calculate velocities and angles: The axial and tangential velocity components at the propeller disk are calculated as:

$$U_A = \frac{V_\infty + v_i}{2} \quad (2.61)$$

$$U_T = \Omega y - \frac{u_i}{2} \quad (2.62)$$

Here, U_A and U_T represent the average axial and tangential velocities at the propeller disk, respectively, whereas v_i and u_i represent the axial and tangential velocities in the slipstream, respectively.

2. Compute local mass flow rate: The local mass flow rate is determined using the expression:

$$\dot{m} = 2\pi\rho y dy \cdot U_A \quad (2.63)$$

This accounts for the mass flow through the rotor disk at a given radius y . Here, ρ represents the air density.

3. Calculate the new estimates for the relative velocity and Reynolds number: The magnitude of the relative velocity at the blade elements is computed as:

$$U = \sqrt{U_A^2 + U_T^2} \quad (2.64)$$

The Reynolds number is computed based on the flow velocity, the characteristic length, and the flow viscosity:

$$Re = \frac{U \cdot c}{\nu} \quad (2.65)$$

4. Determine inflow angle and angle of attack: The inflow angle ϕ and the angle of attack α are given by:

$$\phi = \tan^{-1} \left(\frac{U_A}{U_T} \right) \quad (2.66)$$

$$\alpha = \theta - \phi \quad (2.67)$$

where θ is the true blade pitch angle.

5. Compute lift and drag coefficients: The lift (c_l) and drag (c_d) coefficients are obtained using the airfoil polars as functions of the angle of attack and the Reynolds number, which depends on the relative velocity and blade characteristics:

$$c_l(Re, \alpha) \quad \text{and} \quad c_d(Re, \alpha) \quad (2.68)$$

6. Calculate aerodynamic forces: The lift and drag forces per unit span are calculated using:

$$dL = c_l \cdot \frac{1}{2} \rho U^2 c dy \quad (2.69)$$

$$dD = c_d \cdot \frac{1}{2} \rho U^2 c dy \quad (2.70)$$

7. Determine axial and tangential forces: These forces are projected into axial and tangential components:

$$dF_a = N (dL \cos(\phi) - dD \sin(\phi)) \quad (2.71)$$

$$dF_u = N (dL \sin(\phi) + dD \cos(\phi)) \quad (2.72)$$

These forces represent the thrust and torque contributions.

8. Update induced velocities: The induced velocities are updated using the calculated forces and the mass flow rate:

$$v_i = V_\infty + \frac{dF_a}{\dot{m} K_T} \quad (2.73)$$

$$u_i = \frac{dF_u}{\dot{m} K_P} \quad (2.74)$$

Here, K_T and K_P are correction factors accounting for the losses due to the inflow angle and are computed as follows:

$$K_T = 1 - (1 - F) \cos(\phi) \quad (2.75)$$

$$K_P = 1 - (1 - F) \sin(\phi) \quad (2.76)$$

where F is Prandtl's loss factor. In this research, tip and hub losses are not considered in the simulations. Therefore, Prandtl's loss factor is set to zero, $F = 0$. However, the empirical method used to compute Prandtl's loss factor is represented in section 2.1.2.

9. Apply relaxation for convergence: To facilitate convergence, a relaxation factor is applied to the updated velocities:

$$v_i = v_{i,\text{old}} \cdot (1 - \text{relax}) + v_i \cdot \text{relax} \quad (2.77)$$

$$u_i = u_{i,\text{old}} \cdot (1 - \text{relax}) + u_i \cdot \text{relax} \quad (2.78)$$

where $\text{relax} = 0.1$. This relaxation factor was selected because a system with a stronger tendency to diverge requires a smaller relaxation coefficient to maintain stability, though this also increases convergence time. Different configurations and operating conditions might necessitate varying relaxation values. Typically, a relaxation factor of 0.5 is used for efficient convergence. However, in scenarios with low axial velocities, as in this study, it is necessary to reduce the relaxation factor to 0.1 to ensure convergence[32].

10. Check for convergence: The solver checks if the changes in induced velocities are within a specified

tolerance:

$$\left| \frac{v_i - v_{i,\text{old}}}{v_{i,\text{old}}} \right| < \varepsilon \quad (2.79)$$

$$\left| \frac{u_i - u_{i,\text{old}}}{u_{i,\text{old}}} \right| < \varepsilon \quad (2.80)$$

where $\varepsilon = 10^{-3}$.

Initially, the axial induced velocity is assumed to be 0.01 m/s and the tangential component is 0. The process iterates through these steps until the solution converges or the maximum number of iterations is reached. Once convergence is achieved, the updated performance metrics are stored in the operating rotor object's properties. This includes the inflow angle ϕ , angle of attack α , and the induced axial and tangential velocities.

By solving for the induced velocities directly, this solver provides a robust approach to modeling the performance of rotors, particularly in complex scenarios like hovering.

Note also that the equations used in the solver are derived from the BEMT equations presented previously.

Finally, the model has recently been shown to be valid in stationary conditions and axial flows for both single and coaxial rotors. However, it should be noted that the model has not yet been validated for more complex cases, such as oblique flows. Consequently, the ROTARE software cannot be used in such cases.

Chapter 3

Validation of ROTARE

This chapter is dedicated to the validation of the Blade Element Momentum Theory (BEMT) code, ROTARE. The validation is conducted specifically for the case of a single rotor, as this represents a critical step prior to the validation of coaxial rotors.

In order to validate the BEMT code, two-bladed APC propellers (APC 9x6E and APC 14x12E) were simulated using ROTARE and the resulting data was compared against the available experimental measurements from the University of Illinois Urbana-Champaign (UIUC) [47] and another BEMT code from the literature[28].

Additionally, ROTARE will be compared against another dataset originating from experimental measurements conducted by David Biermann and Edwin P. Hartman, where the blades have a Clark Y airfoil.

For the simulation, geometrical characteristics were required such the chord and pitch distribution for the APC and the Clark Y propellers. These were also available at the UIUC data site [47]. However, the geometry information of the airfoil was computed using XFOIL software.

The comparison with experimental data is essential and important to give a clear answer about the reliability of ROTARE for propeller analysis. More details are presented in sections 3.1, 3.2.

3.1 Comparison with UIUC propeller measurements

The UIUC Propeller Data Site, developed and maintained by Professor Michael Selig and his students at the University of Illinois Urbana-Champaign (UIUC), serves as a comprehensive repository for aerodynamic performance data of small-scale propellers. The primary objective of this initiative is to fill the gap in research-quality data on low Reynolds number propellers, which are commonly used in radio-controlled aircraft and small unmanned aerial vehicles (UAVs). The database specifically includes measurements for propellers used on small UAVs and model aircraft.

Since its inception, the database has expanded significantly, including over 250 different propellers tested under various conditions. These tests are accurately documented across multiple volumes published from 2005 to 2022[47].

A comprehensive dataset was employed for the investigation, including a multitude of propellers from a variety of brands, including APC, Aero-Naut, Graupner, and others. A total of 250 propellers were subjected to evaluation in a multitude of testing conditions, with the majority of them falling within the diameter range of 9 to 11 inches. Wind tunnel testing was employed to measure the propeller performance under two conditions: a static condition, in which the advance ratio (J) was set to zero, and a data capture range across a series of

rotational speeds. Several RPM values were tested for each propeller, within a range of 1,500 to 7,500 RPM, depending on the diameter of the propeller. This allowed for an examination of Reynolds number effects.

The second condition was operational, whereby the propeller speed (RPM) was fixed, while the wind tunnel speed was varied to provide a range of advance ratios until the windmill state (zero thrust) was reached. Significant variation was observed in propeller efficiencies, with peak values ranging from approximately 0.65 (for an efficient propeller) to near 0.28 (for an exceptionally poor propeller). The findings illustrate that the choice of an optimal propeller for unmanned aerial vehicles (UAVs) can significantly influence the aircraft's performance[15].

The Reynolds number, a crucial parameter in these tests, was calculated based on the propeller blade chord and the rotational velocity at the 75% blade station. This parameter is essential for characterizing the aerodynamic performance in the low Reynolds number regime, which is typical for the small-scale propellers used in UAVs and model aircraft. These kinds of propellers typically operate in low Reynolds numbers between 50,000 to 100,000 [15].

The comparison will consist of analyzing the power and thrust coefficients from the simulations under both static and operational conditions, as well as the efficiency in operational conditions. Therefore, it is important to note that the relations used to compute the coefficients in ROTARE are the standard relations used for propellers and no more those used for helicopter as mentioned before, which align with the type of analysis conducted at UIUC. This ensures consistency in the methodology and allows for accurate comparison of results. Table 3.1 represents a comparison between the coefficient definitions for helicopter rotor and propeller applications expressed in US convention.

	Helicopters	Propellers
Thrust Coefficient	$\frac{T}{\rho A (\Omega R)^2}$	$\frac{T}{\rho n^2 D^4}$
Power Coefficient	$\frac{P}{\rho A (\Omega R)^3}$	$\frac{P}{\rho n^3 D^5}$
Torque Coefficient	$\frac{Q}{\rho A \Omega^2 R^3}$	$\frac{Q}{\rho n^2 D^5}$

Table 3.1: Thrust, power, and torque coefficients definitions for helicopter rotor and propeller applications expressed in US convention.

Additionally, the efficiency and the advance ratio were computed using the following relations, Efficiency (η):

$$\eta = \frac{J c_T}{c_P} \quad (3.1)$$

where J is the advance ratio.

Advance ratio (J):

$$J = \frac{V}{nD} \quad (3.2)$$

where V is the forward speed.

As previously stated, the UIUC data site contains a multitude of measurements obtained from a variety of propeller types. The propellers that will be used for the purposes of validation will be the APC (Advanced Precision Composites) propellers (See Figure 3.1), particularly the APC 9x6E and the APC 14x12E. APC propellers are widely known for their high efficiency and reliable performance, which makes them a popular choice for use in model aircraft and unmanned aerial vehicles (UAVs). The precise manufacturing standards and ex-

tensive testing procedures employed by the manufacturer ensure consistent aerodynamic characteristics, which is why the APC propellers are selected for this validation process.



Figure 3.1: Photo showing the APC propellers tested.

In terms of airfoil, the NACA 4412 airfoil will be employed. The NACA 4412 airfoil is frequently employed in these applications especially with the APC propellers, due to its advantageous lift-to-drag ratio and well-balanced stall characteristics. This airfoil provides efficient performance across a range of angles of attack, making it suitable for propellers used in varied flight conditions [11]. The choice of NACA 4412 for the APC propellers in ROTARE ensures an accurate representation of the aerodynamic performance typical of these propellers.

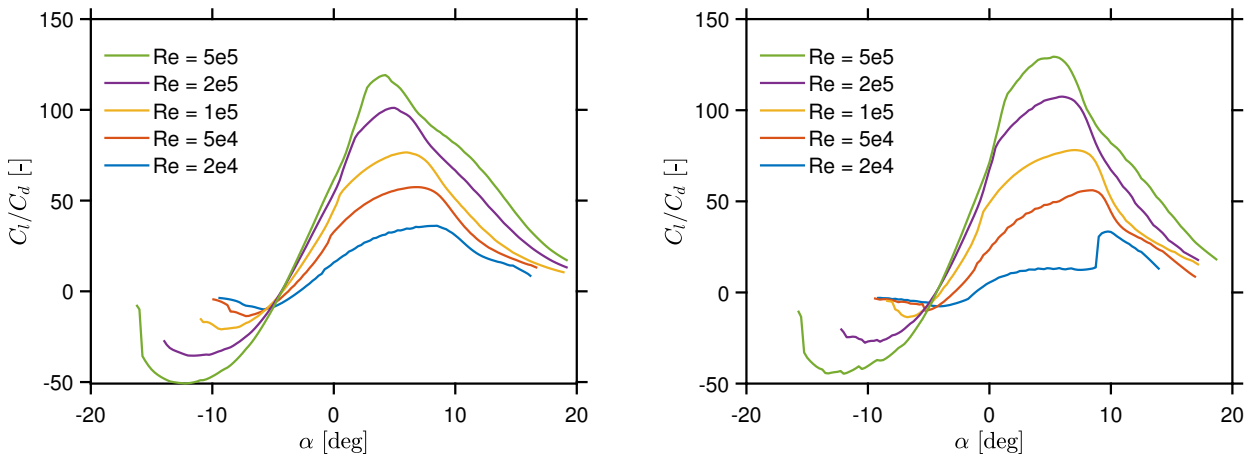
Given the decision to use the NACA 4412, it is crucial to provide a precise and accurate definition of the airfoil's geometry within the ROTARE code, in order to guarantee the accuracy of the performance calculations. To achieve this, two options are available, either the generation of detailed aerodynamic data using XFOIL, or the utilization of data already available on Airfoil Tools [1]. These approaches will provide the necessary geometric parameters to compute accurate results for the propeller's performance.

XFOIL is an interactive computer program designed for the analysis and design of subsonic isolated airfoils. The software is capable of predicting the performance of airfoils by solving the potential flow equations and integrating boundary layer equations, thereby providing the necessary lift, drag, and moment coefficients (polars) over a range of angles of attack [18]. It was thus decided that XFOIL should be used to compute the polars, which will provide the aerodynamic behaviour of the NACA 4412.

Nevertheless, XFOIL is unable to fully account for the full complexity of the flow at low Reynolds numbers, including viscous effects and laminar separations. This limitation can be explained by the assumptions that have been made in order to simplify the boundary layers and transition models in XFOIL. In particular, XFOIL makes the assumption of a steady, two-dimensional, incompressible flow and employs simplified models for the behavior of the boundary layer and the prediction of transitions. These assumptions include the presumption of a smooth transition from laminar to turbulent flow. However, at low Reynolds numbers, the transition is highly sensitive and can be influenced by factors such as slight surface roughness, disturbances, and other factors. [42].

According to various studies, such as those by Drela and Giles (1987) [17], these limitations are well-documented and suggest caution when using XFOIL for low Reynolds number applications. To improve the accuracy of the polars of the airfoil obtained from XFOIL at low Reynolds numbers, several modifications were done:

- **Enhanced Transition Modeling:** Incorporating more sophisticated transition models that account for the sensitivity of the laminar-to-turbulent transition at low Reynolds numbers. In XFOIL, the variable N_{crit} (critical amplification factor) plays a key role in modeling the transition from laminar to turbulent flow. It represents the environment's level of disturbance, with a typical value of 9 representing low turbulence (clean air). Lowering N_{crit} to 5 increases the sensitivity to transition, making XFOIL predict earlier laminar-to-turbulent transition, which is more representative of typical real-world conditions, especially at low Reynolds numbers. This can be seen on Figure 3.2 where at low Reynolds numbers, the aerodynamic performance are better captured when $N_{crit} = 5$ and even in general, the results are more accurate (curves are smoother) with $N_{crit} = 5$.
- **Surface Roughness Effects:** Including the effects of surface roughness in the boundary layer calculations, as real-world airfoils often encounter surface imperfections that can significantly affect transition and overall aerodynamic performance. This can be modeled in XFOIL by setting the variable $PANE$, which refers to the number of panels, to a higher number to define the panel geometry more precisely, leading to more accurate predictions.



(a) lift-to-drag ratio (C_l/C_d) versus angle of attack (α) with $N_{crit} = 5$.

(b) lift-to-drag ratio (C_l/C_d) versus angle of attack (α) with $N_{crit} = 9$.

Figure 3.2: Comparison of the quality of polars for NACA 4412 at various Reynolds numbers, using two different N_{crit} values.

Despite these modifications, XFOIL remains unable to accurately predict performance at Reynolds numbers below 50,000, particularly due to its challenges in modeling phenomena like laminar separation bubbles. Even with adjustments, such as lowering N_{crit} , these low-Reynolds results are unreliable. Therefore, it was decided to exclude data for Reynolds numbers below 50,000 from the analysis in order to get more accurate predictions, leading to a more effective validation of ROTARE against experimental data.

Furthermore, Figure 3.3 illustrates the comparative performance of the four solvers—*Indvel*, *Leishman*, *Indfact*, and *Stahlhut*—used in ROTARE. These solvers were used to compute the power coefficient (c_p) and thrust coefficient (c_t) for an APC 9x6E propeller across a range of RPM values.

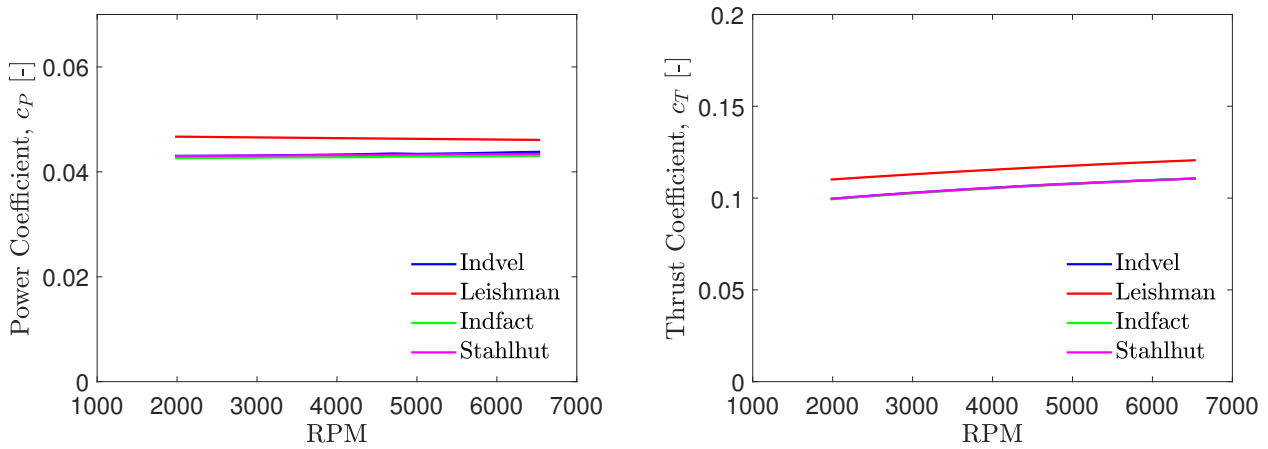
The results produced by the four solvers (*Indvel*, *Leishman*, *Indfact*, and *Stahlhut*) for both the power coefficient (c_p) and thrust coefficient (c_t) are remarkable for their similarity, as demonstrated by the overlapping lines in the plots. This close agreement indicates that all the solvers have been correctly implemented and

are yielding consistent and reliable results. The minor deviations observed can be explained by the different assumptions and methodologies employed by each solver.

A notable observation is the slight variation presented by the *Leishman* solver in comparison to the other solvers. This is a consequence of the strong assumptions adopted in its methodology for modelling the flow and rotor operation. Indeed, The *Leishman* solver linearizes the Blade Element Momentum Theory (BEMT) equations as much as possible by using small angle approximations, which introduces some differences in the results.

The comparison of these solvers is crucial in justifying the selection of one solver over the others for further analysis or simulations. *Leishman* solver will not be chosen to proceed with the validation since it provides less accurate results than the other solvers due to its assumptions and given that the solvers (*Indvel*, *Indfact* and *Stahlhut*) provide nearly identical predictions, the selection of one of these 3 solvers does not really matter but however the *Indvel* solver was selected to be used since it was the one used in the optimization process.

It is important to note that while the results are very similar across the solvers, computational time can differ depending on the solver and the methodology used in it. A detailed discussion of this topic is beyond the scope of the present research. However, it is worth mentioning that the *Indvel* solver is known to be computationally efficient compared to the others.



(a) Power coefficient (c_p) as a function of RPM for different solvers: *Indvel*, *Leishman*, *Indfact*, and *Stahlhut*.

(b) Thrust coefficient (c_t) as a function of RPM for different solvers: *Indvel*, *Leishman*, *Indfact*, and *Stahlhut*.

Figure 3.3: Comparison of power and thrust coefficients for APC 9x6E propeller using different solvers.

3.1.1 Results

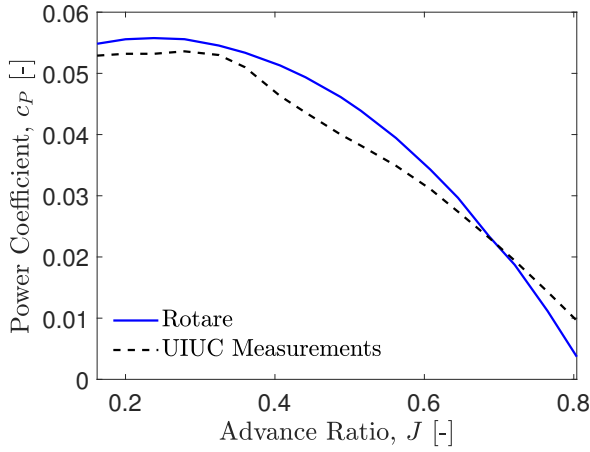
Figure 3.4 shows the results of the validation, comparing the experimental data and computational results for power coefficient (Figure 3.4a), thrust coefficient (Figure 3.4b) and efficiency (Figure 3.4c) in operational conditions.

Figures 3.4a and 3.4b show the power and thrust coefficients (c_p) predicted by ROTARE, which are generally in good agreement with the UIUC measurements across the range of advance ratios (J). ROTARE overestimates the power and thrust coefficients at low advance ratios, and this occurs because BEMT assumes idealized aerodynamic conditions that do not fully account for small-scale losses and three-dimensional effects, leading to

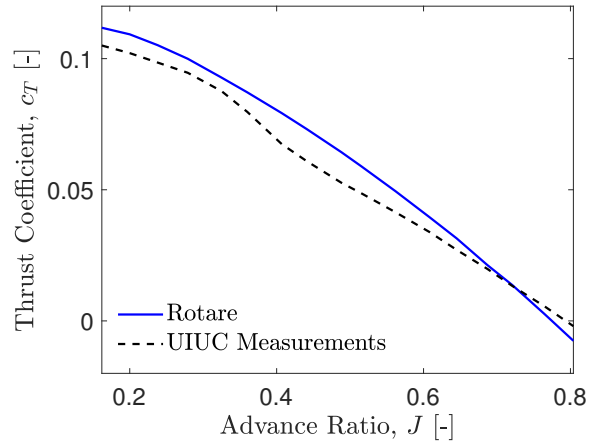
an overestimation of the thrust and power. Whereas at high advance ratios, ROTARE tends to underestimate the power and thrust coefficients due to the increasing complexity of the flow, including flow separation, wake interactions, and other unsteady aerodynamic effects that ROTARE does not capture, resulting in an underestimation of the thrust and power.

Additionally, Figure 3.4c shows the efficiency (η) predicted by ROTARE. At lower advance ratios, ROTARE accurately predicts efficiency because the flow conditions are simpler and align well with the assumptions of BEMT. As J increases, unmodeled effects like flow separation, wake interactions, and three-dimensional flow effects become more significant, leading to larger deviations between predicted and measured efficiency. However, the overall performance of ROTARE remains satisfactory for general design purposes, providing a good balance between accuracy and computational simplicity.

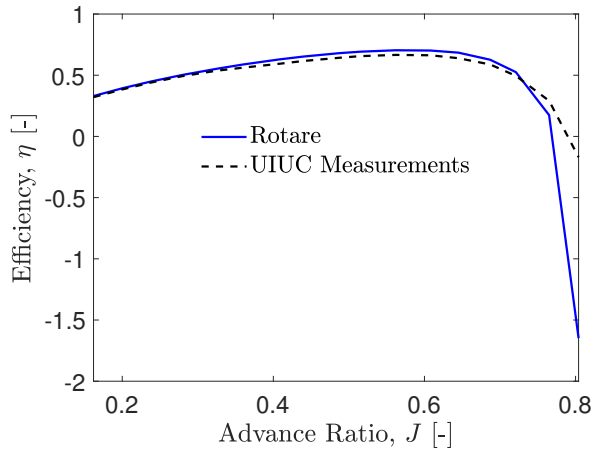
It is reasonable to notice differences between experimental data and computational results from ROTARE, and even more when applying a method such as BEMT that does not account for some phenomena present in propeller operation. Although some corrections are applied to account for the effects of rotations on the aerodynamics of the propeller airfoils, it is a semi-empirical correction that won't be accurate as a CFD simulation of the whole geometry of the propeller. Moreover, the method does not account for the roughness of the surface which influences the boundary layer and therefore the aerodynamic performance, nor it accounts for geometry deformation due to the aerodynamic forces acting on the propeller. Additionally, the quality of airfoil data obtained from XFOIL could be an important factor of these differences since the results become less precise at low Reynolds numbers regimes. The curves of the power coefficient, thrust coefficient and efficiency being very satisfactory and very close to the experimental data, then ROTARE can be assumed reliable.



(a) ROTARE predictions Vs UIUC measurements for power coefficient (c_P) as a function of advance ratio (J).



(b) ROTARE predictions Vs UIUC measurements for thrust coefficient (c_T) as a function of advance ratio (J).



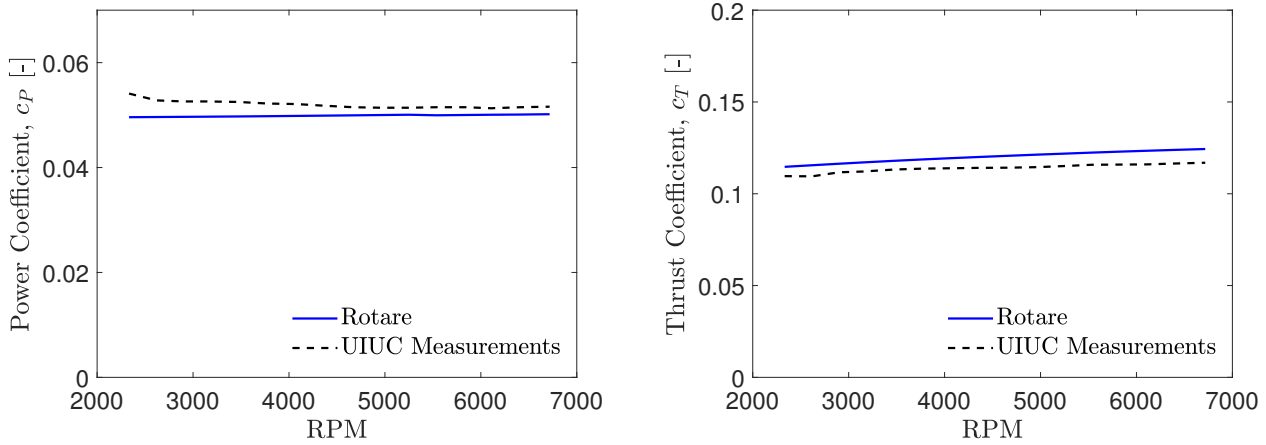
(c) ROTARE predictions Vs UIUC measurements for efficiency (η) as a function of advance ratio (J).

Figure 3.4: Comparison of ROTARE predictions and UIUC measurements for the APC 9x6E propeller in the operational conditions at $Re = [5e4, 1e6]$ and $RPM = 4000$.

On the other hand, Figure 3.5 illustrate the comparison between the ROTARE predictions and UIUC measurements for the power coefficient (c_P) and thrust coefficient (c_T) in static conditions (i.e., with an advance ratio $J = 0$).

The predictions by ROTARE are nearly identical to the experimental data, with only small deviations observed. These deviations can be attributed as mentioned just above to minor discrepancies in the modeling assumptions of BEMT, such as uniform inflow assumptions and the idealization of flow conditions.

Overall, the performance of ROTARE under operational and static conditions remains highly satisfactory, with the model providing accurate predictions for both power and thrust coefficients, making it reliable for initial design and analysis purposes where these small deviations are within acceptable limits.



(a) ROTARE predictions Vs UIUC measurements for power coefficient (c_P) as a function of RPM.

(b) ROTARE predictions Vs UIUC measurements for thrust coefficient (c_T) as a function of RPM.

Figure 3.5: Comparison of ROTARE predictions and UIUC measurements for the APC 9x6E propeller in the static case at $J = 0$.

Finally, a comparison was done in Figure 3.6, where the ROTARE BEMT predictions, UIUC measurements, and another BEMT code from the literature [28] for an APC 14x12E propeller under operational conditions were compared. The solver used in this case is the *Indfact* solver, as the method used in the literature matches the one implemented in this solver. However, it doesn't significantly matter since both *Indvel* and *Indfact* deliver similar results, as shown previously.

In Figure 3.6a, which compares the thrust coefficient (c_T) as a function of the advance ratio (J), the thrust coefficient predicted by ROTARE decreases steadily as the advance ratio increases. However, ROTARE consistently underestimates the thrust coefficient compared to both the UIUC measurements and the literature BEMT results across the entire range of advance ratios. The UIUC data follows a similar decreasing trend but shows higher c_T values than ROTARE, indicating that the ROTARE model might be missing some flow physics elements that contribute to higher thrust in real-world conditions. The literature BEMT code, on the other hand, provides thrust predictions that are closer to the UIUC measurements, particularly at lower advance ratios, suggesting that it might incorporate additional corrections or a more accurate aerodynamic model that better captures the physical phenomena at these conditions.

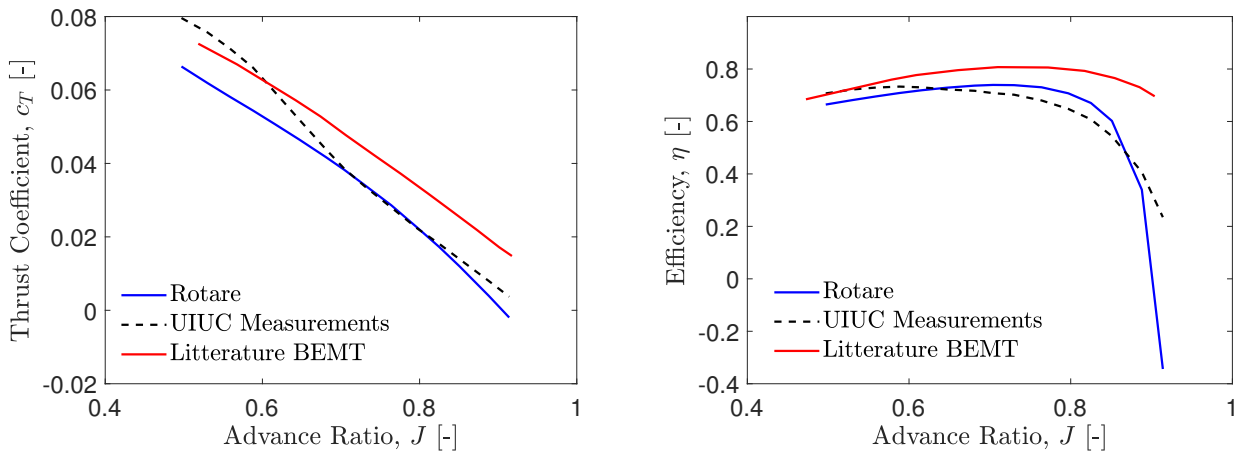
In Figure 3.6b, which shows the efficiency (η) as a function of advance ratio (J), the efficiency predicted by ROTARE increases up to a peak around $J = 0.7$ and then sharply decreases as J approaches 1. The sharp decline in efficiency at higher advance ratios may indicate that ROTARE underestimates thrust as J increases. The efficiency measured by UIUC exhibits a similar trend to the ROTARE predictions but with generally higher values, especially at higher advance ratios. This suggests that ROTARE is underestimating the overall performance, possibly due to the same reasons it underestimates the thrust coefficient. The BEMT code from the literature predicts a slightly different efficiency curve, peaking at a lower advance ratio and maintaining higher efficiency at larger J values. This difference may reflect variations in how losses and corrections are modeled in the different BEMT implementations. Additionally, the quality of the polars used in the BEMT codes to define the airfoil geometry could also be an important factor resulting in these differences with respect to the experimental data.

The discrepancy in the accuracy of the (BEMT) results between ROTARE and literature BEMT across different advance ratios (J ratios) can be attributed to the specific aerodynamic corrections applied in each study, which are tailored to different operating conditions.

Indeed, in the BEMT code used in literature, the BEMT model incorporates corrections that are particularly effective at low Reynolds numbers, which dominate at low J ratios. These include empirical adjustments that account for the limitations of BEMT in predicting thrust and power in low-speed conditions. The corrections address the increased influence of viscous effects and flow separation, which are more pronounced at low speeds. Additionally, the airfoil data used in the literature study is specifically selected or corrected for low Reynolds number conditions, ensuring that the aerodynamic characteristics, such as lift and drag coefficients, are representative of the actual performance under these conditions. This results in BEMT predictions that closely match experimental data at low J ratios.

Conversely, ROTARE applies corrections that enhance the accuracy of the BEMT model at high J ratios, where higher speeds and Reynolds numbers are prevalent. The corrections in this study include compressibility adjustments, which become significant as the blade tips approach transonic speeds. These adjustments modify the aerodynamic coefficients to account for changes in airflow characteristics under high-speed conditions. Furthermore, ROTARE considers the effects of blade sweep, which are critical at higher advance ratios. Swept blades exhibit different aerodynamic behavior, particularly in handling shock waves and drag at high speeds, and this correction helps the BEMT model predict performance more accurately in these regimes.

In conclusion, the results are similar but have small differences due to the quality of the airfoil data used and effects that ROTARE does not capture at low Reynolds numbers. The curves of ROTARE being very close to both experimental data and the other BEMT code, then ROTARE is still reliable to use for propeller analysis.



(a) Comparison of thrust coefficient (c_T) as a function of advance ratio (J).

(b) Comparison of efficiency (η) as a function of advance ratio (J).

Figure 3.6: Comparison of ROTARE predictions, UIUC measurements, and results from a BEMT code in the literature [28] for the APC 14x12E propeller in the operational conditions at $Re = [5e4, 1e6]$ and $RPM = 3500$.

3.2 Comparison with *Clark Y* propellers measurements

In addition to the UIUC data, the validation of ROTARE includes comparison with experimental data obtained by Biermann et al.[14]. The investigated propellers were all 3-bladed, had a diameter of 10 feet and were driven by a Curtiss Conqueror engine (GIV-1570). The propeller used is designed with the blade profile *Clark Y* (called 5868-9).

The Clark Y airfoil is a well-known and widely used airfoil shape characterized by a flat lower surface and a cambered upper surface. This design offers good lift characteristics and moderate drag, making it suitable for a variety of aeronautical applications. Biermann and Hartman's study involved wind tunnel testing of six full-scale propellers, each having different airfoil sections, including the Clark Y. The tests measured aerodynamic coefficients such as thrust, power, and efficiency across different advance ratios and RPM values.

During the tests, the propeller was maintained at constant rotational speed and the wind speed was increased up to 115 miles per hour. Higher values of the advance ratio were then obtained by decreasing the engine rotational speed until zero. Comprehensibility effects are not taken into account since the tip speeds are kept below 525 feet per second.

By incorporating the Clark Y propeller data, ROTARE's predictions can be further validated against a well-documented historical datasets. This provides an additional layer of validation, ensuring that ROTARE accurately models the aerodynamic performance of propellers with various airfoil sections under different operating conditions. The comparison will differ here from the one with UIUC measurements by varying the pitch collective angle and extracting results for these different collective angles as it was done in the experiments which will be beneficial because the ability of the ROTARE of representing stall will be analyzed.

3.2.1 Results

Figure 3.7 presents a comparison between ROTARE and experimental data from Biermann et al. for different pitch angles (collectives) between $[15^\circ - 45^\circ]$ across a range of advance ratios (J). The plots illustrate the power coefficient (c_p) and thrust coefficient (c_t) as functions of the advance ratio for various pitch angles, thereby facilitating an evaluation of the rotor's performance under diverse flight conditions and the ability of ROTARE to model stall behaviour..

Figure 3.7a shows the comparison in terms of the power coefficient (c_p), where the power coefficient is a function of the advance ratio for different pitch angles. ROTARE predictions generally follow the same trends as the experimental data from Biermann et al., with c_p increasing to a peak and then decreasing as the advance ratio increases, particularly at higher pitch angles. However, there is a noticeable difference between ROTARE and the experimental data, especially at higher pitch angles. ROTARE tends to predict higher power coefficients compared to the experimental data, particularly in regions closer to stall (lower advance ratios). This difference in outcome implies that ROTARE might not fully capture the complexities of stall and post-stall behavior, potentially overestimating the power required under these conditions. This behaviour again could be attributed to the assumptions made in the BEMT method and also to the quality of the airfoil data as explained previously.

Figure 3.7b shows the comparison in terms of the thrust coefficient (c_t), where the thrust coefficient is a function of the advance ratio for the same set of pitch angles. Similar to the power coefficient, the thrust coefficient predicted by ROTARE shows a general agreement with the trends observed in Biermann's experimental

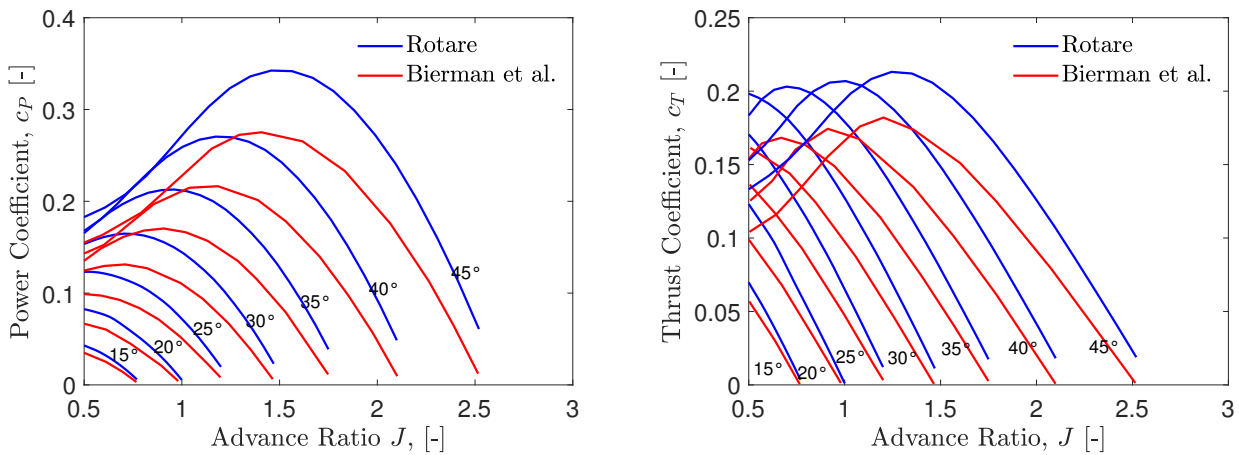
data, with a peak in c_t followed by a decline as J increases. However, ROTARE again overestimates the thrust coefficient, particularly at higher pitch angles and lower advance ratios. This overestimation may indicate that ROTARE predicts higher lift and thrust in regions where flow separation and stall effects become significant, which in turn gives rise to differences compared to the experimental data.

One significant observation is the increase in c_t and c_p as the pitch angle increases, which is indicative of stall behavior. This phenomenon occurs due to an increase in the angle of attack as the advance ratio decreases. The reduction in advance ratio, in turn, causes an increase in lift as the flow begins to separate, eventually leading to stall. The fact that ROTARE successfully captures this behavior demonstrates that the code is well-implemented and accurately predicts the correct aerodynamic trends.

While ROTARE effectively represents stall, there are inherent limitations. Although it captures the general trend of the data, including the onset of stall (indicated by the peaks in c_p and c_t), it tends to overestimate the aerodynamic coefficients as stall progresses. This suggests that the model might not fully account for the non-linearities and complex flow behaviors associated with deep stall, such as flow separation and vortex shedding. The comparison across different pitch angles demonstrates that ROTARE is effective at modeling various flight conditions, but care must be taken when interpreting results in regions prone to stall. The code appears to be more accurate in predicting performance at moderate advance ratios and pitch angles, where stall is less dominant.

A more detailed discussion could be conducted on the behavior near the stall region and the nominal point at the maximum, where the interaction between angle of attack, lift, and drag could be studied along the blade span. However, this analysis lies beyond the scope of the current research and was therefore not undertaken.

Overall, despite the differences observed, ROTARE still shows good results in predicting rotor performance across a range of conditions and can thus be considered reliable for propeller analysis.



(a) Comparison of power coefficient (c_p) as a function of advance ratio (J).

(b) Comparison of thrust coefficient (c_t) as a function of advance ratio (J).

Figure 3.7: Comparison of ROTARE predictions with experimental data from Biermann et al. [14] for the ClarkY airfoil at different pitch angles, $\theta = [15^\circ - 45^\circ]$.

3.3 Conclusion

The accuracy and reliability of ROTARE for single rotor applications were assessed by comparing its computational results with experimental data from UIUC and Biermann's studies. This assessment focused on key aerodynamic coefficients, including thrust (c_T), power (c_P), and efficiency (η), as well as the advance ratio (J) under various operating conditions. The validation confirmed that ROTARE is reliable and can accurately predict the performance of single rotors, thus establishing a strong foundation for further validation efforts involving more complex rotor systems, such as coaxial rotors.

While the validation of the single rotor is not extensively detailed in this chapter, given the scope of the research, the primary goal was to document the initial contributions made by the researcher during the early stages of the internship. For a comprehensive and detailed information on the validation process, concerning single isolated or coaxial rotor methods, readers are encouraged to consult Robin Tamburrini's thesis which is dedicated to the validation of ROTARE and is to be published in September 2024.

Chapter 4

Optimal design point

4.1 Introduction

Now that ROTARE was validated for both single isolated and coaxial rotor systems and can be considered reliable for propeller analysis, the optimization of coaxial rotor performance will proceed. The ROTARE BEMT code will be refined and modified using various strategies aimed at enhancing rotor performance.

The optimization process will be conducted in two phases. In the first phase, the goal will be to identify the optimal configuration or design point of the rotor that achieves a target thrust of $T = 6\text{ kg}$ and a target Thrust to power ratio T/P of 12.5 g/W , without altering the blade geometry. To achieve this, ROTARE will be refined and subjected to iterative processes, which will be detailed later in a dedicated section, in order to accurately determine the optimal configuration. In this phase, operational parameters will be optimized to maximize rotor efficiency while maintaining the existing blade geometry.

The second phase of the optimization, presented in chapter 5, will focus on improving the blade geometry itself. Once the optimal configuration is identified through the first phase, its geometry will be optimized to assess whether these modifications, such as adjustments to the twist and chord distribution along the blade span, can further enhance the overall performance of the drone.

Moreover, The term "configuration" refers to the pair (θ, RPM) , where θ is the collective pitch angle and RPM is the rotational speed of the rotor. Indeed, in the coaxial rotor system that will be analyzed, there are four degrees of freedom: the collective pitch and RPM for both the upper and lower rotors. The goal of this optimization process is to control and optimize these four degrees of freedom to find the best possible configuration for the desired operating conditions, specifically for achieving a thrust of 6 kg during hover.

The key parameters of interest during this optimization process will include the $\frac{c_P}{c_T}$ ratio, which will be maximized to identify the optimal configuration, and the $\frac{T}{P}$ ratio, which is essential for performance evaluation.

The studied blades are real-life blades called, SAB280, ALZRC325, ALZRC380 and BL450 and are symmetric, untwisted, and have a constant chord, with detailed specifications provided in *Appendix A*. These blades are designed and usually used in drone applications [5], [4], [6], [31]. The optimization process will be systematically applied to one of the four blades, with detailed results for this specific blade provided in the main body of the research. The general results for the other blades, obtained using the same methodology, will be

documented in *Appendix B*.

4.2 Blade configuration Set-up

Before running a simulation in ROTARE to compute the performance of the blades, their configuration must be implemented correctly, considering the appropriate assumptions, flow models, and solvers. The performance of the blades is computed using the principles detailed in the theoretical background in Chapter 2. The type of solver used throughout the optimization process is the *Indvel* solver, which was also detailed in Section 2.3.2.

In this setup, the power, thrust, and torque coefficients which are the main key parameters of the optimization are computed using the helicopter standard relations represented in Table 3.1. Moreover, a multiple streamtube (MST) flow model, detailed in section 2.2.1, is employed to simulate the aerodynamic behavior of the blades. To simplify the study, hub and tip losses will not be taken into account during the optimization process. This decision is made because the optimization conducted in this research represents a simplified initial optimization phase, intended to open up various pathways and strategies that could be explored in future studies to further improve performance and enhance ROTARE.

The blades, which are symmetric, untwisted, and have a constant chord, are modeled within ROTARE based on these geometric properties. Moreover, as can be seen in Figure 4.1, they are not fixed at $r = 0$, but at an initial radius of 10 cm, as they are not directly attached to the hub. The simulation process involves inputting the desired operating conditions, such as rotational speed and thrust requirements, and the blade's geometric parameters taking into account the offset of the radius position. ROTARE then iteratively solves the BEMT equations to predict performance characteristics, including the thrust coefficient (c_T) and the power coefficient (c_P). These predictions serve as the foundation for the subsequent optimization phases, where the goal is to refine and enhance the blade's operational efficiency.

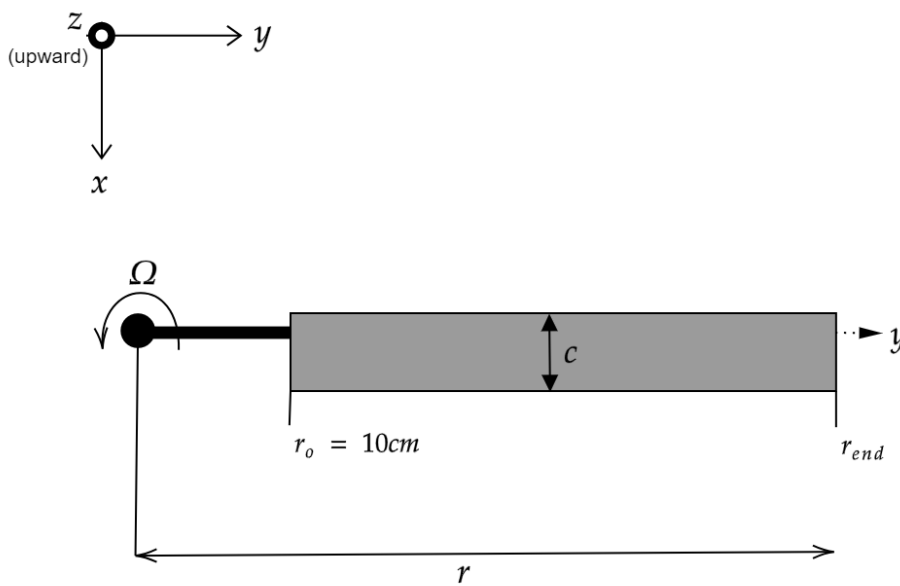


Figure 4.1: Configuration set-up of the simulated blade.

The blade that will be detailed in this chapter is the SAB280mm, which is 280 mm long and has a chord of 25 mm with an airfoil thickness of 3.5 mm, representing 14% of the blade chord. The airfoil type used for this blade is the Selig S8035 [9].



Figure 4.2: SAB 280mm blade and its corresponding airfoil shape, Selig S8035.

4.3 Strategy

Before the detailed explanation of the optimization steps is provided, a flowchart summarizing the overall strategy will be presented. This flowchart presented in Figure 4.3, outlines the sequence of key steps involved in identifying the optimal design point for the coaxial rotor system. It serves as a visual guide to the process, clarifying the methodical approach that will be employed to achieve the desired rotor configuration. Each step in the flowchart will be explained in detail in the subsequent sections.

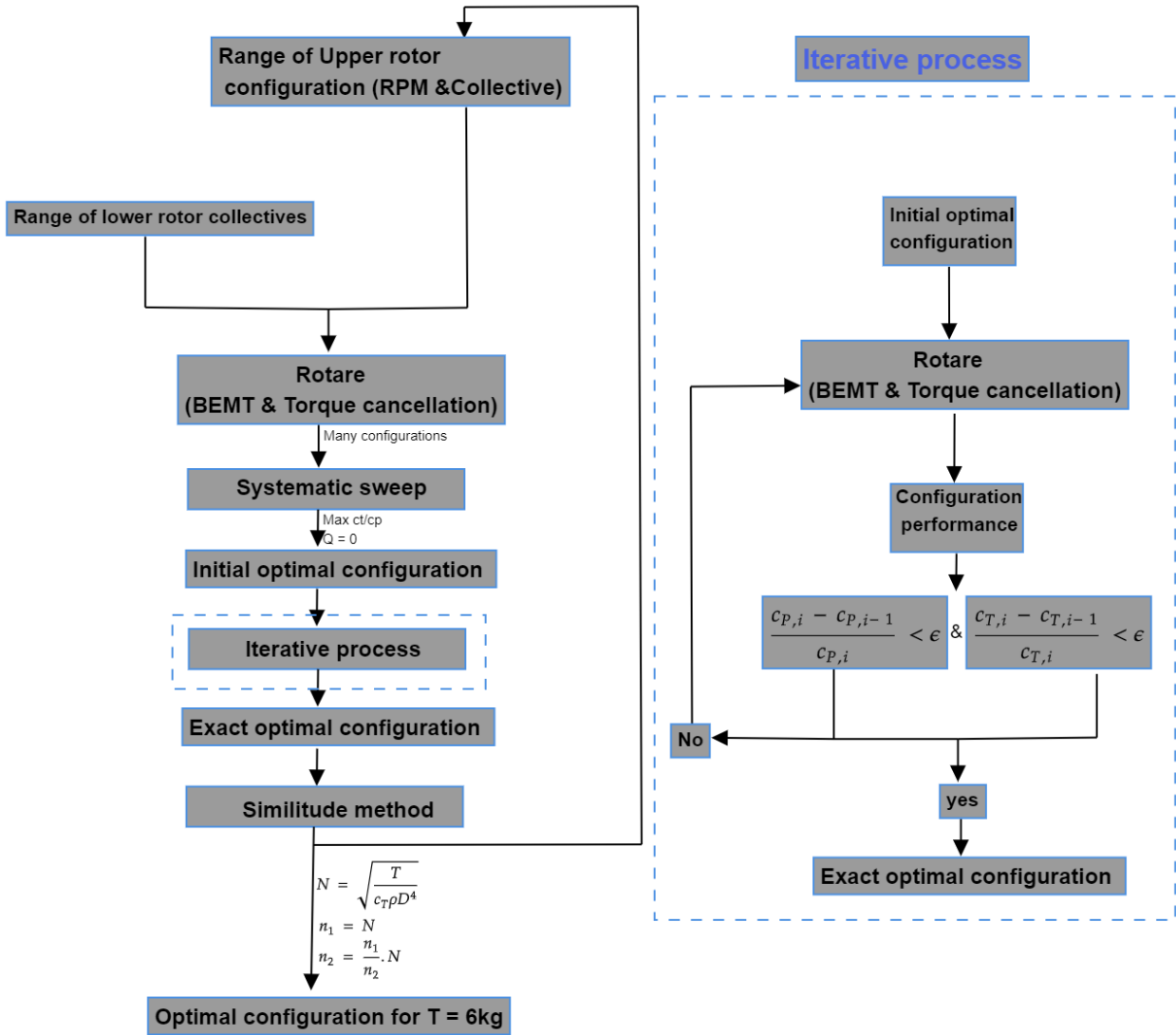


Figure 4.3: Flowchart of the optimization process.

4.3.1 Torque cancellation

The first step of the optimization strategy involves ensuring torque cancellation between the upper and lower rotors. This strategy relies on using the Blade Element Momentum Theory (BEMT) as the core aerodynamic model to compute the performance of the coaxial rotor system. The primary objective of this phase is to achieve torque cancellation between the upper and lower rotors, which is essential for eliminating the need for a tail rotor or additional control systems to counteract torque.

The goal of torque cancellation is to determine the state of the lower rotor such that the torque it produces matches and cancels the torque generated by the upper rotor. To achieve this, the following approach is adopted:

- **Upper rotor performance calculation:** The performance of the upper rotor is computed using the BEMT equations. This includes calculating the aerodynamic parameters associated with the upper rotor, such as thrust, power, and most importantly, torque (Q_{upper}).
- **Lower rotor configuration:** Once the upper rotor's torque is known, the configuration of the lower rotor must be determined. This involves calculating the lower rotor's performance using the BEMT equations. However, to ensure that the lower rotor generates a torque that matches and cancels the upper rotor's torque, an iterative process is required.
- **Iterative process - Secant method:** The iterative process used is the Secant Method, which is combined with the BEMT equations to adjust the configuration of the lower rotor. The goal is to find a configuration where the lower rotor's aerodynamic parameters, particularly torque, exactly match the upper rotor's torque in magnitude but with the opposite direction. To do so the following steps are applied:

1. **Iterations:** The method begins with two initial guesses for the variable to be adjusted:

- If the strategy is to adjust the RPM, the initial guesses are set to $RPM_{upper} - 100$ and $RPM_{upper} + 100$.
- If the strategy is to adjust the collective pitch, the initial guesses are set to $\theta_{upper} - 1^\circ$ and $\theta_{upper} + 1^\circ$.

Here, RPM_{upper} and θ_{upper} refer to the RPM and collective pitch of the upper rotor, respectively.

Throughout the optimization process in this research, the second strategy is employed, where the collective pitch of the lower rotor is adjusted iteratively to achieve the desired torque cancellation.

2. **Function evaluation:** For each iteration, the BEMT equations are solved to compute the torque of the lower rotor. The function to be minimized is the difference between the torque of the upper rotor (Q_{upper}) and the torque of the lower rotor (Q_{lower}), i.e., $f(x) = Q_{upper} - Q_{lower}$.

3. **Secant update:** The next guess for the variable (e.g., RPM or collective pitch) is calculated using the Secant update formula:

$$x_{n+1} = x_n - \frac{f(x_n) \cdot (x_n - x_{n-1})}{f(x_n) - f(x_{n-1})}$$

where x_n and x_{n-1} are the current and previous guesses, and $f(x_n)$ and $f(x_{n-1})$ are the corresponding function evaluations (torque differences).

4. **Convergence:** The iterative process continues until the difference between the torques of the upper and lower rotors is within a specified convergence criterion, defined as:

$$\text{Convergence Criterion} = \left| \frac{Q_{upper} - Q_{lower}}{Q_{upper}} \right| < \varepsilon$$

where $\varepsilon = 10^{-3}$ is the tolerance.

By applying the Secant Method in this manner, the lower rotor's configuration is adjusted to ensure that its torque cancels the torque of the upper rotor, thereby achieving the desired torque balance in the coaxial rotor system.

This torque cancellation strategy is indispensable in the design of a coaxial rotor system because it eliminates the need for a tail rotor or a complex control system to counteract the torque produced by the rotors.

By ensuring that the lower rotor's torque cancels the upper rotor's torque, the system can achieve stable and efficient operation without the additional weight and complexity of a tail rotor or other torque-compensation mechanisms.

Finally, a flowchart is presented in Figure 4.4 to visually summarize the key steps involved in this process. This flowchart will outline the sequence of actions done to achieve torque cancellation between the upper and lower rotors.

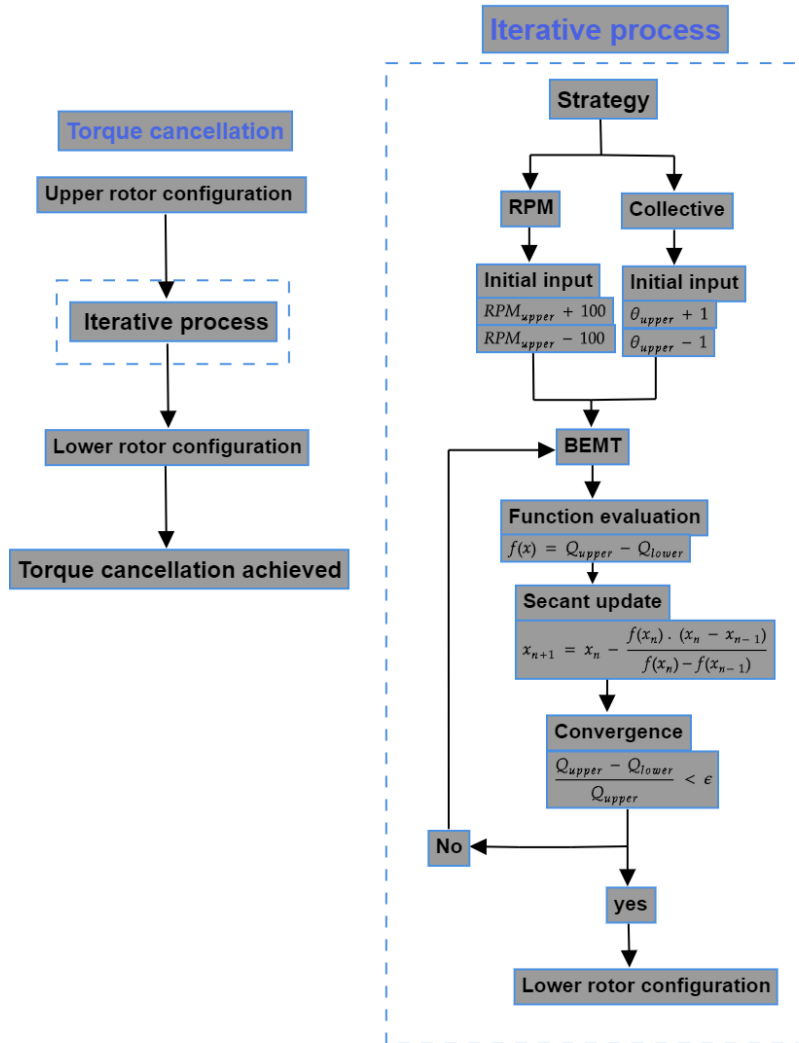


Figure 4.4: Flowchart summarizing the steps for achieving torque cancellation between the upper and lower rotors.

4.3.2 Non-Dimensionalization

The computed power and thrust coefficients of both the lower and upper rotors are non-dimensionalized with respect to the upper rotor RPM. This means that the thrust coefficient (c_T) and the power coefficient (c_P) for both rotors are calculated based on the RPM of the upper rotor.

Non-dimensionalizing the coefficients with respect to the upper rotor RPM provides several benefits:

- **Uniform basis for comparison:** By using a common reference (RPM_{upper}), the performance of the upper

and lower rotors can be directly compared within the same framework. This uniform basis is crucial for optimizing the system, as it allows the impact of changes in the lower rotor configuration to be assessed relative to the fixed conditions of the upper rotor.

- **Consistency in performance metrics:** Using the upper rotor RPM as the reference ensures that the calculated c_T and c_P values for both rotors are consistent across different simulations. This consistency is essential for accurately comparing different configurations and ensuring that the optimization process yields meaningful results.

The standard helicopter relations used to non-dimensionalize the thrust coefficient (c_T) and power coefficient (c_P) are as follows:

$$c_T = \frac{T}{\rho \cdot \pi \cdot R^2 \cdot (\text{RPM}_{\text{ur}} \cdot R)^2}$$

$$c_P = \frac{P}{\rho \cdot \pi \cdot R^2 \cdot (\text{RPM}_{\text{ur}} \cdot R)^3}$$

where:

- T is the thrust generated by the rotor,
- P is the power consumed by the rotor,
- ρ is the air density,
- R is the rotor radius,
- RPM_{ur} is the rotational speed of the upper rotor.

4.3.3 Systematic Sweep

The systematic sweep represents the second step of the strategy for finding the optimal design point. The term "Systematic Sweep" refers to a methodical approach in which a range of parameters is varied systematically to explore all possible configurations or outcomes. This method allows for a comprehensive analysis of different setups to identify the optimal configuration according to a defined performance criterion.

After applying the torque cancellation strategy, the system is now balanced, allowing us to compute as many configurations as desired. The main goal of this section is to find the configuration that maximizes the total $\frac{c_T}{c_P}$ ratio of both rotors. Additionally, the systematic sweep aims to identify the optimal quadrant within the design space, where the exact optimal configuration can be refined and determined in later stages of the optimization process.

The systematic sweep is implemented in the core of ROTARE. This sweep involves varying the collective pitch of the lower rotor across a specified range while keeping the upper rotor configuration fixed. When the collective pitch of the lower rotor is varying to account for different configurations, the RPM is automatically computed using the secant method to ensure torque cancellation with the upper rotor. The performance metrics, particularly the thrust coefficient (c_T) and power coefficient (c_P), are then computed for each configuration. These coefficients are then non-dimensionalized with respect to the upper rotor's RPM ($\text{RPM}_{\text{upper}}$) as discussed

in Section 4.3.2.

The systematic sweep method allows for a thorough exploration of the possible lower rotor configurations, ensuring that the optimal configuration is identified. By varying the collective pitch over a defined range and using the Secant Method to ensure torque cancellation, the method effectively balances the need for torque equilibrium with the goal of maximizing aerodynamic efficiency.

The systematic sweep also serves a strategic purpose: it helps in identifying the optimal quadrant within the design space, where the exact optimal configuration should be located. This initial identification allows for a more focused and refined optimization process in subsequent stages, where fine-tuning within this quadrant can lead to the precise determination of the best rotor configuration.

Thus, this method helps to identify the way to be taken in order to get directly to the optimal point by sampling all the possibilities and eliminating those that are not desired.

The process of systematic sweep implemented within ROTARE can be described as follows:

1. **Upper rotor configuration:** Let the upper rotor configuration be defined by its RPM ($\text{RPM}_{\text{upper}}$) and collective pitch (θ_{upper}). These values are kept constant throughout the sweep.
2. **Lower rotor collective pitch range:** For the fixed upper rotor configuration, the collective pitch of the lower rotor (θ_{lower}) is varied systematically within a defined range:

$$\theta_{\text{lower}} \in [\theta_{\text{upper}} - 10^\circ, \theta_{\text{upper}} + 10^\circ]$$

This range allows the exploration of lower rotor configurations that are slightly less or more aggressive in pitch compared to the upper rotor.

3. **Torque cancellation and RPM adjustment:** For each value of θ_{lower} within the specified range, the RPM of the lower rotor ($\text{RPM}_{\text{lower}}$) is calculated such that the torque of the lower rotor (Q_{lower}) cancels the torque of the upper rotor (Q_{upper}). This involves solving the following 'Secant Method' equation iteratively:

$$Q_{\text{upper}}(\text{RPM}_{\text{upper}}, \theta_{\text{upper}}) = Q_{\text{lower}}(\text{RPM}_{\text{lower}}, \theta_{\text{lower}})$$

The Secant Method is used to adjust $\text{RPM}_{\text{lower}}$ until the torques match, ensuring that the system is balanced.

4. **Performance metrics calculation:** Once the correct $\text{RPM}_{\text{lower}}$ is found for each θ_{lower} , the performance metrics are computed. Specifically, the thrust coefficient (c_T) and power coefficient (c_P) for both rotors are calculated using the BEMT equations and then non-dimensionalized. The total $\frac{C_T}{C_P}$ ratio for the system is then given by:

$$\left(\frac{C_T}{C_P} \right)_{\text{total}} = \frac{C_{T,\text{upper}} + C_{T,\text{lower}}}{C_{P,\text{upper}} + C_{P,\text{lower}}}$$

This ratio is a key performance indicator that reflects the aerodynamic efficiency of the rotor system.

5. **Optimization:** The goal of the systematic sweep is to identify the lower rotor configuration that maxi-

mizes the total $\frac{C_T}{C_P}$ ratio. Mathematically, this involves finding:

$$\max_{\theta_{\text{lower}} \in [\theta_{\text{upper}} - 10^\circ, \theta_{\text{upper}} + 10^\circ]} \left(\frac{C_T}{C_P} \right)_{\text{total}}$$

This process results in a set of lower rotor configurations, from which the optimal configuration is selected based on the highest total $\frac{C_T}{C_P}$ ratio. Identifying this optimal configuration also helps in determining the quadrant within the design space where the exact optimal configuration should be found and refined in subsequent stages of the optimization process.

The mathematical foundation of this approach, combined with its implementation in ROTARE, ensures that the resulting rotor configurations are both balanced and optimized. Thus, for each fixed upper rotor configuration, an optimal lower rotor configuration is found. The systematic nature of the sweep means that even subtle variations in rotor performance can be detected, allowing for fine-tuned optimization of the rotor system.

4.3.4 Exact rotor configuration

Now that the first two steps of the strategy have been explained—where the second step involved a systematic sweep to identify a near-optimal configuration of the lower rotor for a given upper rotor configuration—the third step focuses on refining this configuration. The second step provided a starting point by determining an optimal configuration composed of discrete values. However, to find the exact optimal configuration, a more precise iterative approach is necessary.

This step involves applying another iterative process within the core of ROTARE on the optimal configuration identified in the second step (Section 4.3.3). The initial optimal configuration found in the systematic sweep is composed of discrete values for the lower rotor's collective pitch and RPM. While this configuration is close to optimal, further refinement is needed to achieve the exact optimal configuration.

This refinement process is conducted using again the Secant Method in combination with the BEMT equations, similar to the torque cancellation strategy. The key difference here is that the focus is now on fine-tuning the configuration to maximize the performance metrics rather than merely balancing the torque.

The iterative refinement process can be described as follows:

1. **Initial optimal configuration:** The starting point for this refinement process is the optimal configuration identified in the second step, which includes specific values for the lower rotor's collective pitch (θ_{lower}) and RPM ($\text{RPM}_{\text{lower}}$).
2. **Secant method application:** The Secant Method is applied iteratively to refine the collective pitch and RPM values of the lower rotor. For each iteration, the BEMT equations are used to recalculate the thrust coefficient (C_T) and power coefficient (C_P). The objective is to iteratively adjust the lower rotor's parameters to maximize the total $\frac{C_T}{C_P}$ ratio:

$$\left(\frac{C_T}{C_P} \right)_{\text{total}} = \frac{C_{T,\text{upper}} + C_{T,\text{lower}}}{C_{P,\text{upper}} + C_{P,\text{lower}}}$$

The refinement process continues until the difference between consecutive iterations is within a predefined convergence criterion. Specifically, the Secant Method continues iterating until:

$$\left| \frac{c_{T,i} - c_{T,i-1}}{c_{T,i}} \right| < \varepsilon \quad \text{and} \quad \left| \frac{c_{P,i} - c_{P,i-1}}{c_{P,i}} \right| < \varepsilon$$

where $\varepsilon = 10^{-3}$, ensuring that the solution is sufficiently accurate.

The configuration at this point is considered the exact optimal configuration for the lower rotor, as it has been fine-tuned to maximize the aerodynamic efficiency of the coaxial rotor system.

This third step in the optimization strategy is crucial for achieving the highest possible performance from the rotor system. While the systematic sweep identifies a close-to-optimal configuration, the iterative refinement process fine-tunes the solution to ensure that no further improvements can be made.

By combining the Secant Method with the BEMT equations, ROTARE is able to precisely adjust the rotor parameters and maximize the $\frac{c_T}{c_P}$ ratio. This approach ensures that the final configuration not only balances the torques between the rotors but also provides the best possible aerodynamic efficiency, which is critical for the performance of coaxial rotor systems.

4.3.5 Similitude method

Now that ROTARE is capable of determining the optimal configuration of the coaxial rotor for any given configuration of the upper rotor, it will be applied to the real blades available to us in order to obtain their optimal configurations and aerodynamic performances. This step is particularly important as it helps us find the exact optimal configuration required for the blades to hover at a thrust of 6 kg. It is crucial to remember that the optimization process described here is performed for a steady state of the drone, specifically during hover.

The Similitude Method, which is a form of dimensional analysis, serves as the final step in the first phase of optimization. The main objective is to determine the exact RPM values for both the upper and lower rotors that will allow the system to hover at the desired thrust of 6 kg. The process can be described as follows:

1. **Looping through upper rotor configurations:** The first part of this step involves looping through various configurations of the upper rotor. For each configuration of the upper rotor, the optimal configuration of the lower rotor is determined using the refined ROTARE code developed in the previous steps. This involves maximizing the $\frac{c_T}{c_P}$ ratio while ensuring that the torque is canceled ($Q = 0$).
2. **Determining optimal lower rotor configuration:** For each iteration of the loop, the refined ROTARE code is used to find the optimal configuration of the lower rotor. This is done by applying the following two conditions:
 - Maximizing the $\frac{c_T}{c_P}$ ratio.
 - Ensuring that the torque is canceled, meaning $Q_{\text{upper}} + Q_{\text{lower}} = 0$.

After running the loop, multiple optimal configurations for the lower rotor are obtained for various upper rotor configurations. Thanks to the computed configurations, a plot of the curves $\frac{c_T}{c_P}$ as a function of the upper rotor collective pitch can be traced and also the curves of $\frac{T}{P}$ as a function of thrust can be traced. These plots are useful for graphically determining the configuration at which the system should

operate for the desired thrust of 6Kg, these figures are represented in section 4.5. To compute the exact configuration for $T = 6$ kg, the process is explained in the third step, which is the 'Application of the Similitude Method'.

3. **Application of the similitude method (Dimensional Analysis):** It is important to note that the optimal configurations obtained at the end of the previous steps, although it may be optimal in terms of maximizing the $\frac{c_T}{c_P}$ ratio and canceling torque, do not necessarily provide the exact thrust required, which is 6 kg. Each configuration give a different thrust value and thus this will help us to draw the curves T/P as a function of the thrust generated by these configurations. This is precisely why the Similitude Method, grounded in dimensional analysis, is employed. Once the best optimal configuration has been identified from the refined ROTARE code, the Similitude Method, which involves dimensional analysis, is applied to find the exact RPM values for both the upper and lower rotors to achieve a thrust of 6 kg. The Similitude Method relies on the RPM ratio between the upper and lower rotors, which remains constant across all the optimal configurations found in previous steps because when the rpm of the upper rotor was modified, the rpm of the lower rotor is adjusted to this modification in order to give a total torque of zero and that is why $Q_{tot} = 0$ was one of the conditions of the optimization process.

The exact RPM values for the upper and lower rotors are determined using the following approach:

1. **Determination of the RPM ratio:** Let n_1 represent the RPM of the upper rotor and n_2 represent the RPM of the lower rotor. The RPM ratio between the two rotors is constant, denoted as:

$$\text{RPM Ratio} = \frac{n_2}{n_1} \quad (4.1)$$

This ratio is calculated and stored during the previous optimization steps for each optimal configuration.

2. **Thrust and RPM calculation:** To determine the exact RPM values required for a thrust of 6 kg, we use the following relationship between thrust T and the thrust coefficient c_T , which is derived from the dimensional analysis:

$$T = c_T \cdot \rho \cdot N^2 \cdot D^4 \quad (4.2)$$

This equation is derived by expressing the thrust coefficient c_T as a dimensionless quantity that relates the actual thrust produced by the rotor to the dynamic pressure and the rotor's disk area.

The thrust coefficient c_T is defined as:

$$c_T = \frac{T}{\frac{1}{2} \rho V_t^2 A} \quad (4.3)$$

where V_t is the tip speed, ρ is the air density, and $A = \pi R^2$ is the rotor disk area.

The tip speed V_t is related to the rotor RPM, N_{rot} and diameter, D by:

$$V_t = \omega R = \left(\frac{2\pi N_{rot}}{60} \right) \frac{D}{2} \quad (4.4)$$

Substituting the expression for V_t into the thrust coefficient equation, and solving for T , we obtain:

$$T = c_T \cdot \rho \cdot N_{rot}^2 \cdot D^4 \quad (4.5)$$

Where:

- T is the thrust,
- ρ is the air density,
- N_{rot} is the rotational speed in revolutions per second,
- D is the rotor diameter,
- c_T is the thrust coefficient.

Using this relation, the RPM of the upper rotor n_1 can be determined as:

$$n_1 = \sqrt{\frac{T}{c_T \cdot \rho \cdot D^4}} \quad (4.6)$$

The RPM of the lower rotor n_2 is then calculated using the RPM ratio:

$$n_2 = \text{RPM Ratio} \times n_1 \quad (4.7)$$

This calculation gives the exact RPM values needed to achieve the desired thrust of 6 kg with the optimal aerodynamic efficiency.

3. **Final configuration:** These RPM values, n_1 and n_2 , represent the exact rotational speeds needed for the upper and lower rotors to achieve the desired hover thrust of 6 kg with optimal aerodynamic efficiency.

The Similitude Method provides a robust framework for determining the exact RPM values needed to achieve a specific thrust, in this case, 6 kg, while maintaining optimal aerodynamic performance. By leveraging the constant RPM ratio between the upper and lower rotors, this method ensures that both rotors operate at their most efficient points. The systematic approach of looping through different configurations and refining them using ROTARE guarantees that the final configuration is not only balanced in terms of torque but also optimized for performance.

The advantage of this method lies in its flexibility; if, in the future, the manufacturer decides to change the imposed thrust due to modifications in the payload—whether increasing or decreasing the thrust requirement—the Similitude Method can be easily reapplied to adjust the RPM values accordingly without having to restart the entire optimization process.

There are indeed other methods to obtain the optimal configuration for a specific thrust, such as 6 kg, but the Similitude Method remains advantageous for the reason mentioned above. One alternative method that could have been used involves following a similar process where, for a given upper rotor configuration, the optimal lower rotor configuration is found as explained before. Then, instead of using the Similitude Method, the thrust of this configuration could be adjusted to 6 kg iteratively by adjusting the RPM of the upper rotor.

The advantage of this alternative method is that it directly finds the correct Reynolds number, as the thrust is adjusted to the desired value during the iterative process. However, the downside is that if the required thrust changes in the future, the entire iterative process would need to be restarted from the beginning, in contrast to the Similitude Method, which allows for a simple adjustment based on the new thrust requirement.

4.4 Implementation

All the steps described in the optimization process were implemented in MATLAB for the four blades of the coaxial rotor system presented in Appendix A. The discussion of results in this chapter will focus on one of these four blades, with similar procedures applied to the others. The simulations were conducted over a range of rotational speed values of the upper rotor between 500 and 6000 RPM, which corresponds to the operational capacity range of the drone motor in question. Additionally, the collective pitch of the upper rotor was varied between 1° and 17° . For each combination of upper rotor collective pitch and RPM, an optimal configuration for the lower rotor was determined using the methods outlined earlier.

It is important to note that the results for the other blades, which are presented in the Appendix B, present generally the same tendencies and behaviors.

The implementation ensured that for every upper rotor configuration, the lower rotor's RPM and collective pitch were adjusted iteratively to achieve torque cancellation and maximize the c_T/c_P ratio, following the systematic sweep and similitude methods. The results presented in the following sections reflect the outcomes of these optimizations, highlighting the performance characteristics of the selected blade (SAB280) under various operating conditions.

4.5 Results

Before going into the detailed analysis of the results, note that for each upper rotor configuration presented in the following figures, the corresponding optimal configuration for the lower rotor has been determined through the methods described in previous sections. These optimal lower rotor configurations, including their specific collective pitch and RPM values, are provided in details in Table B.1 located in the Appendix B.

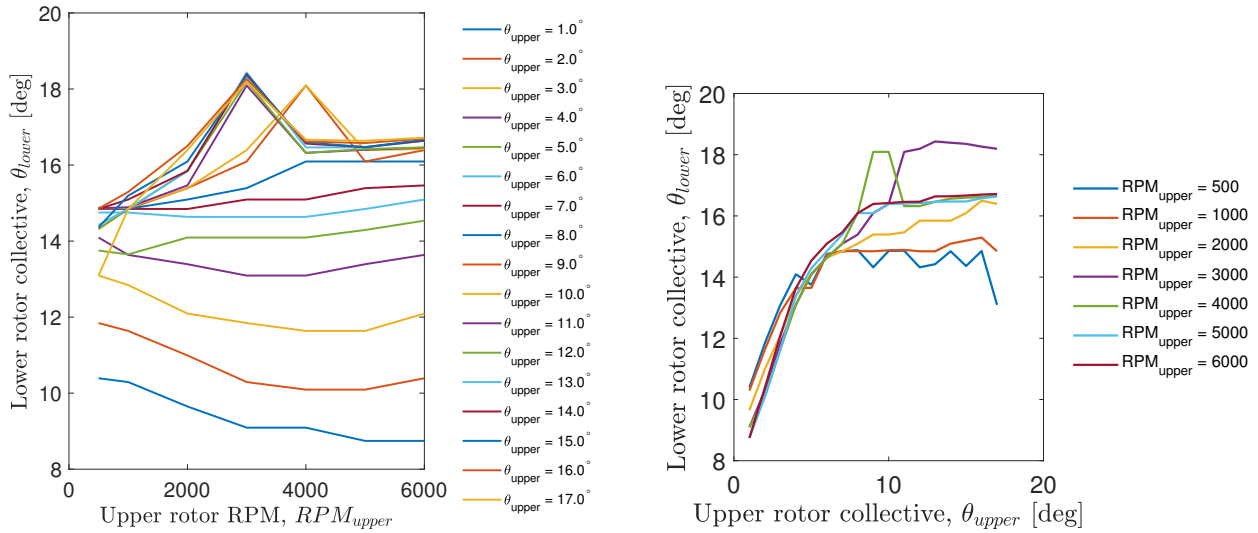
4.5.1 Variation of θ_{lower} with $\text{RPM}_{\text{upper}}$ and θ_{upper}

The variation of the lower rotor collective pitch (θ_{lower}) with respect to the upper rotor RPM ($\text{RPM}_{\text{upper}}$) and upper rotor collective pitch (θ_{upper}) is crucial for understanding the rotor system's performance and stability. As shown in Figures 4.5a and 4.5b, a general trend can be observed where the lower rotor collective pitch decreases as the upper rotor RPM increases. This decrease occurs because an increase in RPM leads to a higher axial velocity component in the airflow, thereby increasing the thrust produced by the upper rotor. To maintain torque balance between the rotors, the lower rotor's collective pitch must be reduced accordingly. However, this relationship is not linear across all operating conditions. At lower upper rotor RPMs and collective pitches, the adjustment of θ_{lower} is relatively smooth and predictable. As θ_{upper} increases, the lower rotor collective pitch must increase to counterbalance the higher thrust generated by the upper rotor. This trend is straightforward at lower RPMs, where the aerodynamic forces are more easily controlled.

As θ_{upper} reaches higher values, particularly beyond approximately 13° , the behavior of the lower rotor collective pitch becomes more complex and even chaotic. At these high collective pitches, small changes in θ_{upper} can lead to significant and sometimes unpredictable changes in the lower rotor collective pitch. The chaotic behavior seen in the lower rotor collective pitch at high upper rotor collective angles can be explained by the complex and non-linear aerodynamic effects that occur at these operating conditions. While BEMT simplifies the analysis by treating the rotors in isolation and assuming steady flow, the actual aerodynamic environment

is far more complex. This complexity, particularly at high RPMs, leads to instability in the system's response, manifesting as the erratic variations observed in the plots.

It might appear from the plots that the lower rotor collective pitch remains constant for certain ranges of θ_{upper} and $\text{RPM}_{\text{upper}}$. However, this is not the case. The variation in the optimal value of θ_{lower} is indeed present but is not significant enough to be clearly visible on the plots. The detailed values of θ_{lower} and the corresponding $\text{RPM}_{\text{lower}}$ are provided in Table B.1 in Appendix B.



(a) Lower rotor collective pitch angle as a function of upper rotor RPM at $\theta_{\text{upper}} = 1^\circ - 17^\circ$.

(b) Lower rotor collective pitch angle as a function of upper rotor collective pitch angle at $\text{RPM} = 500 - 6000$.

Figure 4.5: Lower rotor collective pitch angle variation for the SAB 280mm blade. Blade parameters: $L = 280\text{ mm}$, $c = 25\text{ mm}$, airfoil: Selig S8035, $r_0 = 100\text{ mm}$, $r_{\text{end}} = 290\text{ mm}$.

4.5.2 Variation of $\text{RPM}_{\text{lower}}$ with $\text{RPM}_{\text{upper}}$ and θ_{upper}

As shown in Figure 4.6a, the lower rotor RPM increases with the upper rotor RPM, but the rate of increase is dependent on the upper rotor's collective pitch. At low θ_{upper} , the lower rotor RPM increases more slowly, while at high θ_{upper} , the increase is more rapid. This reflects the need for the lower rotor to match the torque of the upper rotor, which requires higher RPMs as the upper rotor's thrust (and thus torque) increases with both RPM and collective pitch.

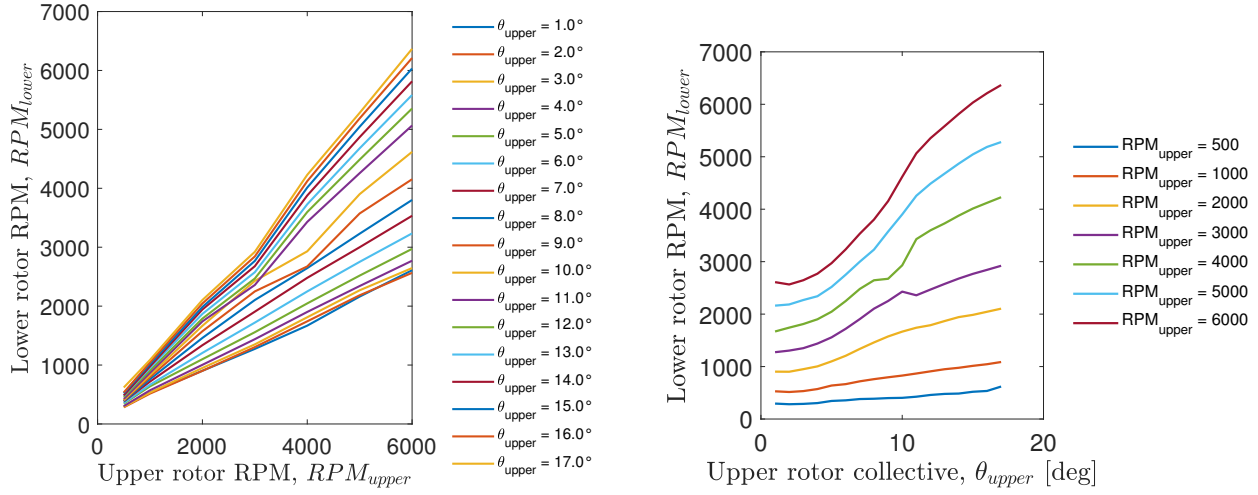
Figure 4.6b also shows that as θ_{upper} increases, the lower rotor RPM also tends to increase. However, the relationship between the upper rotor's collective pitch and the lower rotor's RPM is complex because it is influenced by multiple factors, including how much lift the upper rotor needs to generate and how this lift affects the aerodynamic behavior of the entire coaxial rotor system.

The performance and balance of the rotor system are not just dependent on either the RPM or the collective pitch alone but on how these two parameters interact. Different combinations of RPM and collective pitch will have varying effects on the rotor system's performance, which adds complexity to predicting results.

When the upper rotor's collective pitch is set to a high angle, it increases the angle at which the blades interact with the incoming air. This, in turn, increases the lift generated by the upper rotor, but also requires more power, affecting the system's balance. As the collective pitch is increased further, even small adjustments

can cause significant changes in the aerodynamic forces. Specifically, the lower rotor must adjust its RPM to maintain balance (e.g., to cancel out the torque produced by the upper rotor).

To counterbalance the increased lift (and corresponding torque) from the upper rotor as its collective pitch increases, the lower rotor might need to spin faster. This is necessary to generate enough opposing torque to stabilize the system.



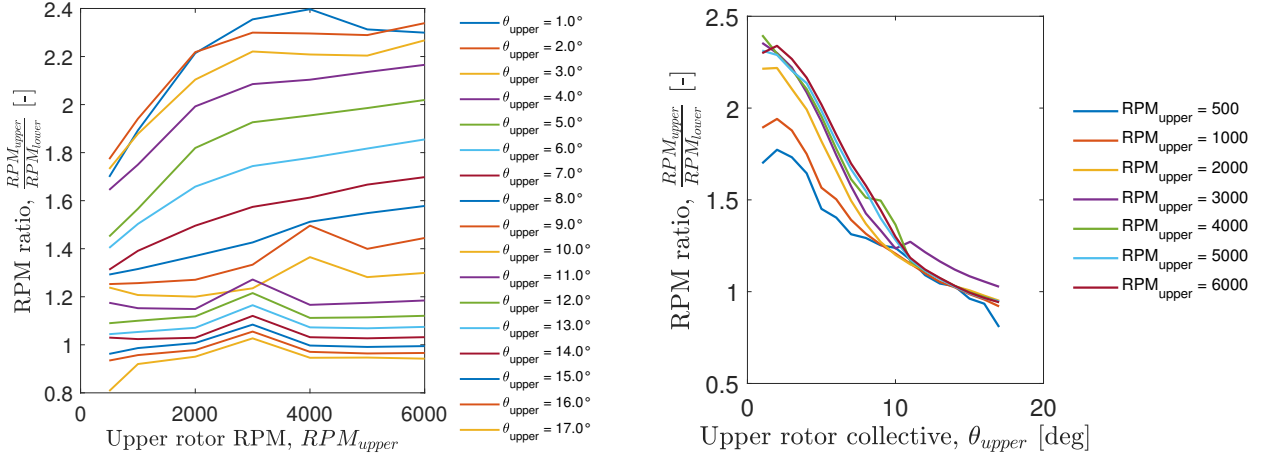
(a) Lower rotor RPM as a function of upper rotor RPM at $\theta_{upper} = 1^\circ - 17^\circ$.

(b) Lower rotor RPM as a function of upper rotor collective pitch angle at $RPM = 500 - 6000$.

Figure 4.6: Lower rotor RPM variation for the SAB 280mm blade. Blade parameters: $L = 280$ mm, $c = 25$ mm, airfoil: Selig S8035, $r_0 = 100$ mm, $r_{end} = 290$ mm.

4.5.3 Analysis of c_T/c_P and T/P Curves

The RPM ratio $\frac{RPM_{upper}}{RPM_{lower}}$ is a crucial factor for torque cancellation. The RPM ratio changes as a function of θ_{upper} (Figure 4.7b), but it remains relatively stable when plotted against RPM_{upper} (Figure 4.7a). This suggests that while the RPM ratio is sensitive to changes in the collective pitch of the upper rotor, it is more consistent across different upper rotor RPMs.

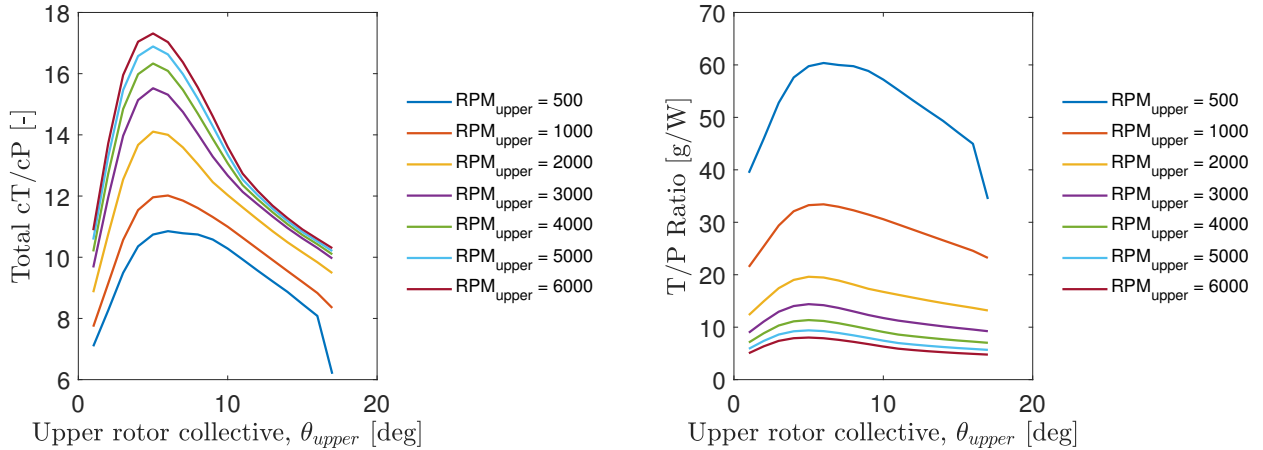


(a) RPM ratio as a function of upper rotor RPM at $[\theta_{upper} = 1^\circ - 17^\circ]$.

(b) RPM ratio as a function of upper rotor collective pitch angle at $RPM = [500 - 6000]$.

Figure 4.7: RPM ratio variation for the SAB 280mm blade. Blade parameters: $L = 280$ mm, $c = 25$ mm, airfoil: Selig S8035, $r_0 = 100$ mm, $r_{end} = 290$ mm.

This non-constant behavior of the RPM ratio as a function of θ_{upper} leads to variations in the c_T/c_P curves, resulting in several distinct curves for different upper rotor RPMs as shown in Figure 4.8a. Since the lower rotor RPM is chosen to cancel the torque, variations in the RPM ratio directly impact the thrust and power coefficients, resulting in differences in c_T/c_P .



(a) c_T/c_P as a function of upper rotor collective pitch angle at $RPM = [500 - 6000]$.

(b) Thrust-to-power ratio T/P as a function of upper rotor collective pitch angle at $[RPM = 500 - 6000]$.

Figure 4.8: Variation of c_T/c_P and T/P for the SAB 280mm blade. Blade parameters: $L = 280$ mm, $c = 25$ mm, airfoil: Selig S8035, $r_0 = 100$ mm, $r_{end} = 290$ mm.

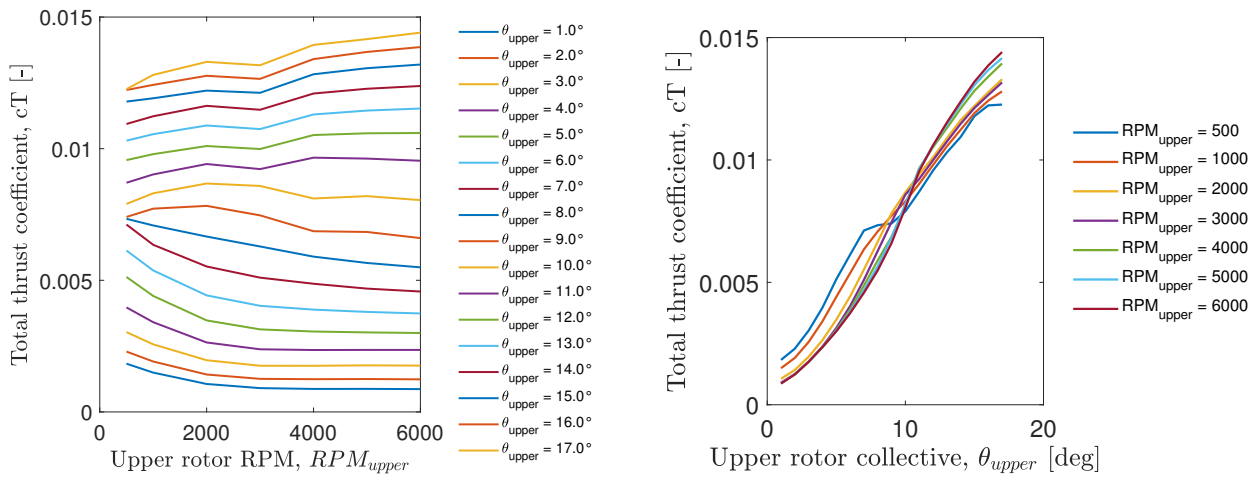
The behavior of the c_T/c_P and T/P curves can be understood by analyzing the physical relationship between thrust, power, and rotor speed. The thrust (T) is proportional to the square of the rotational speed (ω), implying that as RPM increases, thrust increases, but not as rapidly as power consumption. On the other hand, the power (P) is proportional to the cube of the rotational speed (ω), meaning that the power required increases faster than the thrust as RPM increases.

The c_T/c_P ratio represents the efficiency of thrust production relative to power consumption. Since c_T

(thrust coefficient) increases with RPM, the c_T/c_P ratio will also increase initially. However, as RPM increases further, c_P (power coefficient) increases more rapidly due to the cubic relationship with ω , causing the c_T/c_P ratio to peak at a certain RPM and then decrease as power consumption surpasses thrust production.

The T/P ratio is directly proportional to the c_T/c_P ratio divided by the RPM (ω) (See relations presented in section 4.3.2). Therefore, while c_T/c_P increases with RPM, the rapid increase in power consumption at higher RPMs causes the T/P ratio to peak at lower RPMs. At higher RPMs, the system becomes less efficient because the power needed for the same thrust level becomes disproportionately large. Hence, the T/P ratio decreases at higher RPMs, and therefore an optimal solution is found at $(c_T/c_P)_{max}$.

Figures 4.9a and 4.10a representing c_T versus RPM and c_P versus RPM show distinct trends in thrust and power coefficients as the upper rotor RPM increases. The c_T plots indicate that the total thrust coefficient does not increase uniformly with RPM; instead, it exhibits a more complex behavior, especially at higher collective angles. Specifically, at lower collective angles (θ_{upper}), the increase in c_T with RPM is more gradual, while at higher collective angles, c_T increases more significantly as RPM rises.



(a) Total thrust coefficient c_T as a function of upper rotor RPM at $[\theta_{upper} = 1^\circ - 17^\circ]$.

(b) Total thrust coefficient c_T as a function of upper rotor collective pitch angle at $[RPM = 500 - 6000]$.

Figure 4.9: Total thrust coefficient c_T variation for the SAB 280mm blade. Blade parameters: $L = 280$ mm, $c = 25$ mm, airfoil: Selig S8035, $r_0 = 100$ mm, $r_{end} = 290$ mm.

In contrast, the c_P plots reveal that the power coefficient initially decreases as RPM increases, reaching a minimum at mid-range RPMs before starting to rise again, particularly at higher collectives. This trend reflects the balance between aerodynamic efficiency and power requirements: at lower RPMs, power consumption is higher due to less efficient aerodynamic conditions, while at higher RPMs, although aerodynamic efficiency improves, the power required to maintain the increased thrust becomes significantly greater.

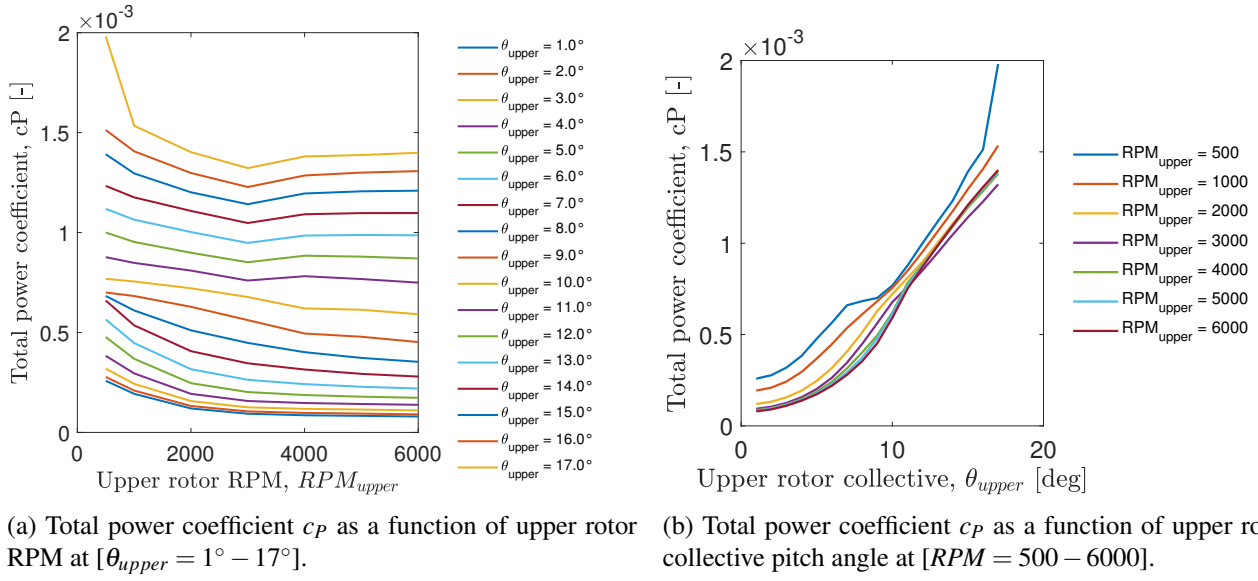


Figure 4.10: Total power coefficient c_P variation for the SAB 280mm blade. Blade parameters: $L = 280$ mm, $c = 25$ mm, airfoil: Selig S8035, $r_0 = 100$ mm, $r_{end} = 290$ mm.

These observations are consistent with the earlier analysis of the c_T/c_P and T/P curves. Indeed, the relationship between c_T and c_P as functions of RPM explains why c_T/c_P peaks at higher RPMs while T/P peaks at lower RPMs. At higher RPMs, the system can produce more thrust, but the associated increase in power consumption leads to a decrease in efficiency, as reflected in the T/P ratio. Conversely, at lower RPMs, power consumption is more balanced relative to thrust, leading to a peak in the T/P ratio.

Finally, the peak of c_T/c_P at higher RPMs suggests that the rotor is capable of producing more thrust efficiently at these speeds, but it comes at the cost of increased power, which diminishes the T/P efficiency. In contrast, the T/P ratio's peak at lower RPMs demonstrates that while the thrust may be lower, the power required is much less, making it a more efficient operating point for the system in terms of energy use.

4.5.4 Thrust and Power Distribution

Generally, the thrust generation and power consumption of the entire coaxial rotor system exhibit similar tendencies: both increase with the upper rotor collective pitch and the upper rotor RPM. This trend is illustrated in Figures 4.11a and 4.11b. This finding is logical, as a higher collective pitch on the upper rotor generates more thrust, but it also leads to increased power consumption. The increased thrust results in higher torque, which necessitates a faster rotation of the lower rotor to counteract this torque. Consequently, the power consumption of the lower rotor increases, thereby raising the overall power consumption of the system.

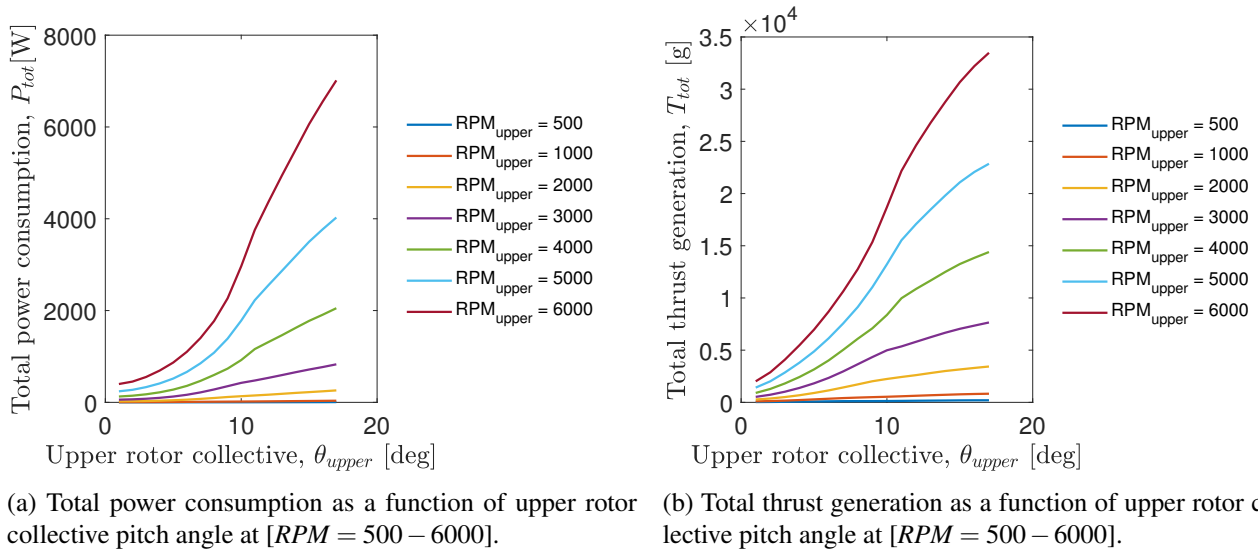


Figure 4.11: Variation of total thrust generation and total power consumption for the SAB 280mm blade. Blade parameters: $L = 280$ mm, $c = 25$ mm, airfoil: Selig S8035, $r_0 = 100$ mm, $r_{end} = 290$ mm.

Moreover, the plots of power consumption and thrust generation illustrating the contribution of each rotor separately (see Figure 4.12) reveal interesting behaviors across different upper rotor collectives and RPMs.

At lower collective angles (θ_{upper}), the thrust generation is more significant on the lower rotor. This occurs because, at low collective angles, the upper rotor is not fully utilizing its capacity to generate thrust, leading to a situation where the lower rotor must compensate by producing more thrust to maintain the overall lift and balance of the system. The lower rotor is thus operating more efficiently in these conditions, contributing more to the total thrust generation.

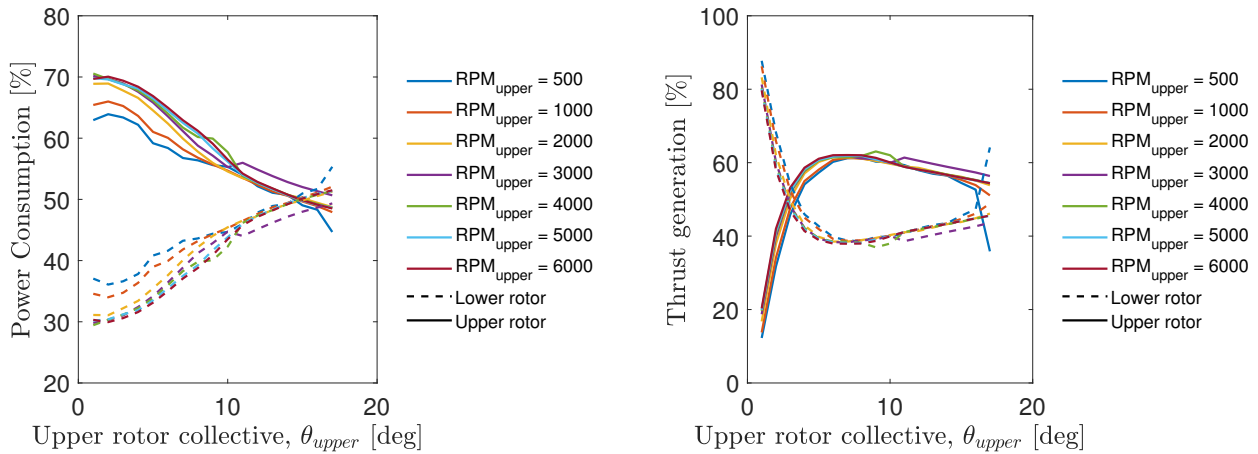
Conversely, the power consumption at these lower collective angles does not vary as significantly between the upper and lower rotors. This is because power consumption is more directly tied to the RPMs, which remain relatively stable across the system, rather than to the collective pitch alone. Therefore, while the thrust generation shifts between rotors, the total power consumed by the system is more uniformly distributed, reflecting the shared load between the two rotors in terms of maintaining rotational speed and overcoming drag.

As the collective pitch increases, particularly at high collective angles and high RPMs, a noticeable divergence occurs between the thrust and power generation of the upper and lower rotors. At these settings, the upper rotor begins to dominate both in terms of thrust production and power consumption. The physical reasoning behind this is that the increased collective angle significantly boosts the angle of attack on the upper rotor blades, enhancing their lift generation but also greatly increasing the aerodynamic drag and induced losses. This leads to a higher rate of power consumption by the upper rotor, which grows disproportionately compared to the thrust it generates. The lower rotor, meanwhile, becomes less efficient due to increased interference and reduced aerodynamic efficiency in the wake of the upper rotor, causing a divergence in the thrust-to-power relationship.

Additionally, The analysis of thrust and power distribution reveals that, except for extreme cases (small angles of attack and high collective pitch at high RPM), the thrust distribution between the upper and lower rotors generally varies between 40% and 60%. Specifically, the upper rotor typically generates between 50%

and 60% of the total thrust, while the lower rotor contributes between 40% and 50%. These percentages align with findings in the literature, which suggest that coaxial rotor systems often exhibit a nearly equal proportion of thrust generation between the upper and lower rotors [38]. Moreover, As the collective pitch of the upper rotor increases, the rotor blades generate more lift for a given RPM. This means that for the same thrust, the rotor does not need to work as hard in terms of RPM, which results in a decrease in power consumption. In essence, the rotor becomes more aerodynamically efficient as the blades are better aligned to produce lift with less induced drag. This efficiency is reflected in the decrease in power consumption as the collective pitch increases, even as the rotor continues to generate the necessary thrust. In contrast, the power consumption of the lower rotor increases with the collective pitch of the upper rotor. This is because as the upper rotor generates more thrust and consumes less power, the lower rotor, operating in the disturbed wake of the upper rotor, has to work harder to generate the remaining thrust required to balance the system. The lower rotor, which is less aerodynamically efficient due to the interaction with the wake of the upper rotor, compensates for the increased load by increasing its RPM, leading to higher power consumption.

These observations highlight the complexity of optimizing coaxial rotor systems, where the interplay between collective pitch, RPM, and rotor interactions can lead to non-intuitive outcomes in terms of performance and efficiency.



(a) Power consumption as a function of upper rotor collective pitch angle at $[RPM = 500 - 6000]$.

(b) Thrust generation as a function of upper rotor collective pitch angle at $[RPM = 500 - 6000]$.

Figure 4.12: Thrust generation and power consumption for the SAB 280mm blade. Blade parameters: $L = 280$ mm, $c = 25$ mm, airfoil: Selig S8035, $r_0 = 100$ mm, $r_{end} = 290$ mm.

4.5.5 T/P vs. Thrust

The T/P vs. Thrust plots (see Figures 4.13a and 4.13b) offer crucial insights into the relationship between thrust generation and power efficiency across different rotor configurations. These plots reveal how the system's power efficiency varies with the amount of thrust being generated.

At lower thrust levels, the T/P ratio is higher, indicating greater efficiency. This is because, at these lower thrust levels, the rotors are operating within their most efficient aerodynamic range, where the induced and profile losses are minimized. The power consumption is relatively low compared to the thrust generated, leading to a higher T/P ratio.

As thrust increases, particularly beyond a certain point, the T/P ratio begins to decrease. This reduction is due to the fact that higher thrust requires higher collective pitches and RPMs, which lead to a disproportionate increase in power consumption. At higher collectives, the rotors experience more significant induced drag and other aerodynamic losses, which increase the power required to maintain the same level of thrust. Additionally, the increased angle of attack at higher collectives can lead to flow separation and stall on parts of the blades, further reducing aerodynamic efficiency and thus requiring even more power to generate the same thrust.

The deviation observed at higher thrust levels, especially at high collective and high RPM, reflects this shift from a regime of efficient thrust generation to one where aerodynamic losses dominate, causing the T/P ratio to drop. This deviation indicates that the rotor system becomes increasingly less power-efficient as it is pushed toward its operational limits, which is a critical consideration for optimizing performance in high-demand scenarios.

One can also notice that the T/P reaches its peak for all RPMs at the same upper collective value of 5° at which the aerodynamic efficiency of the rotor is at its maximum.

Finally, the T/P vs. Thrust plot allows for the determination of the optimal configuration for a specific thrust requirement. For the SAB280 blade on order to achieve $T = 6$ kg, the optimal configuration was identified at $\text{RPM}_{\text{upper}} = 3000$ (Purple curve) with $\theta_{\text{upper}} = 13^\circ$. This corresponds to a lower rotor configuration of approximately $\theta_{\text{lower}} = 18.5^\circ$ and $\text{RPM}_{\text{lower}} = 2600$ (See Table B.1) and this optimal configuration delivers a T/P of approximately 11 g/W which is below the target value that is equal to 12.5 g/W.

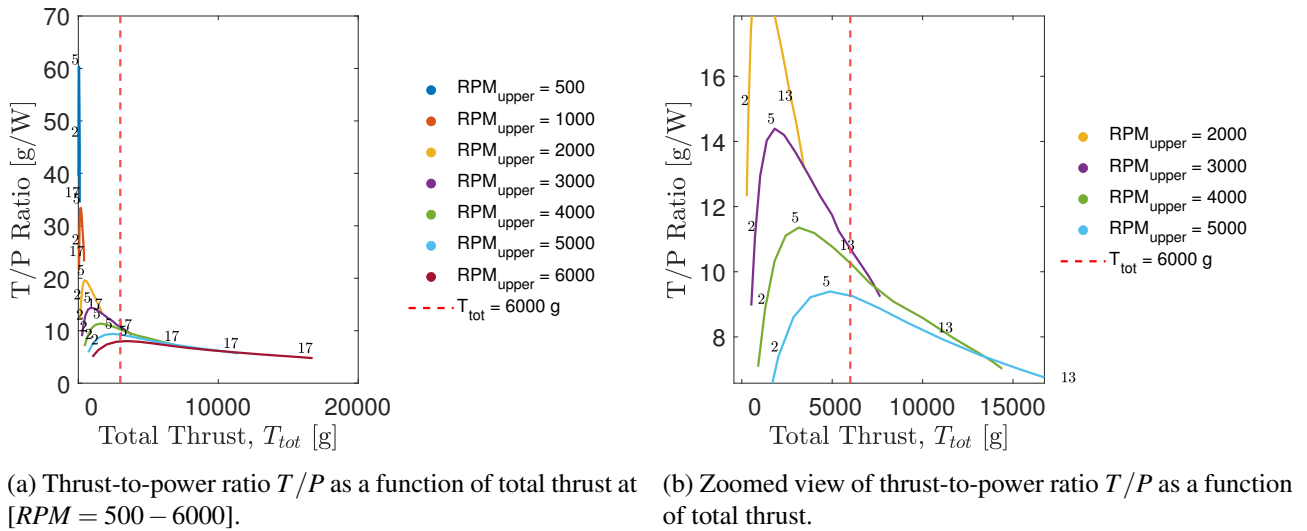


Figure 4.13: Thrust-to-power ratio T/P for the SAB 280mm blade at $\theta_{\text{upper}} = 1^\circ - 17^\circ$. Blade parameters: $L = 280$ mm, $c = 25$ mm, airfoil: Selig S8035, $r_0 = 100$ mm, $r_{\text{end}} = 290$ mm.

4.6 Conclusion

The optimization results presented in this chapter focused on the SAB280mm blade, providing detailed insights into the variation of rotor parameters and their impact on performance. The results demonstrated how different

configurations of the upper rotor collective pitch and RPM influence the corresponding optimal settings for the lower rotor to achieve torque cancellation and maximize efficiency.

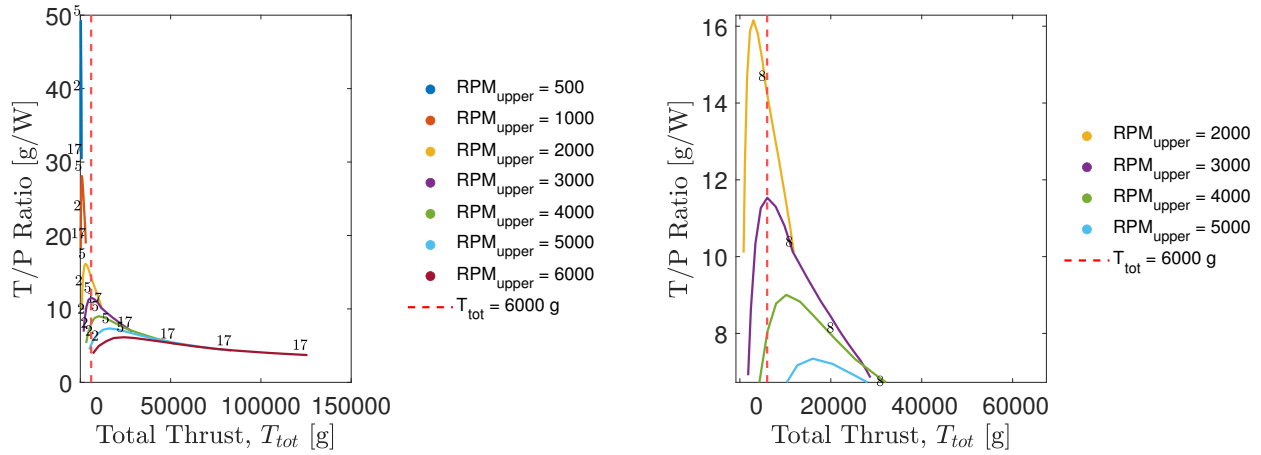
Among the blades studied, the ALZRC80 blade turned out to be the most performant for achieving a thrust of $T = 6$ kg. The ALZRC380 blade achieves the target thrust of 6 kg with a higher T/P ratio compared to the SAB280mm and the other blades (See Appendix B). Specifically, at $T = 6$ kg, the ALZRC380 achieves a T/P ratio of approximately 15 g/W at a lower rotational speed than the SAB280 blade equaling 2000 RPM and an upper rotor collective of $\theta_{upper} = 8^\circ$, this turns out to be even more optimal than the target value of 12.5 g/W, whereas the SAB280mm achieves a T/P ratio of around 11 g/W, as illustrated in Figures 4.15, 4.14a, 4.14b and 4.13b .

The superior performance of the ALZRC380 can be attributed to several factors. Firstly, its slightly larger chord length compared to the SAB280mm blade, which enhances its ability to generate lift efficiently. Indeed, a wider blade can interact with a larger volume of air, effectively generating more lift. This can lead to a higher thrust-to-power ratio, as the blade can achieve the required thrust with potentially lower RPMs or less aggressive collective pitch settings, thereby reducing the power required for the same thrust output.

Secondly, it can also be attributed to the increased overall blade length which plays a significant role in its performance. A longer blade span increases the rotor disk area, which enhances the blade's ability to generate lift. Additionally, a longer blade span typically leads to higher tip speeds, which can improve the blade's aerodynamic efficiency, especially in hover conditions. This also contributes to a more favorable lift-to-drag ratio, as the blade can generate more lift with relatively lower induced drag compared to shorter blades. Finally, the ALZRC80's overall geometry, including its airfoil profile and span, contributes to better aerodynamic characteristics, particularly in terms of reducing induced drag and improving the lift-to-drag ratio. These factors collectively result in a more favorable c_T/c_P ratio, enabling the ALZRC380 to achieve higher efficiency at the target thrust level.

The results show the importance of blade geometry in optimizing rotor performance, and the detailed analysis presented here provides a solid foundation for further refinements and studies in coaxial rotor system design. The results for the other blades, which are presented in Appendix B, generally exhibit similar tendencies and behaviors, although the ALZRC380 stands out as the most efficient in terms of the T/P ratio for the specified thrust target.

It is important to note that the T/P ratio delivered by different blades can vary depending on the upper rotor RPM. For instance, at a rotational speed of 3000 RPM, the ALZRC 325mm blade achieves the highest T/P ratio of 12.5 g/W for a $T = 6$ kg (See appendix B). However, this is still lower than the T/P ratio of 15 g/W achieved by the ALZRC380 blade at 2000 RPM. Therefore, it is crucial to analyze the behavior of different blades across the RPM range and identify the configuration that provides the highest T/P ratio for a desired thrust.



(a) Thrust-to-power ratio T/P as a function of total thrust at $[RPM = 500 - 6000]$. (b) Zoomed view of thrust-to-power ratio T/P as a function of total thrust.

Figure 4.14: Thrust-to-power ratio T/P variation for the ALZRC380 blade. Blade parameters: $L = 380 \text{ mm}$, $c = 33.5 \text{ mm}$, airfoil: St. CYR 172 (Royer), $r_0 = 100 \text{ mm}$, $r_{end} = 480 \text{ mm}$.

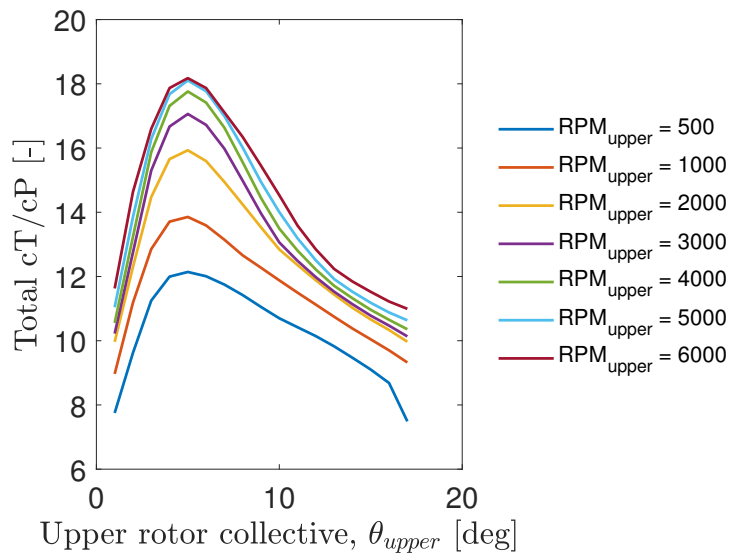


Figure 4.15: cT/cP as a function of upper rotor collective pitch angle for the ALZRC380 blade at $[RPM = 500 - 6000]$. Blade parameters: $L = 380 \text{ mm}$, $c = 33.5 \text{ mm}$, airfoil: St. CYR 172 (Royer), $r_0 = 100 \text{ mm}$, $r_{end} = 480 \text{ mm}$.

Chapter 5

Geometry optimization

5.1 Introduction

The main focus of this chapter is to change the design strategy of the rotor blade to enhance its aerodynamic performance. Unlike the previous chapter, where the optimization was centered on finding the optimal operating conditions, the focus here will be on optimizing the blade's geometry. Specifically, modifications to the blade's twist and chord distribution, key factors influencing rotor performance, will be explored.

The advantage lies in the fact that ROTARE has been implemented with the capability to introduce variations in blade geometry, such as twist and chord distribution, and to accurately compute the resulting performance.

Firstly, the optimization of the twist distribution of the SAB280 blade will be conducted. Using ROTARE and an iterative process, the optimal twist distribution that maximizes aerodynamic efficiency will be determined. Once this optimal twist distribution has been identified, it will be implemented in the blade configuration, and the performance will be recalculated in ROTARE to assess the improvements.

Next, the influence of modifying the chord distribution will be investigated. The approach will be similar to that used for twist optimization. Since ROTARE is also capable of handling both constant and variable chord distributions, the potential for further performance enhancements through altering the chord distribution will be explored.

It is important to note that in this research, combining twist and chord variations is not considered, as it would introduce significant complexity in terms of coding and results. Therefore, the twist and chord variations will be explored separately.

These geometry modifications will be applied to the optimal configuration of the SAB280 blade, which was found in the previous chapter to provide the required thrust of $T = 6$ kg. This optimal configuration was identified with an upper rotor RPM of 3000 and a collective pitch angle (θ) of 13° , while the lower rotor operated at an RPM of 2575.4 with a collective pitch angle of 18.43° . The analysis will determine whether these geometry changes lead to further improvements in performance and provide insights into whether the modifications significantly enhance the rotor's performance or if the improvements are marginal.

It should be noted that the blade configuration setup remains the same as the one explained in the previous chapter in section 4.2, and the coefficients are also non-dimensionalized as before. Furthermore, all the methodologies explained in Chapter 4, including torque cancellation, remain consistent in this chapter. The only changes introduced here are the modifications to the twist and chord distribution of the blade, with the subsequent performance recalculated based on these changes.

5.2 Strategy

5.2.1 Introduction of twist in the blade airfoil

When considering the exploitation of efficient thrust generation at the tip of a blade, the twist distribution plays a crucial role in optimizing aerodynamic performance. The twisting of the blade root and tip has several impacts. Concerning the tip blade twist, it has an impact on tip vortex reduction, which in turn reduces the induced drag [16]. Furthermore, it has a positive impact on the lift distribution, where a proper twist can lead to a more optimal lift distribution along the blade span, improving the overall aerodynamic efficiency [29]. Finally, it also has a positive impact on stall characteristics, as twisting the tip can delay flow separation, allowing stall to occur at higher angles of attack. This is beneficial for maintaining performance at high blade loading [22]. The negative impact of twisting the blade tip could be the increased structural complexity and the potential for higher bending stresses[16].

Concerning root twisting, it also has its positive and negative impacts. Positive impacts include improved root performance, where the flow is typically more complex due to lower Reynolds numbers and three-dimensional effects [50]. Furthermore, the lift distribution could also be better by twisting the root [30]. However, a negative impact of twisting the blade root could have a lower effect on tip efficiency since thrust generation primarily occurs in the outer section of the blade (mid-span to tip). Therefore, root twist might not have as significant an impact on the thrust generated at the tip compared to tip twist [41].

Twist Optimization Strategy Implementation

As we consider the optimization of the SAB280 blade, it is important to note that the blade has the same airfoil profile along its entire span. This implies that the optimal angle of attack remains constant across the span of the blade. Therefore, to determine the optimal twist distribution for the SAB280 blade, a different approach will be employed. Instead of starting with a predefined twist, the process will begin in the opposite direction—by using the local inflow angle and incidence angle to derive an improved twist distribution. The optimization here focuses on positioning the blade profile at the optimal angle of attack relative to the incoming flow to maximize the c_L/c_D ratio.

The idea here is to start with a non-twisted blade operating at the optimal configuration, providing the required thrust of $T = 6$ kg. For this non-twisted blade, ROTARE computes its aerodynamic performance, including the distribution of the inflow angle (ϕ) along the span of both the upper and lower rotors. From this distribution, an initial twist can be calculated to improve the blade's performance by positioning it at the most favorable angle with respect to the lift-to-drag ratio (c_L/c_D), using the following formula:

$$\chi = \frac{\pi}{2} - \phi + \alpha^* \quad (5.1)$$

where

- χ is the twist angle.
- ϕ is the inflow angle.
- α^* is the optimal angle of attack of the blade airfoil and is equal to 9.75° . This angle was computed using the polars of the airfoil of the upper and lower rotors. It is indeed the same for both rotors since they consider the same airfoil. The polars are represented in Figure 5.1.

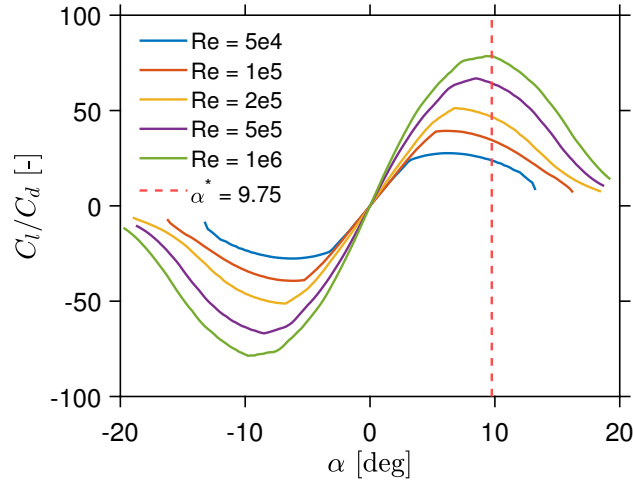


Figure 5.1: Polars of the airfoil Selig S8035 for the SAB280mm blade. Blade fixed parameters: $c = 25$ mm, blade length $L = 280$ mm, $r_0 = 100$ mm, and $r_{\text{end}} = 290$ mm.

A representation of the velocity triangle of a blade element is shown in Figure 5.2, which helps in understanding the origin of Eq.5.1.

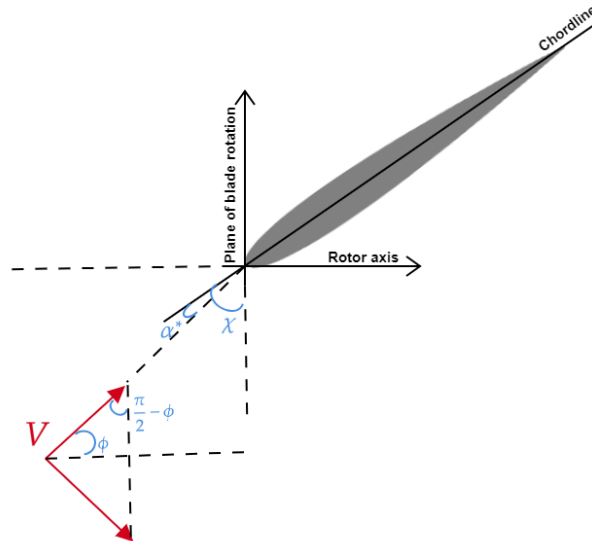


Figure 5.2: Velocity triangle of the blade element for the SAB280mm blade. Blade fixed parameters: $c = 25$ mm, blade length $L = 280$ mm, $r_0 = 100$ mm, and $r_{\text{end}} = 290$ mm.

To explain the process more clearly, the following steps are carried out:

- **Initial twist calculation:** Begin by computing four different values of the initial twist at specific points along the blade span—one at the root, two at mid-span, and one at the tip. These values are computed using Eq. 5.1 linking the inflow angle obtained from ROTARE for the non-twisted blade at the optimal configuration with the twist.
- **Cubic interpolation:** Apply a cubic interpolation to these four points to obtain an initial twist distribution along the entire blade span. This distribution positions the blade at the best possible angle relative to c_L/c_D , using the optimal α^* derived from the blade's airfoil polar data.
- **Performance recalculation:** With the initial twist distribution determined, the blade's performance is recomputed using ROTARE, keeping all other parameters the same as before but introducing the newly calculated twist distribution.
- **Iterative twist adjustment:** After the performance is recalculated, the inflow angle distribution is updated using the new performance data from ROTARE. This new inflow angle distribution is then used to compute a new twist distribution, following the same steps as before. Essentially, at each iteration, the blade is aligned with the velocity triangles of the previous configuration, adjusting the twist to the most favorable angle.
- **Convergence:** This iterative process continues until the twist angles no longer change significantly, indicating that convergence has been reached. At this point, the blade is considered to have an optimal twist distribution for the given operating conditions, aligning the blade correctly with the inflow angles for maximum aerodynamic efficiency.

By systematically aligning the blades with the velocity triangles and adjusting the twist distribution iteratively, the optimal twist for the SAB280 blade is achieved, ensuring that the blade operates at peak efficiency throughout its span.

Finally, a flow chart of the optimization process is presented in figure 5.3 to summarize and provide a better understanding of the process.

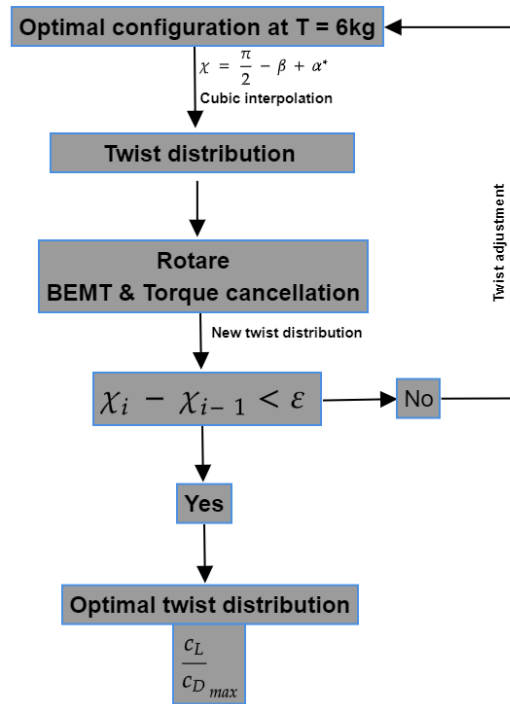


Figure 5.3: Flow chart of the twist optimization process.

5.2.2 Results

The twist distribution shown in Figure 5.4 highlights how the twist angle varies along the span of both the upper and lower rotors. The upper rotor exhibits a moderate decrease in twist from approximately 16° at the root to 14° at the tip, ensuring that the angle of attack remains consistent across the span, which is crucial for efficient lift generation. In contrast, the lower rotor shows a more pronounced decrease in twist from 25° to 15° , a necessary adjustment to cope with the disturbed flow field generated by the upper rotor. This significant twist helps the lower rotor maintain an optimal angle of attack, which is essential for generating thrust efficiently in the complex aerodynamic environment of a coaxial rotor system.

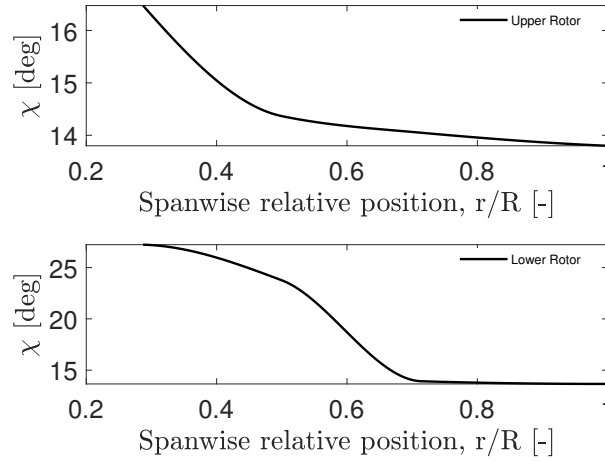


Figure 5.4: Twist distribution for the SAB280mm blade at $RPM_{upper} = 3000$, $\theta_{upper} = 13^\circ$, $RPM_{lower} = 2600$ and $\theta_{lower} = 18.5^\circ$. Blade fixed parameters: $c = 25$ mm, blade length $L = 280$ mm, $r_0 = 100$ mm, and $r_{end} = 290$ mm, featuring a Selig S8035 airfoil.

To further understand the physical effects of this twist distribution, the local distributions of thrust, drag, and power analyzed in this study correspond to the values distributed over the surface area swept by each segment of the blade. Specifically, these distributions are evaluated per unit span along the blade, reflecting the contributions of each blade segment to the overall aerodynamic performance. This analysis provides insights into how the aerodynamic forces vary along the length of the blade, allowing for a detailed understanding of the efficiency and effectiveness of the blade's design.

These behaviors were specifically analyzed at the optimal configuration of 3000 RPM and $\theta_{upper} = 13^\circ$ for the upper rotor, and approximately 18.5° and 2600 RPM for the lower rotor in the untwisted case. For the twisted case, while the upper rotor's configuration remains the same, the lower rotor's optimal configuration changes to $\theta_{lower} = 16.4^\circ$ and 2500 RPM. These optimal configurations are the ones necessary to achieve the desired thrust of 6kg.

Figure 5.5 presents the local thrust-to-power ratio (dT/dP) as a function of the spanwise position for both the upper and lower rotors, comparing twisted and untwisted blade configurations.

For the upper rotor (upper plot), the untwisted blade exhibits a higher dT/dP ratio near the root, which gradually decreases towards the tip. This behavior can be attributed to the untwisted blade maintaining a higher angle of attack near the root, resulting in greater thrust generation relative to power consumption in this region. However, towards the tip, the flow velocities increase, and the twisted blade's optimized angle of attack becomes more effective, reducing the difference in dT/dP between the two configurations.

For the lower rotor (lower plot), the same behavior occurs due to the same reasons where at the root, the twisted blade has a slightly lower dT/dP ratio with respect to the untwisted blade that increases further towards the tip. Moreover, the jump in dT/dP that the lower rotor has, corresponds to the wake limits of the upper rotor.

In summary, the untwisted blades perform slightly better near the root where flow conditions are simpler, while the twisted blades are more effective towards the tip, where they can better manage the complex aerodynamic forces, resulting in improved efficiency.

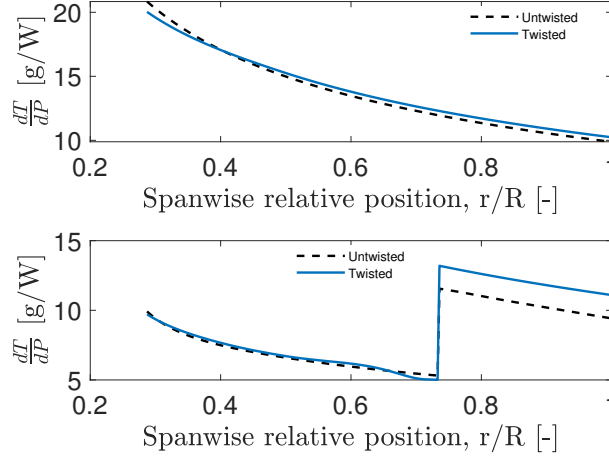
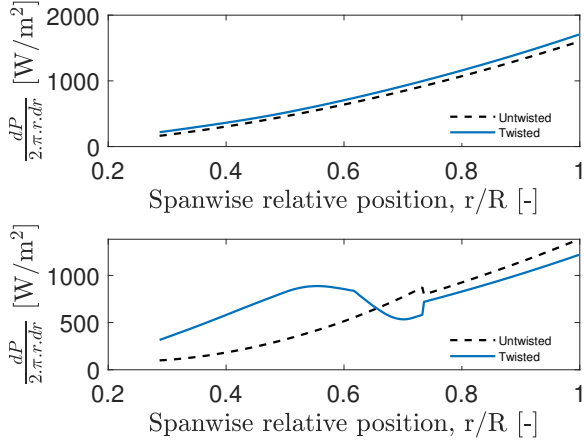
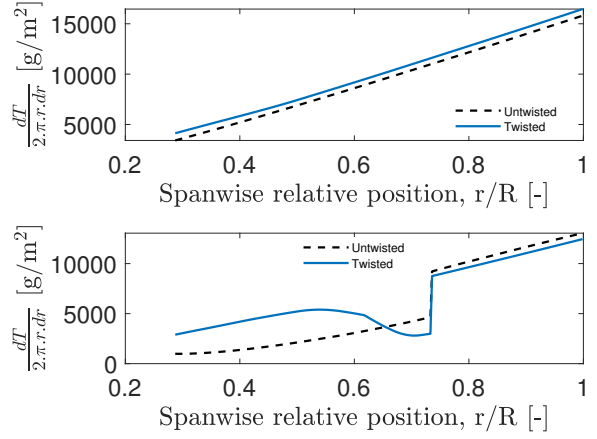


Figure 5.5: Local dT/dP vs. span for the SAB280mm blade at $RPM_{upper} = 3000$, $\theta_{upper} = 13^\circ$, $RPM_{lower} = 2600$ & $\theta_{lower} = 18.5^\circ$ (Non-twisted), $RPM_{lower} = 2500$ & $\theta_{lower} = 16.4^\circ$ (Twisted). Blade fixed parameters: $c = 25$ mm, blade length $L = 280$ mm, $r_0 = 100$ mm, and $r_{end} = 290$ mm, featuring a Selig S8035 airfoil.

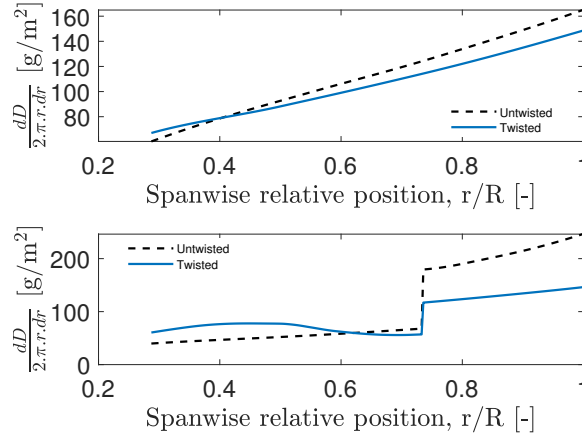
This behavior near the hub of the untwisted blade can also be explained by examining the local distributions of thrust ($dT/2\pi r dr$) and drag ($dD/2\pi r dr$) as represented in Figures 5.6b, 5.6c. The twisted blades concentrate thrust generation near the root and tip, which, while reducing drag, leads to an undesirable increase in mechanical losses near the hub. This concentration of thrust near the hub is inefficient because the generated thrust contributes less effectively to overall system performance due to the higher mechanical losses associated with thrust generation at lower radii. Additionally, the drag distribution reveals a significant reduction in drag near the tips for the twisted configuration, aligning with the goal of reducing aerodynamic losses. However, the less significant drag reduction near the hub is surprising as it has to be the opposite and this highlights the need for further optimization strategies to balance thrust and drag efficiently across the span.



(a) Variation of the local power consumption with blade span.



(b) Variation of the local thrust generation with blade span.



(c) Variation of the local drag with blade span.

Figure 5.6: Local thrust, power, and drag vs. span for the SAB280mm blade at $RPM_{upper} = 3000$, $\theta_{upper} = 13^\circ$, $RPM_{lower} = 2600$ & $\theta_{lower} = 18.5^\circ$ (Non-twisted), $RPM_{lower} = 2500$ & $\theta_{lower} = 16.4^\circ$ (Twisted). Blade fixed parameters: $c = 25$ mm, blade length $L = 280$ mm, $r_0 = 100$ mm, and $r_{end} = 290$ mm, featuring a Selig S8035 airfoil.

The local aerodynamic performance, represented in Figure 5.7, demonstrates that the twist optimization indeed improves the lift-to-drag ratio (c_l/c_d), particularly towards the blade tips. The twisted blades maintain a more consistent and optimal angle of attack, as shown in the alpha plots (α), leading to enhanced aerodynamic efficiency. However, the increased thrust generation near the hub for the twisted configuration, while beneficial for maintaining torque balance, results in a lower dT/dP near the hub, where the lift-to-drag ratio is not optimized as effectively as in the outer regions of the blade.

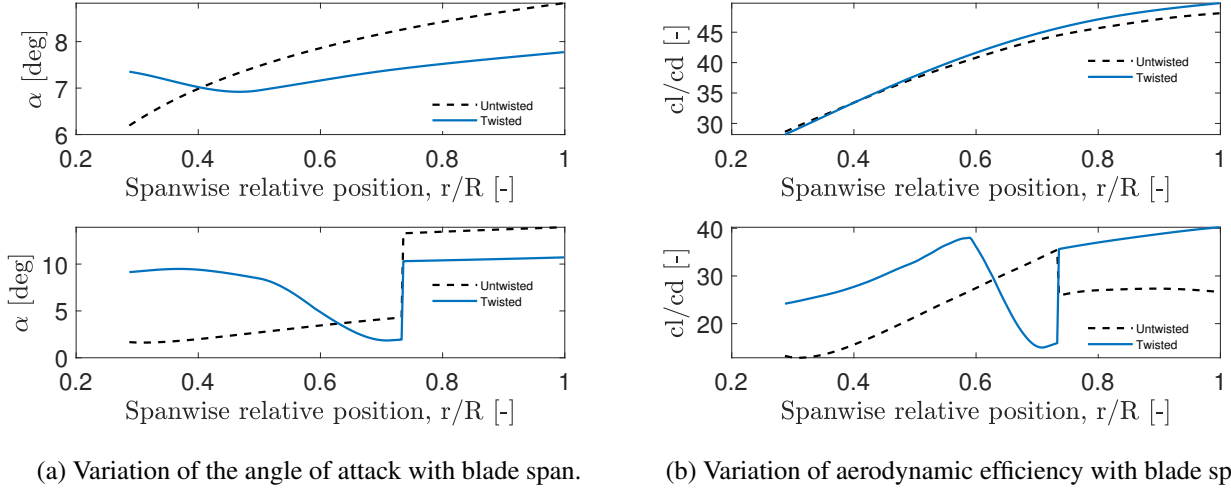


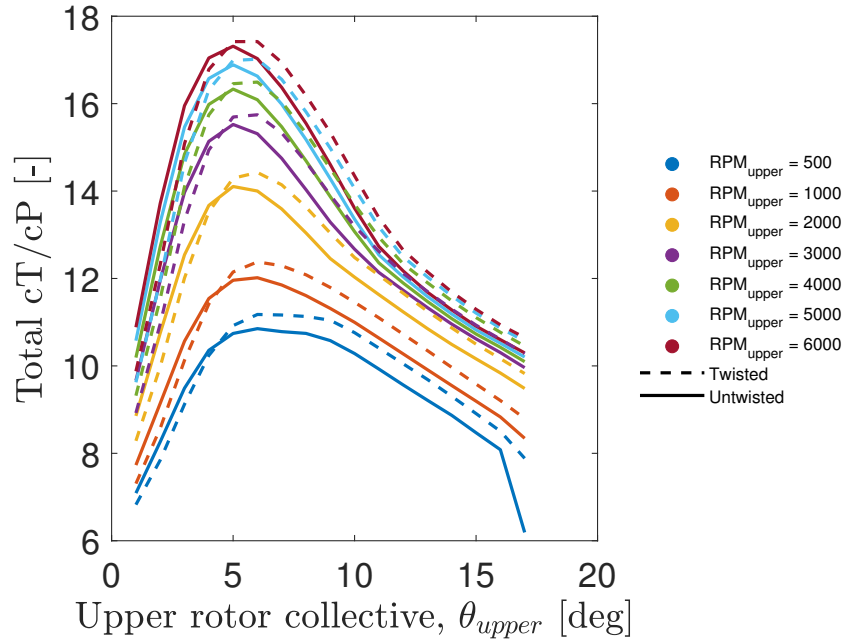
Figure 5.7: Local aerodynamics for the SAB280mm blade at $RPM_{upper} = 3000$, $\theta_{upper} = 13^\circ$, $RPM_{lower} = 2600$ & $\theta_{lower} = 18.5^\circ$ (Non-twisted), $RPM_{lower} = 2500$ & $\theta_{lower} = 16.4^\circ$ (Twisted). Blade fixed parameters: $c = 25$ mm, blade length $L = 280$ mm, $r_0 = 100$ mm, and $r_{end} = 290$ mm, featuring a Selig S8035 airfoil.

Finally, the global performance metrics, as illustrated in Figure 5.8 and Figure 5.9, show the overall impact of the twist optimization on the rotor system. The c_T/c_P curves reveal that twisting only the blades improves the efficiency of thrust generation relative to power consumption across most collective pitch settings by 4%, which is not significant. All blades studied revealed the same range of improvement varying between 3% and 4% (See Appendix B).

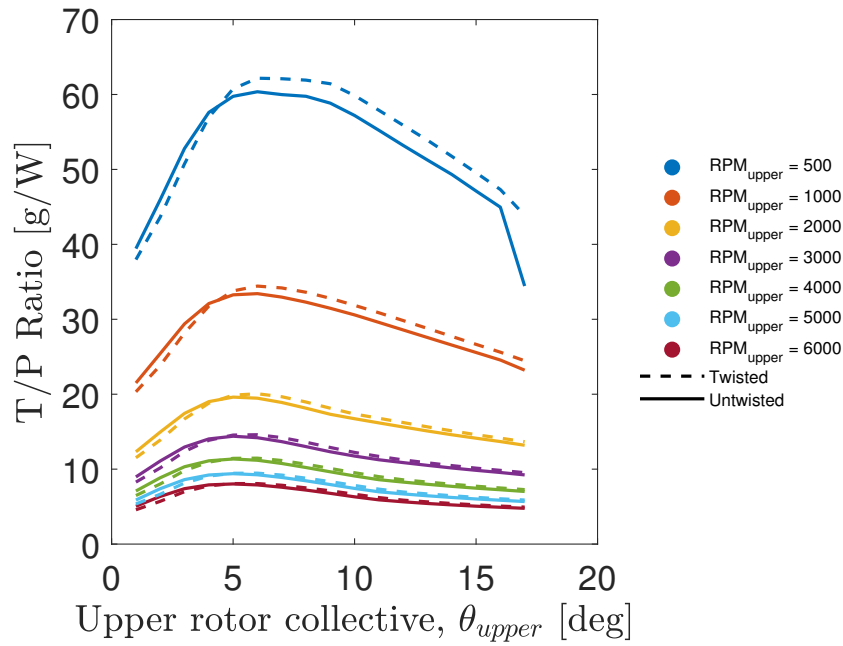
The T/P curves indicate that while the twisted blades are more efficient at lower thrust levels, the untwisted configuration becomes more competitive at higher thrust levels. This suggests that the increase in thrust near the hub in the twisted configuration leads to greater mechanical losses and inefficiencies at higher thrust settings, indicating that it may not be worthwhile to only twist the blades without combining this strategy with chord optimization since the improvements are not significant.

In conclusion, while the twist optimization strategy is effective in reducing drag and improving the lift-to-drag ratio, it also results in suboptimal thrust distribution near the hub, leading to increased mechanical losses. This indicates that twist optimization alone may not be sufficient for achieving the best performance in a coaxial rotor system. A combined strategy that optimizes both twist and chord distribution would be more effective, reducing unnecessary thrust near the hub and improving overall aerodynamic efficiency.

This concept is supported by design principles seen in wind turbine blade propellers. In this application, the chord distribution is not constant but rather varies along the span of the blade. Specifically, the chord is typically thicker at mid-span and thinner near the root and tip. This design helps to concentrate useful thrust generation in regions where it is most effective while minimizing the generation of lift that contributes to mechanical losses rather than useful thrust. For instance, in wind turbines, the chord decreases towards the root and tip, with a maximum chord located between 15% and 20% of the span. This approach minimizes energy loss at the hub and tip regions, where aerodynamic inefficiencies are most pronounced [16].

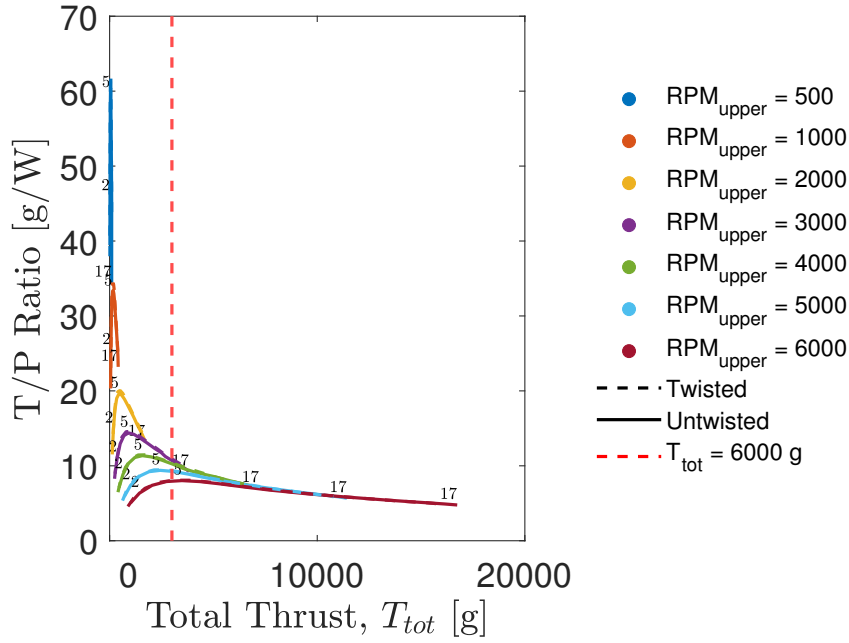


(a) c_T/c_P variation as a function of the upper collective pitch angle at $RPM = 500 - 6000$.

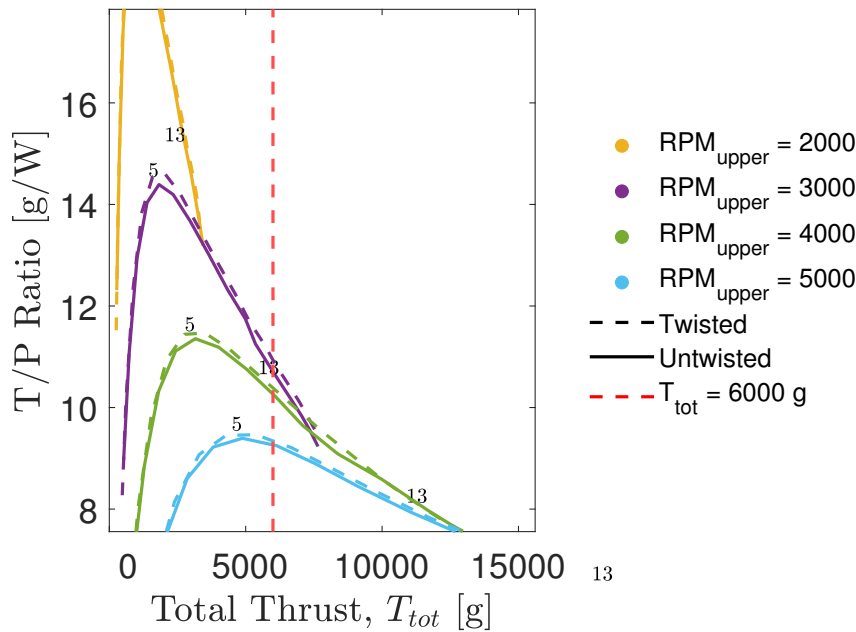


(b) Variation of the thrust-to-power ratio as a function of the upper collective pitch angle at $RPM = 500 - 6000$.

Figure 5.8: Performance improvement with twist for the SAB280mm blade. Blade fixed parameters: $c = 25$ mm, $L = 280$ mm, $r_0 = 100$ mm, and $r_{end} = 290$ mm, featuring a Selig S8035 airfoil.



(a) Thrust-to-power ratio T/P as a function of total thrust at $RPM = [500 - 6000]$.



(b) Zoomed view of thrust-to-power ratio.

Figure 5.9: Performance improvement with twist for the SAB280mm blade. Blade fixed parameters: $c = 25$ mm, blade length $L = 280$ mm, $r_0 = 10$ cm, and $r_{end} = 290$ mm, featuring a Selig S8035 airfoil. The numbers 1 to 17 on the curves correspond to the collective pitch angles θ_{upper} of the upper rotor.

5.2.3 Chord distribution of the blade

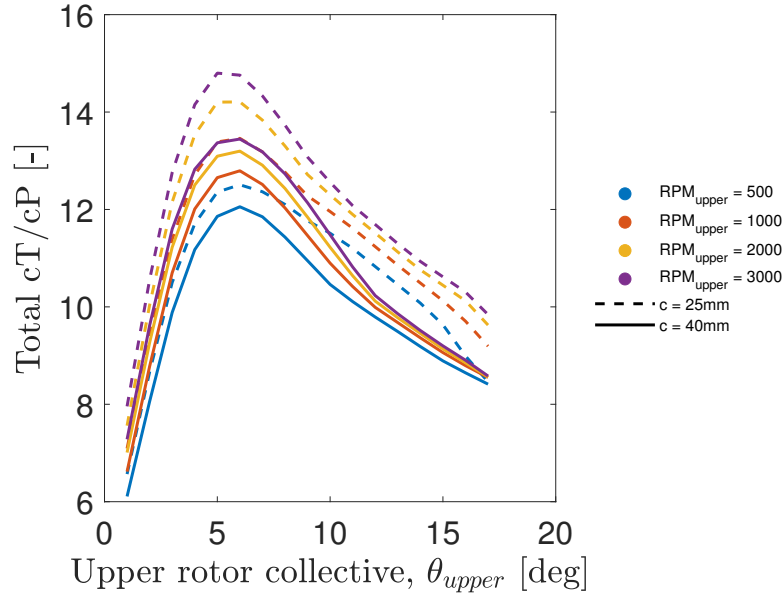
This part of the optimization is still under development and reflection, and as such, it has not been extensively detailed or supported with many plotted results. The primary objective of this section is to explain and illustrate the general tendencies of how modifying the chord distribution affects blade performance.

Initially, the optimization began with a constant chord to investigate whether increasing the chord length could lead to performance improvements. The comparison between different chord lengths is presented in Figure 5.10, where the aerodynamic performance of the SAB280mm blade with a chord length of 25mm is compared to a blade with a chord length of 40mm. These initial results show general tendencies and are not intended to provide a detailed analysis.

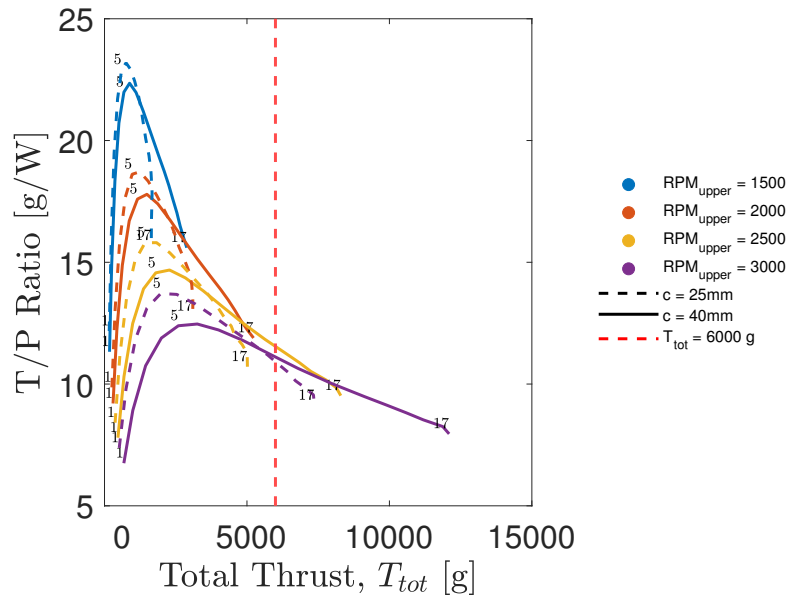
The c_T/c_P vs. θ_{upper} plot in Figure 5.10a illustrates how increasing the chord from 25mm to 40mm affects the blade's performance. As the chord length increases, the peak of the c_T/c_P curve shifts towards higher collective pitch angles, indicating that the blade with a larger chord generates more thrust at higher collective pitches. This shift is desirable when pushing the blade to operate at higher RPMs, as it allows the blade to maintain a higher angle of attack without stalling.

However, this increase in thrust generation, results in an increased aerodynamic drag, as seen in the T/P vs. T plot (Figure 5.10b). The larger chord blade, while capable of generating more thrust, becomes less efficient because the power required per unit of thrust increases. The relative losses, which include factors such as increased aerodynamic drag and higher power consumption to overcome the additional blade area, become more significant as the chord length increases.

These results highlight the importance of balancing chord length to optimize both thrust generation and efficiency. While increasing the chord enhances thrust, the associated losses reduce the overall efficiency of the blade. Typically, a performant blade is a very thin blade that turns at a very high RPM but since the RPM range is limited in our application to RPM values around 6000, an optimal chord distribution should be found.



(a) c_T/c_P variation as a function of the upper collective pitch angle at $RPM = [500 - 6000]$ for two different chord lengths.



(b) Thrust-to-power ratio variation as a function of total thrust at $RPM = 500 - 6000$ for two different chord lengths.

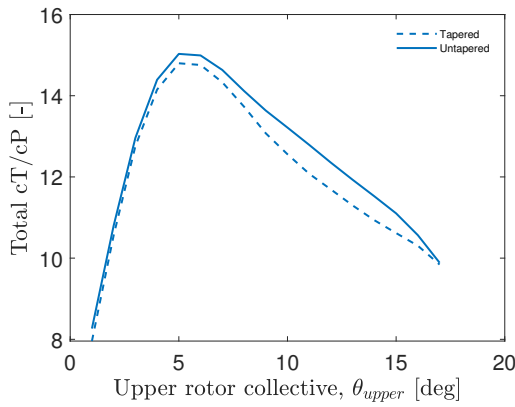
Figure 5.10: Comparison for different chord values at constant chord for the SAB280mm blade. Blade fixed parameters: $c = 25$ mm and $c = 40$ mm, blade length $L = 280$ mm, $r_0 = 100$ mm, and $r_{\text{end}} = 290$ mm, featuring a Selig S8035 airfoil.

Following this, the exploration was extended beyond simply varying the constant chord length to examine how tapering the chord—i.e., changing the chord length from the root to the tip—could potentially enhance performance. The analysis of chord tapering was conducted using random values for chord lengths at the root and tip for the sake of observing the general tendencies and clarifying the direction for future optimization efforts.

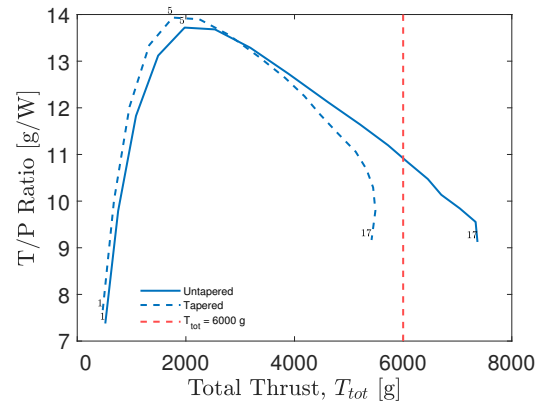
The effect of chord tapering on performance was specifically analyzed at an RPM of 3000, as shown in Fig-

ure 5.11a. This RPM was selected based on previous observations where it was noted that the rotor performs optimally around this speed, providing a balanced trade-off between thrust generation and power consumption. This speed is also within the operational range where the rotor avoids both excessive aerodynamic drag and stalling, making it a representative point for assessing the impact of chord tapering.

The results in Figure 5.11 demonstrate how tapering the chord affects the thrust-to-power ratio as a function of the upper rotor's collective pitch (θ_{upper}). The tapering tends to shift the performance curve, suggesting that adjusting the chord distribution can optimize the blade's aerodynamic efficiency by redistributing the thrust along the blade span. However, it is important to note that the chord distribution in these plots was not optimized; it was simply linearly tapered. As a result, the performance of the tapered blade does not necessarily surpass that of the untapered blade. This inefficiency makes it difficult to draw definitive conclusions from these plots, as the observed results might be not optimal compared to what could be achieved with a well-optimized chord distribution.



(a) c_T/c_P variation as a function of the upper collective pitch angle.



(b) Thrust-to-power ratio variation as a function of total thrust.

Figure 5.11: Effect of chord linear tapering on performance at $RPM = 3000$ for the SAB280mm blade. Blade fixed parameters: $c_{\text{root}} = 30$ mm, $c_{\text{tip}} = 15$ mm, $L = 280$ mm, $r_0 = 100$ mm, and $r_{\text{end}} = 290$ mm, featuring a Selig S8035 airfoil.

The plots reveal that the tapered chord distribution is less efficient than the uniform chord distribution, as it fails to generate a thrust of 6 kg even at higher collective pitch angles. Additionally, the plots show that the T/P ratio performs better near the hub, which can be attributed to the increased chord length at the root, leading to higher solidity and more effective thrust generation in this region. However, at the tip, the performance degrades and becomes less efficient due to the reduced chord length, which increases the relative losses and drag, thus highlighting the inefficiency of this particular chord distribution. This further emphasizes the complexity of optimizing chord distribution and underscores the need for a more refined approach that considers the aerodynamic principles discussed earlier.

Two important considerations must be taken into account when optimizing the chord distribution. First, on the blade and more specifically towards the root, tangential velocities increase, leading to higher losses. Second, if a significant amount of thrust is concentrated at the tip, the hydrodynamic efficiency tends to approach 1. This scenario is problematic because it means that more fluid acceleration occurs at the tip than in other sections of the blade, leading to imbalances in the mass flow and reducing overall propulsive efficiency.

To address these issues, it is generally recommended that thrust be equidistributed along the blade. Concentrating too much thrust per unit surface area at the tip results in greater acceleration of the fluid at the tip, while less acceleration occurs elsewhere on the blade. This imbalance can degrade the propulsive efficiency because the extremities (tip sections) become detrimental to the overall efficiency. Therefore, it is advisable to reduce the thrust near the root but balance it as the tip is approached.

To achieve a constant thrust distribution, the chord variation should tend toward $1/r$ as the tip is approached. This is because the mass flow that the blade accelerates increases proportionally to r , and thus the relative flow velocity increases like r . Since the thrust per unit chord increases as r^2 , to maintain a constant thrust, the chord length should decrease by a factor of $1/r$.

It may seem contradictory, but having constant thrust is not always efficient. This is because sometimes the thrust generated comes with significant losses, especially near the hub, which is why the thrust distribution should be chosen in a smart way. The goal is to achieve an optimal chord distribution that maximizes thrust generation while minimizing its relative losses. As explained previously, it is better to combine chord tapering with twisting, allowing the blade to be positioned optimally with respect to the flow. This strategy minimizes drag while generating the most efficient thrust, thanks to an optimized chord distribution.

In general, to achieve an optimal chord distribution, the strategy should involve imposing a desired thrust distribution along the blade profile. This begins with selecting how to distribute the thrust across the blade. For instance, it is known that most of the thrust is generated at the tip, and it could be decided not to generate any thrust near the hub of the upper rotor. The choice of thrust distribution is flexible, and once it is determined, the corresponding chord distribution can be computed since the chord length is proportional to the thrust generated by each blade element. Additionally, with the thrust distribution imposed and the RPM values known, the velocity triangles can also be calculated.

The ideal way to impose a thrust distribution, given the freedom to choose, involves optimizing the rotor's efficiency by proportionally allocating more thrust at the blade's extremities, where thrust generation is more effective. The interaction with the lower rotor must also be considered in this process. Several thrust distribution strategies should be compared, and their parametric impact on the lower rotor should be evaluated to guide the selection of an optimal thrust distribution.

In conclusion, the approach starts from the premise that the blade operates most effectively when positioned at the optimal incidence angle, which is constant across the entire span due to the uniform airfoil profile. Using the airfoil polars, the optimal angle of attack can be determined, and since the c_L/c_D ratio is known at this point, the optimal blade positioning can be identified.

For this design, the optimization could be simplified by selecting an operational point in hover, and then parametrizing the thrust or chord distribution along the blade. The goal is to find the best compromise between thrust and power consumption. Another possible approach involves using a constant chord and optimizing for the best T/P ratio while ensuring the blade is correctly positioned at the optimal angle of incidence, which can be automatically determined relative to the optimal angle of attack.

Chapter 6

Conclusion

The primary objective of this thesis was to explore and enhance the aerodynamic performance of coaxial rotor systems through a detailed optimization process, focusing on both operational parameters and blade geometry. The research aimed to identify optimal configurations that maximize thrust efficiency while maintaining or improving the overall aerodynamic characteristics of the system. This was achieved through a systematic approach involving both the validation of ROTARE and subsequent optimization of real rotor blades, considering real-life applications.

The first significant step in this research was the validation of ROTARE, a computational tool designed for analyzing and optimizing rotor performance. This validation was crucial to ensure that the code could reliably predict the performance of rotor blades in a single rotor configuration, which is a necessary precursor before applying it to the more complex coaxial rotor systems. Through rigorous testing and comparison with known benchmarks, ROTARE was proven to be a reliable tool for conducting further optimization analyses. This validation provided the confidence needed to proceed with the detailed optimization process of coaxial rotor systems.

Following the validation, the research proceeded with a two-phase optimization strategy. The first phase focused on operational parameter optimization, where the goal was to find the optimal configuration of the rotor system that would achieve a target thrust of $T = 6$ kg without altering the blade geometry. The optimization process involved iterative adjustments of the collective pitch angles and RPMs for both the upper and lower rotors, aiming to maximize c_T/c_P while ensuring torque cancellation between the rotors. A systematic sweep process combined with the secant method was employed to explore the design space and identify the best configuration. The optimal configuration for the SAB280 blade was determined to be an upper rotor RPM of 3000 and a collective pitch of 13° , with the lower rotor operating at approximately 2600 RPM and a collective pitch of 18.5° . Among the four blades analyzed, the ALZRC380 blade was found to be the most efficient, delivering a thrust-to-power ratio of approximately 15 g/W, which was attributed to its larger chord length, enabling better lift generation.

The second phase of the optimization focused on geometric modifications to the rotor blades, specifically examining the impact of twist and chord distribution on aerodynamic performance. The twist optimization process was carried out using an iterative approach, where the blade's twist distribution was adjusted to align with the optimal angle of attack at various points along the blade span. The objective was to improve the lift-to-drag ratio (c_L/c_D) by ensuring that each section of the blade operated at its most aerodynamically efficient angle

relative to the incoming airflow. Despite these efforts, the twist optimization alone resulted in only a modest improvement in the thrust-to-power ratio, increasing it by approximately 4%.

The study also explored the effects of varying the chord distribution, initially testing blades with constant chord lengths before moving on to tapered designs. The results indicated that while increasing the chord length could generate more thrust, it also led to increased aerodynamic drag, which diminished overall efficiency. The linearly tapered chord designs, although offering some performance improvements, did not achieve significant gains over the uniform chord configuration. This suggested that neither twist nor chord adjustments alone were sufficient to substantially enhance the rotor's performance.

A key finding of this research is that significant performance improvements in coaxial rotor systems are likely to be achieved only through the combination of twist and chord optimization strategies. The research has shown that while each geometric modification offers some benefits, their effects are not additive when applied independently. Instead, a more complete approach is required, where the blade's twist and chord are optimized together, guided by a carefully designed thrust distribution strategy. Such a strategy would ensure that the blade generates thrust efficiently across its span, with minimal drag and optimal lift-to-drag ratios at all operating points.

Moreover, this research highlights the importance of considering alternative optimization strategies. While the methods employed in this study have provided valuable insights and identified potential paths for improvement, they are not the only approaches available. Other strategies, such as more advanced computational fluid dynamics (CFD) simulations or machine learning-based optimization techniques, could potentially offer even greater performance gains. The findings of this research open up multiple avenues for future explorations, suggesting that the field of coaxial rotor optimization is rich with possibilities for innovations.

Finally, this research has successfully validated the ROTARE code and demonstrated its effectiveness in optimizing coaxial rotor systems. The research has provided a detailed analysis of both operational and geometric optimization strategies, identifying key factors that influence rotor performance. While the study has made significant progress in understanding and improving coaxial rotor designs, it also underscores the complexity of the task and the need for integrated optimization strategies that consider all aspects of rotor design. This work lays the foundation for future research, which may explore alternative or more advanced methods to achieve even greater efficiency and performance in coaxial rotor systems.

6.1 Further perspectives and future improvement suggestions

6.1.1 Optimal thrust distribution strategy

One of the most promising areas for future research lies in developing an optimal thrust distribution strategy along the blade span. The key to this approach is to explore several strategic thrust distributions, which could include:

- **Concentration of thrust at the extremities:** By concentrating thrust generation towards the blade extremities, particularly near the tips, the rotor could achieve higher aerodynamic efficiency. This strategy leverages the higher relative velocities at the blade tips, where lift generation is more effective. However, care must be taken to avoid excessive flow acceleration that could reduce propulsive efficiency.
- **Reduced thrust near the hub:** Another strategy could involve minimizing or eliminating thrust generation near the hub of the upper rotor. This approach would reduce the mechanical losses associated with thrust generation at lower radii, where aerodynamic efficiency is typically lower due to higher induced drag and flow complexities. By focusing thrust generation away from the hub, the rotor could achieve a more balanced and efficient operation.
- **Equidistributed thrust along the blade span:** Instead of concentrating thrust in specific regions, an alternative strategy could involve distributing thrust more evenly along the blade span. This approach could lead to a more balanced load distribution and potentially reduce the mechanical stress on the blades, improving overall system durability and performance.
- **Exploration of various thrust distribution profiles:** Various distribution profiles such as linear, parabolic, hyperbolic, and exponential could be investigated to determine their impact on rotor performance. A linear distribution would involve a steady increase or decrease in thrust along the blade span, while a parabolic or hyperbolic distribution might emphasize the thrust in certain regions more intensely. Exponential distributions could also be explored for their potential to fine-tune the balance between thrust efficiency and mechanical stress. Each of these profiles would need to be analyzed through computational simulations and possibly experimental tests to identify the most effective strategy.

Each of these strategies could be explored through detailed simulations and experimental validation to determine the most effective thrust distribution pattern. Once an optimal thrust distribution is identified, it would directly inform the design of the chord distribution along the blade, allowing for a tailored chord profile that maximizes aerodynamic efficiency. The integration of this optimized chord distribution with the optimal twist profile could then lead to significant performance improvements in coaxial rotor systems.

6.1.2 Integration of multiple airfoil profiles

Another promising direction for future research is the introduction of multiple airfoil profiles along the blade span. Currently, the blades analyzed in this research are designed with a constant airfoil profile, which, while simplifying the design and manufacturing processes, may limit the potential for performance optimization.

- **High-lift airfoil at the tips:** One potential improvement could involve incorporating a high-lift airfoil at the blade tips. This strategy would take advantage of the higher relative velocities and potential for increased lift generation at the tips, contributing to more efficient thrust production. The use of a high-lift airfoil could also help in delaying flow separation and improving performance at high angles of attack.
-

- **Optimized airfoils for different spanwise regions:** The blade span could be divided into segments, each optimized with a different airfoil profile tailored to the specific aerodynamic conditions encountered in that region. For example, the root region, which experiences lower Reynolds numbers and complex flow structures, could benefit from an airfoil designed to handle these conditions more effectively. Meanwhile, the mid-span could be optimized for maximum lift-to-drag ratio, and the tip could be designed to minimize induced drag and tip vortex formation.

By integrating multiple airfoil profiles along the blade span, it may be possible to create a blade design that is better suited to the varying aerodynamic conditions experienced across the rotor, thereby improving overall performance.

6.1.3 Fixed pitch between upper and lower rotors

A third potential improvement, which offers both technical and economic advantages, is the consideration of a fixed pitch configuration between the upper and lower rotors, as opposed to the variable pitch strategy used in this research. While the variable pitch allows for more precise control of rotor performance across different operational conditions, it also introduces complexity in both the design and manufacturing processes.

- **Iterative process for optimal fixed pitch:** The challenge with adopting a fixed pitch strategy lies in identifying the optimal pitch angles for both rotors that maximize efficiency and performance under typical operating conditions. This would require an iterative optimization process, where the performance of different fixed pitch configurations is evaluated and compared to determine the most effective setup.
- **Simplified manufacturing and cost reduction:** A significant advantage of a fixed pitch design is the simplification of the rotor system, which could lead to easier manufacturing and assembly processes. By eliminating the need for variable pitch mechanisms, the overall system could be made more robust, reducing the potential for mechanical failure and lowering production costs. If it can be shown that a fixed pitch configuration does not significantly reduce performance, this strategy could become a viable alternative for future rotor designs.

This approach, although potentially less flexible in operation, could offer a more practical and cost-effective solution for rotor systems, especially in applications where the operational conditions are relatively stable and do not require frequent adjustments to the pitch settings.

Appendix A

Appendix

Blade SAB 280 mm

- Blade length = 280 mm
- Blade chord = 25 mm
- Airfoil thickness = 3.5 mm = 14% of blade chord
- Closest airfoil on airfoil tools database : Selig S8035 [9]



S8035 for RC aerobatic 14% thick (s8035-il)
S8035 for RC aerobatic 14% thick - Selig S8035 low Reynolds number airfoil

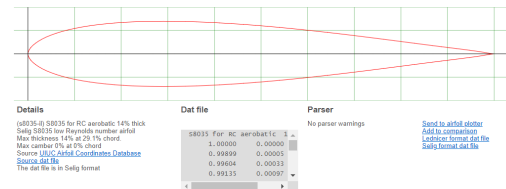


Figure A.1: Blade SAB 280 mm [6] and closest airfoil shape S8035 [9].

Blade 3 stars BL450 325 mm

- Blade length = 325 mm
- Blade chord = 32 mm
- Airfoil thickness = 4.2 mm = 13.1% of blade chord
- Closest airfoil on airfoil tools database : Gottingen GOE 411 [8]



GOE 411 AIRFOIL (goe411-il)
GOE 411 AIRFOIL - Gottingen 411 airfoil

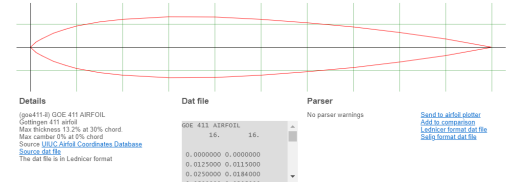


Figure A.2: Blade BL450 325 mm [31] and closest airfoil shape Gottingen GOE 411 [8].

Blade ALZRC 325 mm

- Blade length = 325 mm
- Blade chord = 32.5 mm
- Airfoil thickness = 4 mm = 12.3% of blade chord
- Closest airfoil on airfoil tools database : Eppler E171 [7]



(Dicke 12.28%) (e171-il)
(Dicke 12.28%) - Eppler E171 low Reynolds number airfoil

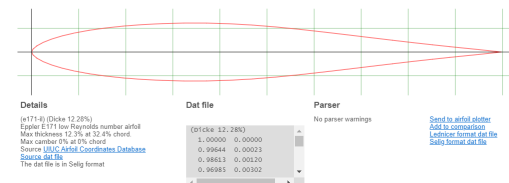


Figure A.3: Blade ALZRC 325 mm [5] and closest airfoil shape Eppler E171 [7].

Blade ALZRC 380 mm

- Blade length = 380 mm
- Blade chord = 33.5 mm
- Airfoil thickness = 4.5 mm = 13.4% of blade chord
- Closest airfoil on airfoil tools database : St. CYR 172 (Royer) [10]



St. CYR 172 (Royer) (stcyr172-il)
 St. CYR 172 (Royer) - St. CYR 172 (Royer) airfoil

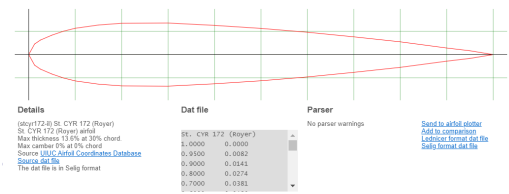


Figure A.4: Blade ALZRC 380 mm [4] and closest airfoil shape St. CYR 172 [10].

Appendix B

Results

SAB 280mm

Table B.1: Summary of the RPM and collective pitch variations for the upper and lower rotors across the full range of configurations for the blade SAB280.

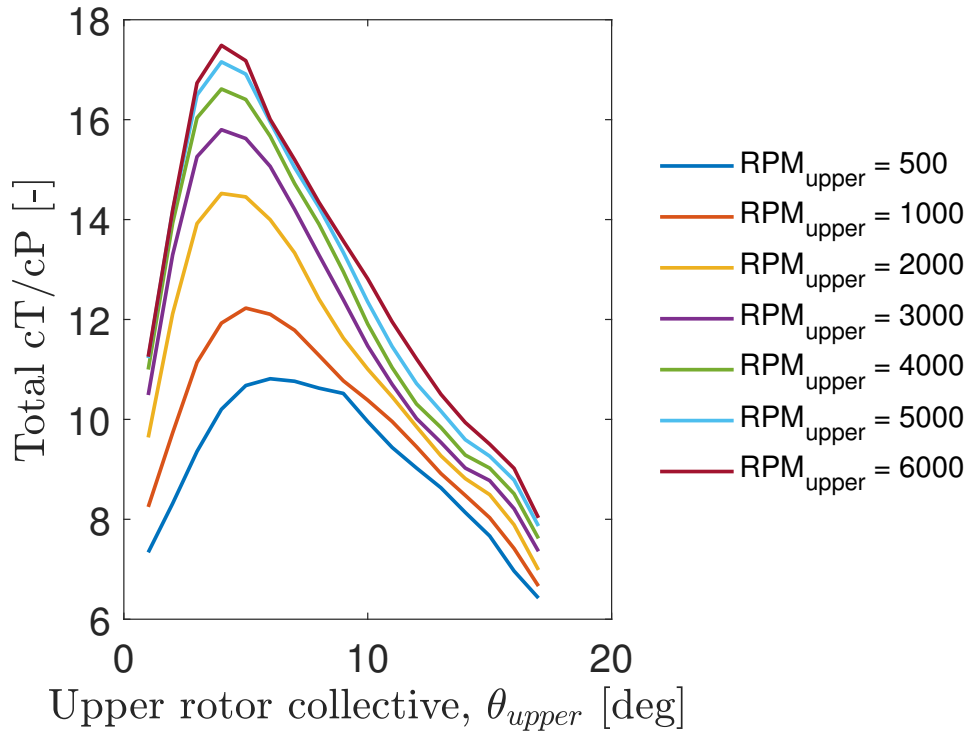
Upper Rotor RPM	Upper Rotor Collective θ_{upper} [deg]	Lower Rotor Collective θ_{lower} [deg]	Lower Rotor RPM
500	1	10.3916	294.2832
500	2	11.8442	282.0104
500	3	13.0930	288.6487
500	4	14.0930	303.9729
500	5	13.7499	344.6035
500	6	14.7499	356.2709
500	7	14.8442	380.8763
500	8	14.8812	386.8616
500	9	14.3200	399.1272
500	10	14.8565	403.7246
500	11	14.8632	425.5617
500	12	14.3200	458.7896
500	13	14.4232	478.8303
500	14	14.8698	485.4513
500	15	14.3632	519.6766
500	16	14.8532	535.0739
500	17	13.0930	619.2129
1000	1	10.2916	528.3429
1000	2	11.6368	515.1961
1000	3	12.8442	532.4672
1000	4	13.6368	571.4128
1000	5	13.6499	638.4839
1000	6	14.7499	665.2612
1000	7	14.8463	718.8142

Upper Rotor RPM	Upper Rotor Collective θ_{upper} [deg]	Lower Rotor Collective θ_{lower} [deg]	Lower Rotor RPM
1000	8	14.8498	760.1575
1000	9	14.8450	795.6993
1000	10	14.8756	828.3778
1000	11	14.8896	867.7657
1000	12	14.8901	909.9969
1000	13	14.8932	949.3197
1000	14	15.0991	976.8133
1000	15	15.1930	1013.7743
1000	16	15.2930	1044.7533
1000	17	14.8125	1087.0019
2000	1	9.6499	903.2834
2000	2	10.9929	901.5761
2000	3	12.0930	950.5796
2000	4	13.3916	1003.7925
2000	5	14.0930	1099.2458
2000	6	14.6368	1205.9546
2000	7	14.8442	1337.0592
2000	8	15.2256	1460.0226
2000	9	15.3916	1573.9676
2000	10	15.4118	1666.0970
2000	11	15.4640	1740.7983
2000	12	15.8442	1788.5824
2000	13	15.8671	1867.9030
2000	14	15.9745	1943.0975
2000	15	16.0930	1985.5619
2000	16	16.5000	2044.7149
2000	17	16.4157	2104.0077
3000	1	9.0930	1274.0240
3000	2	10.2916	1304.5969
3000	3	11.8442	1350.7609
3000	4	13.0930	1438.6825
3000	5	14.1830	1557.3086
3000	6	14.6368	1720.2183
3000	7	15.1456	1905.8121
3000	8	15.5579	2103.6022
3000	9	16.0930	2249.7937
3000	10	16.3931	2428.7612
3000	11	18.0930	2358.8337
3000	12	18.1930	2468.5506
3000	13	18.4328	2575.5439

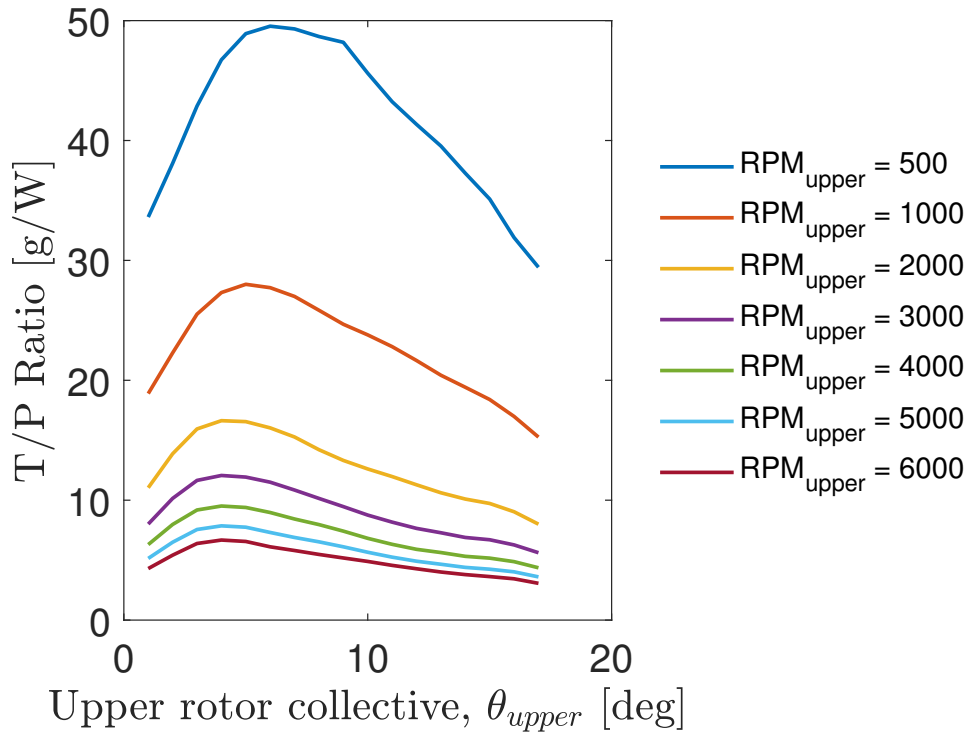
Upper Rotor RPM	Upper Rotor Collective θ_{upper} [deg]	Lower Rotor Collective θ_{lower} [deg]	Lower Rotor RPM
3000	14	18.3926	2677.5955
3000	15	18.3543	2767.2941
3000	16	18.2646	2843.4956
3000	17	18.1937	2921.6072
4000	1	9.0930	1668.7851
4000	2	10.0930	1742.2171
4000	3	11.6368	1811.1760
4000	4	13.0930	1901.5282
4000	5	14.0930	2046.1594
4000	6	14.6368	2249.5875
4000	7	15.1125	2480.2769
4000	8	16.1930	2645.0945
4000	9	18.0930	2673.6409
4000	10	18.0930	2930.5166
4000	11	16.3200	3429.7546
4000	12	16.4123	3597.2882
4000	13	16.4640	3729.2267
4000	14	16.5640	3877.5422
4000	15	16.5964	4012.3020
4000	16	16.6164	4121.1378
4000	17	16.6664	4228.3919
5000	1	8.7442	2161.7538
5000	2	10.3916	2184.1043
5000	3	12.0930	2268.7883
5000	4	13.6368	2341.0988
5000	5	14.2916	2518.2339
5000	6	14.8442	2751.7810
5000	7	14.9911	2999.6683
5000	8	16.1371	3229.5878
5000	9	16.2769	3572.9256
5000	10	16.3930	3900.9762
5000	11	16.4016	4256.8255
5000	12	16.4216	4486.8214
5000	13	16.4640	4678.6358
5000	14	16.4723	4868.4847
5000	15	16.5784	5045.0594
5000	16	16.6368	5186.9655
5000	17	16.6552	5280.3242
6000	1	8.7442	2609.4269
6000	2	10.3916	2565.2078

Upper Rotor RPM	Upper Rotor Collective θ_{upper} [deg]	Lower Rotor Collective θ_{lower} [deg]	Lower Rotor RPM
6000	3	12.0930	2646.1428
6000	4	13.6368	2770.7953
6000	5	14.5368	2971.6027
6000	6	15.3369	3234.6830
6000	7	15.4640	3533.5514
6000	8	16.0930	3802.3995
6000	9	16.3930	4153.3267
6000	10	16.4216	4618.4031
6000	11	16.4640	5065.4423
6000	12	16.5611	5353.7639
6000	13	16.6368	5583.5868
6000	14	16.6427	5815.3891
6000	15	16.6668	6032.9378
6000	16	16.6968	6211.2447
6000	17	16.7168	6367.4224

BL450 325mm

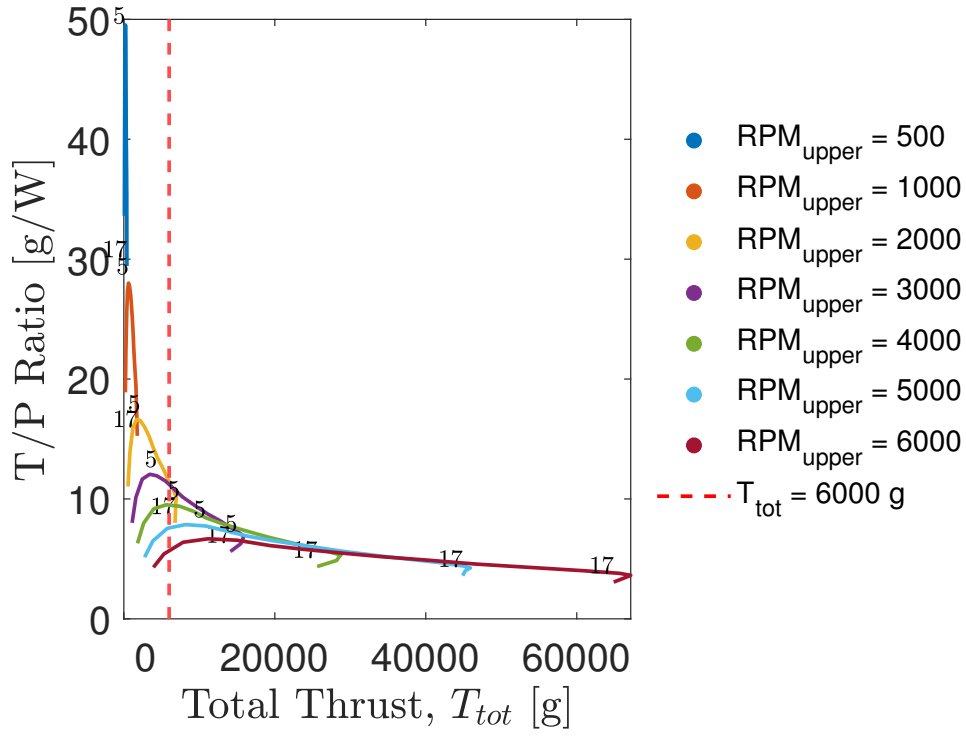


(a) c_T/c_P as a function of upper rotor collective pitch angle for $[RPM = 500 - 6000]$.

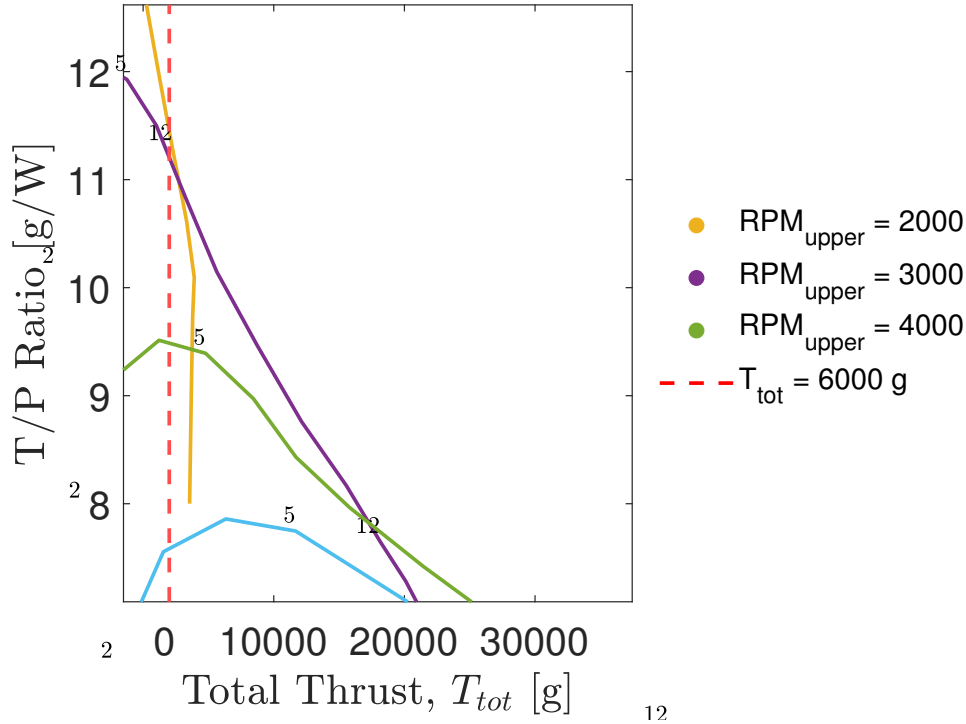


(b) Thrust-to-power ratio T/P as a function of upper rotor collective pitch angle for $[RPM = 500 - 6000]$.

Figure B.1: Variation of c_T/c_P and T/P with upper rotor collective pitch for the BL450 325mm blade. Blade parameters: $L = 325$ mm, $c = 32$ mm, airfoil: Gottingen GOE 411, $r_0 = 100$ mm, $r_{end} = 425$ mm.

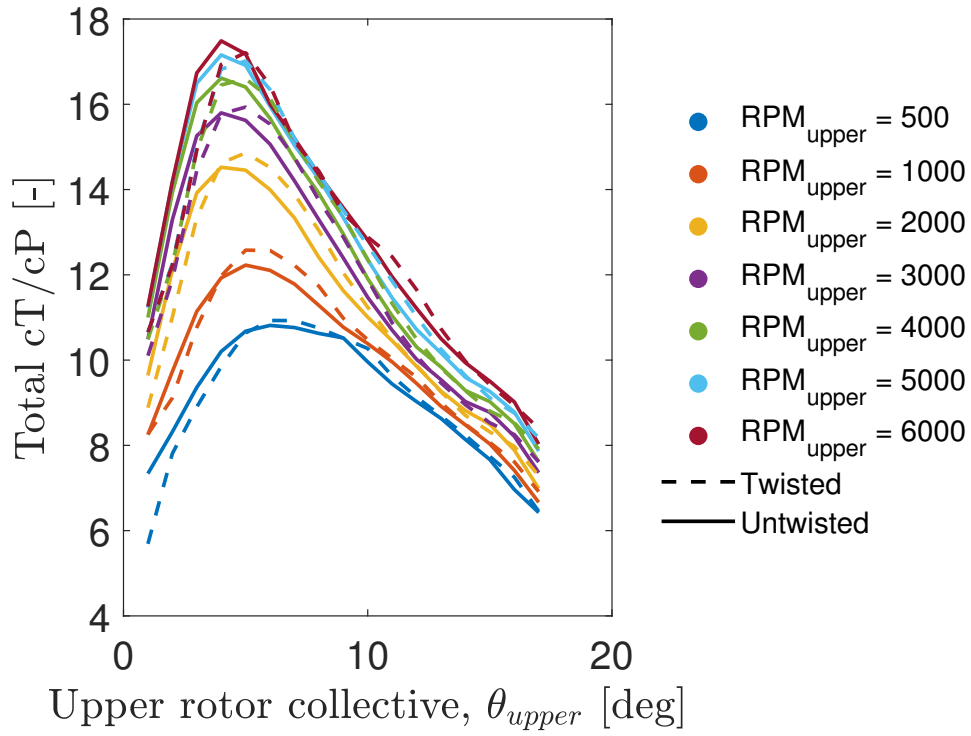


(a) Thrust-to-power ratio T/P as a function of total thrust for $[RPM = 500 - 6000]$.

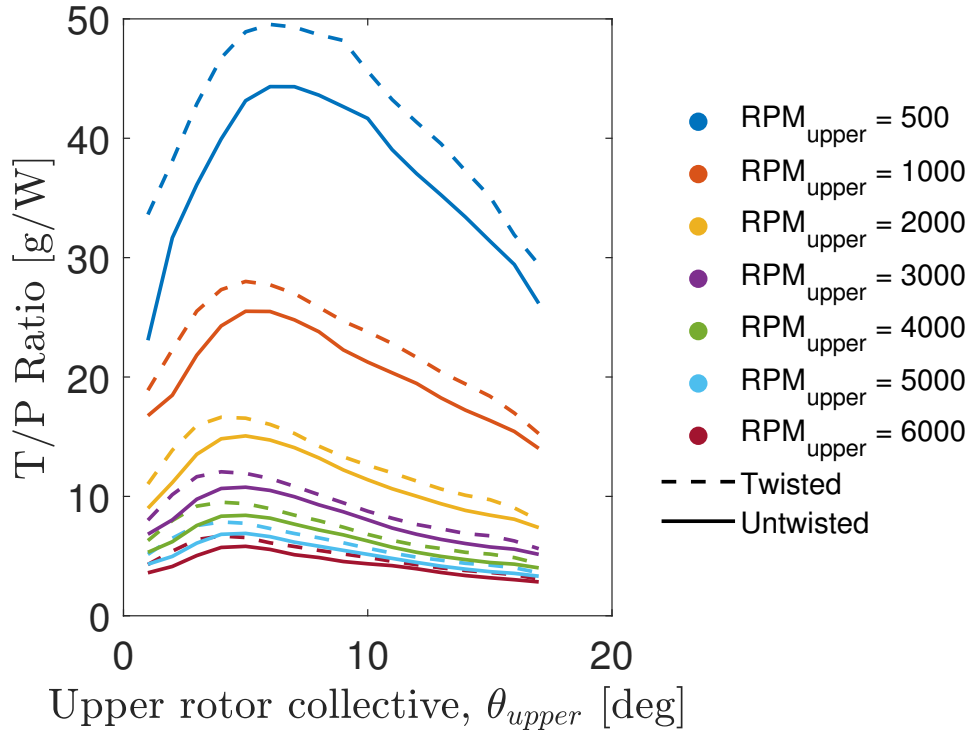


(b) Zoomed view of thrust-to-power ratio T/P as a function of total thrust.

Figure B.2: Thrust-to-power ratio T/P for the BL450 325mm blade at $\theta_{upper} = 1^\circ - 17^\circ$. Blade parameters: $L = 325$ mm, $c = 32$ mm, airfoil: Gottingen GOE 411, $r_0 = 100$ mm, $r_{end} = 425$ mm.

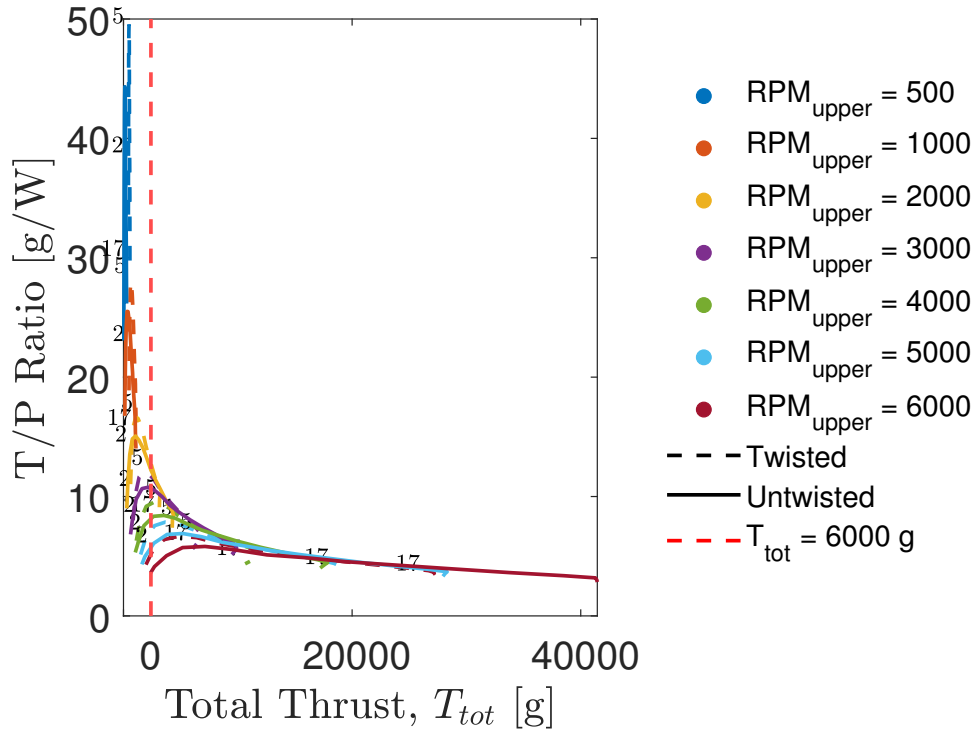


(a) c_T/c_P as a function of upper rotor collective pitch angle for $[RPM = 500 - 6000]$.

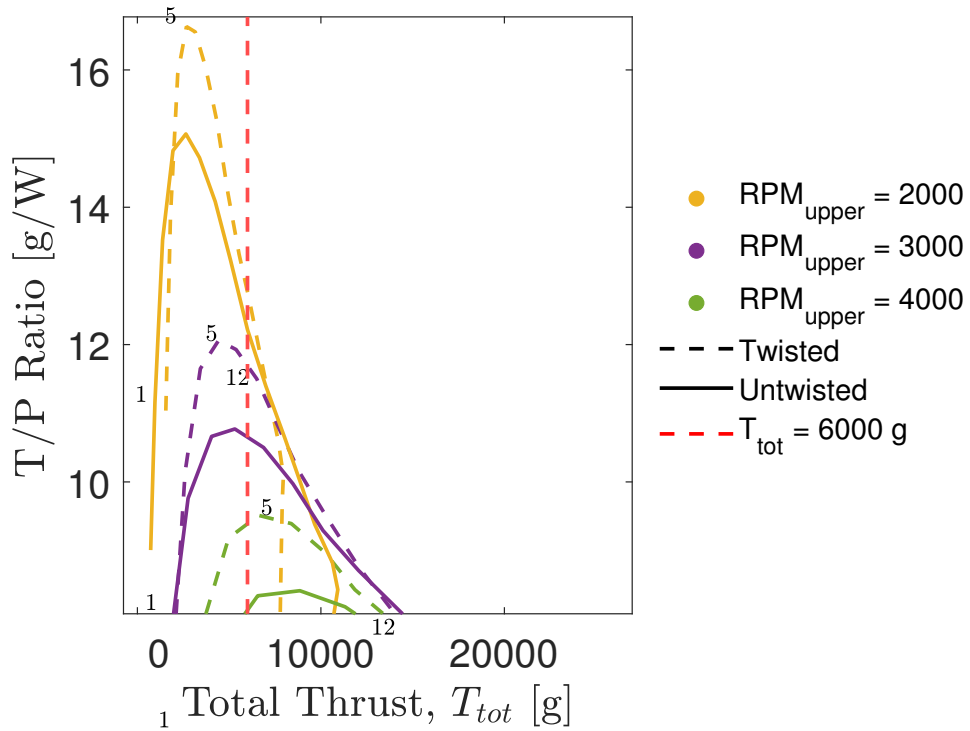


(b) Thrust-to-power ratio T/P as a function of upper rotor collective pitch angle for $[RPM = 500 - 6000]$.

Figure B.3: c_T/c_P and T/P variation for the BL450 blade with twisted blade configuration. Blade parameters: $L = 325$ mm, $c = 32$ mm, airfoil: Gottingen GOE 411, $r_0 = 100$ mm, $r_{end} = 425$ mm.



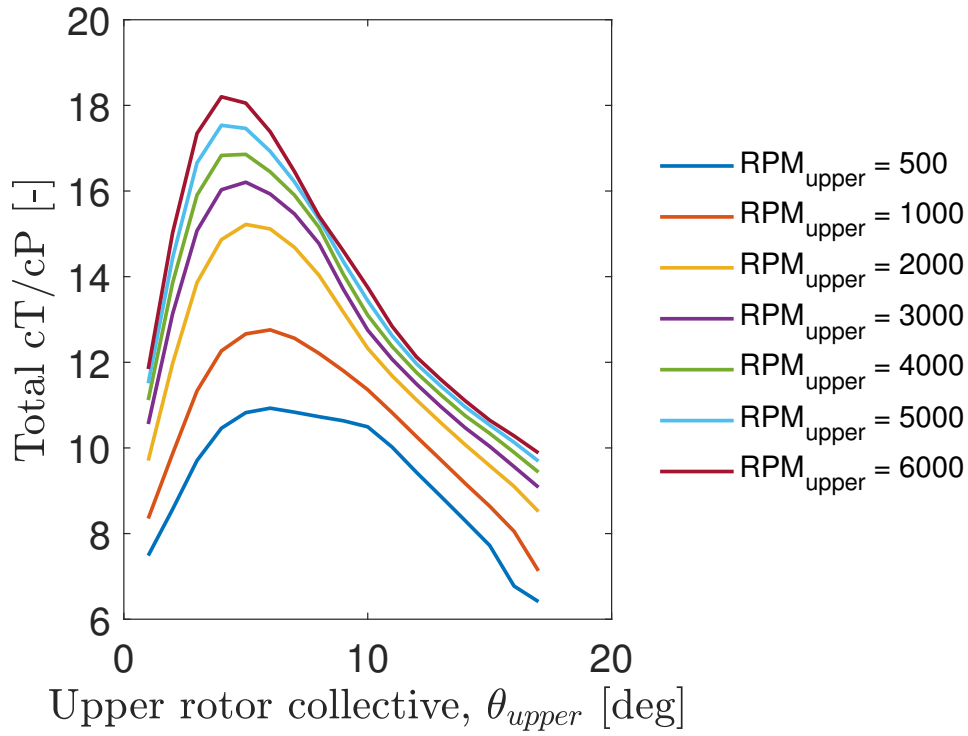
(a) Thrust-to-power ratio T/P as a function of total thrust for [$RPM = 500 - 6000$].



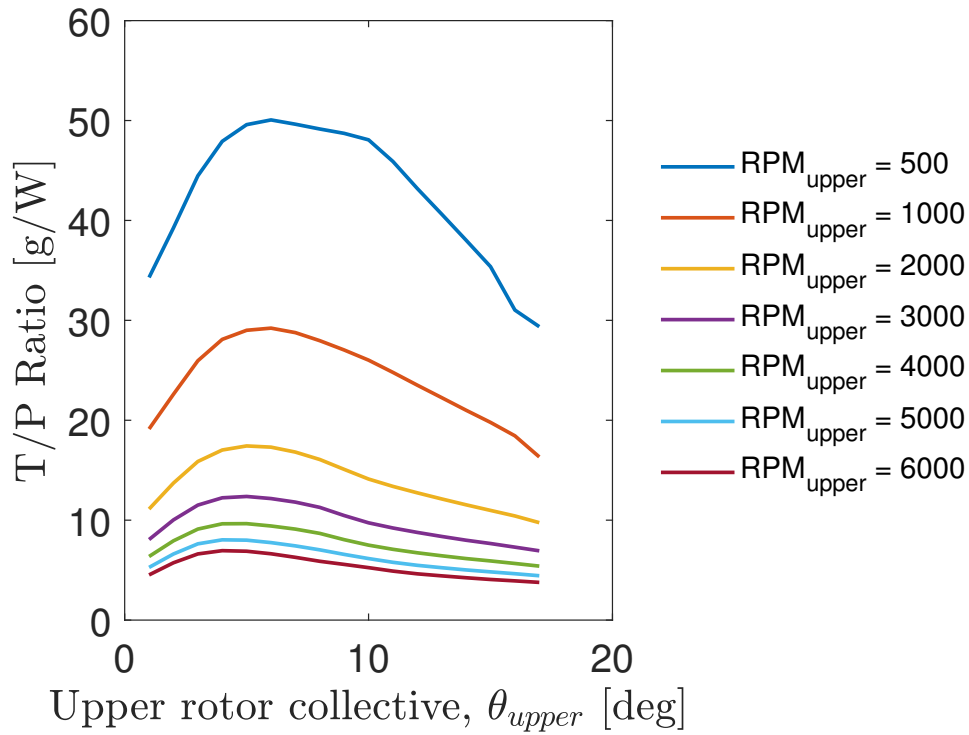
(b) Zoomed view of thrust-to-power ratio T/P as a function of total thrust.

Figure B.4: Performance improvement with twisted blade configuration for the BL450 325mm blade. Blade parameters: $L = 325$ mm, $c = 32$ mm, airfoil: Gottingen GOE 411, $r_0 = 100$ mm, $r_{end} = 425$ mm. The numbers 1 to 17 on the curves correspond to the collective pitch angles θ_{upper} of the upper rotor.

ALZRC 325mm

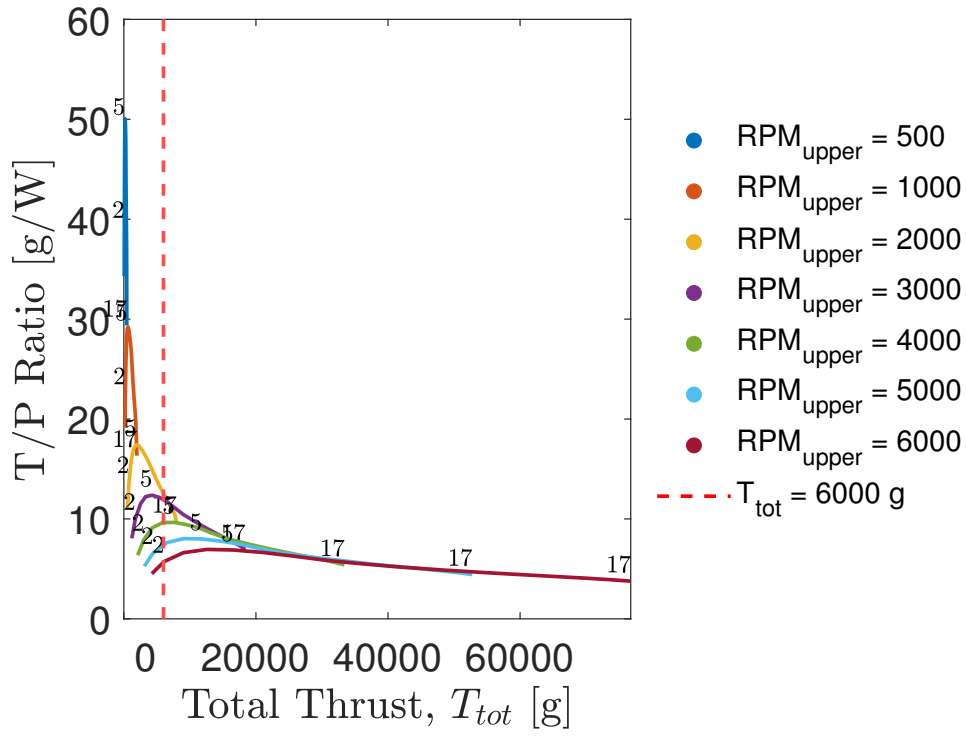


(a) c_T/c_P as a function of upper rotor collective pitch angle for $[RPM = 500 - 6000]$.

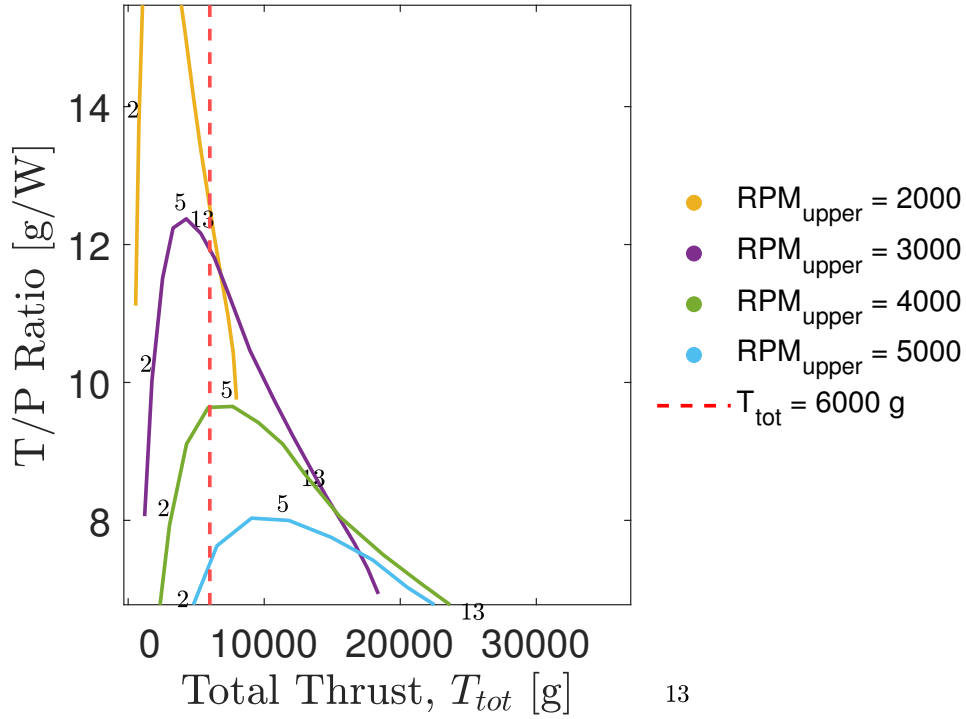


(b) Thrust-to-power ratio T/P as a function of upper rotor collective pitch angle for $[RPM = 500 - 6000]$.

Figure B.5: c_T/c_P and T/P variations for the ALZRC 325mm blade. Blade parameters: $L = 325$ mm, $c = 32.5$ mm, airfoil: Eppler E171, $r_0 = 100$ mm, $r_{end} = 425$ mm.

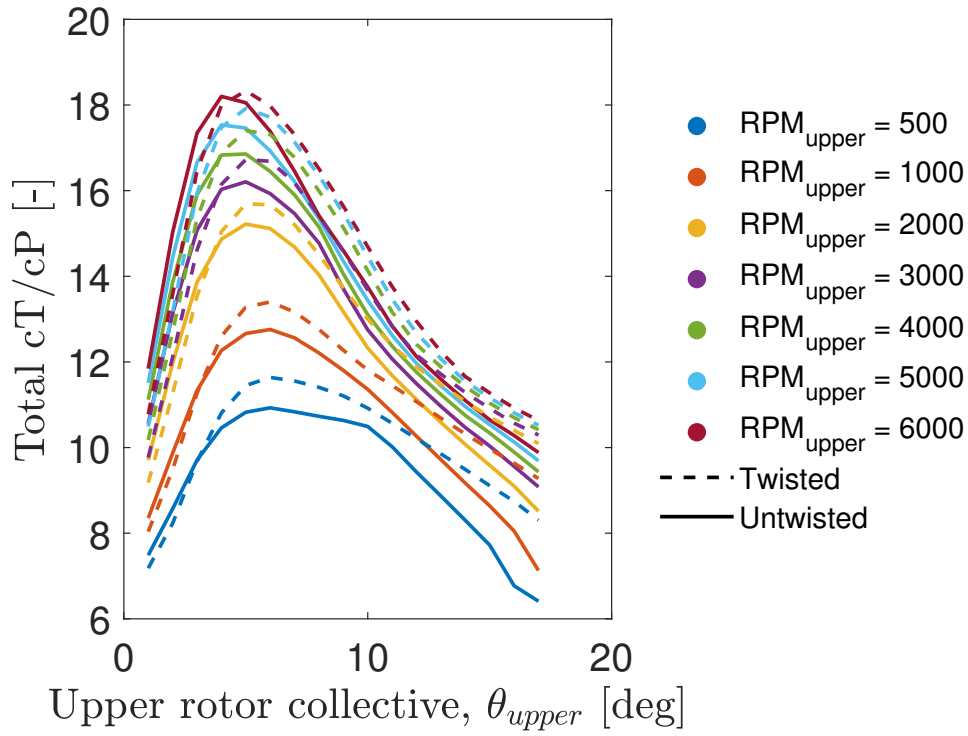


(a) Thrust-to-power ratio T/P as a function of total thrust for $[RPM = 500 - 6000]$.

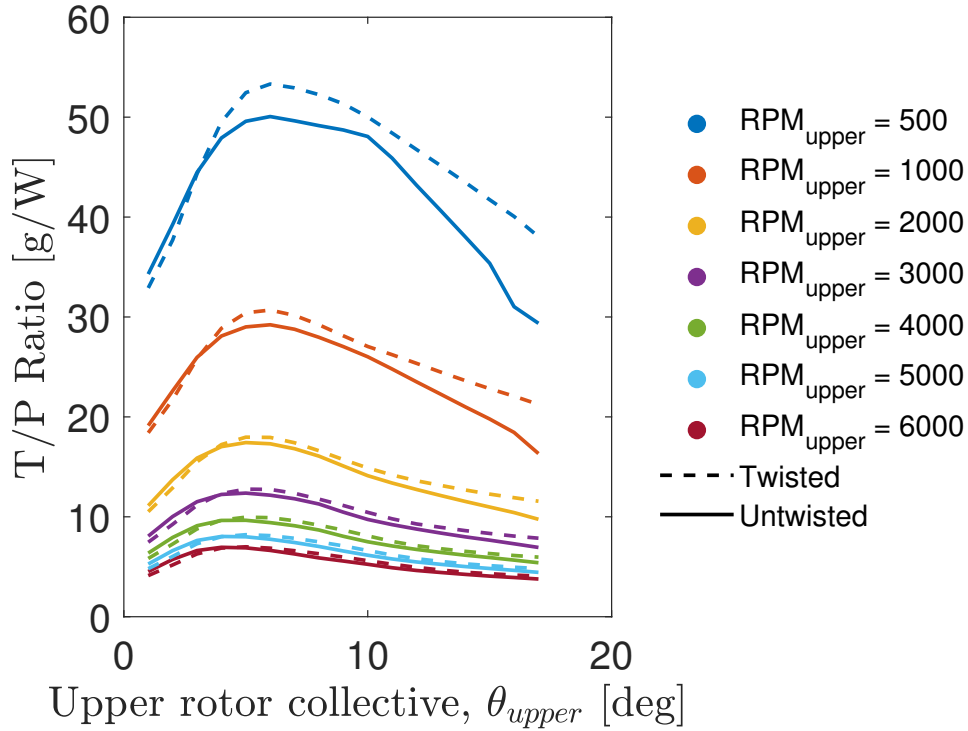


(b) Zoomed view of thrust-to-power ratio T/P as a function of total thrust.

Figure B.6: Thrust-to-power ratio T/P for the ALZRC 325mm blade at $\theta_{upper} = 1^\circ - 17^\circ$. Blade parameters: $L = 325$ mm, $c = 32.5$ mm, airfoil: Eppler E171, $r_0 = 100$ mm, $r_{end} = 425$ mm.

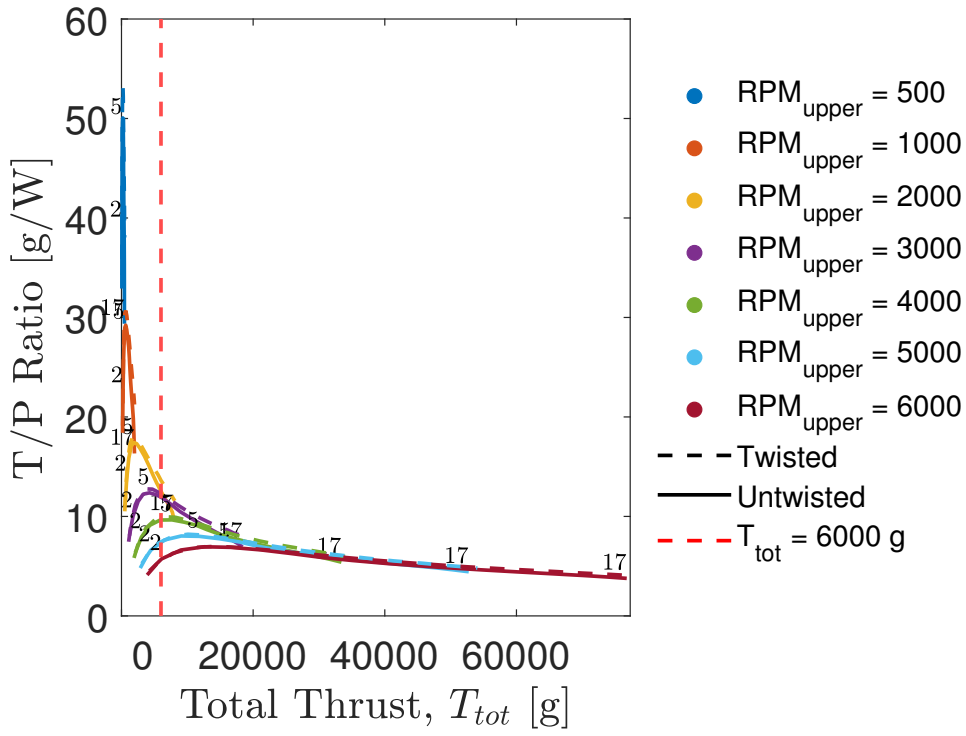


(a) c_T/c_P as a function of upper rotor collective pitch angle for $[RPM = 500 - 6000]$.

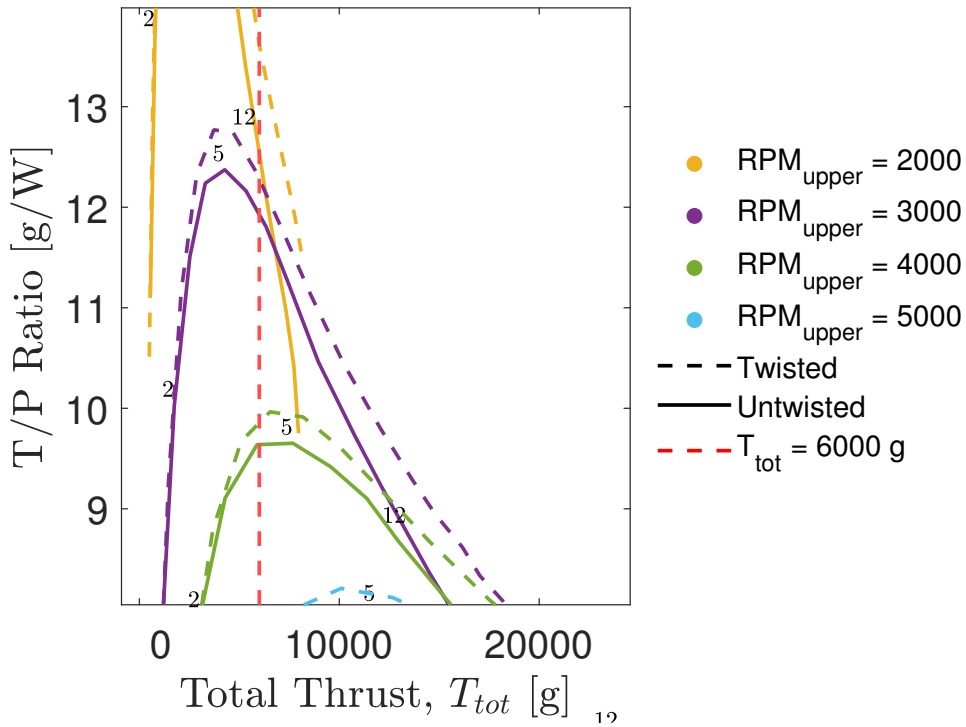


(b) Thrust-to-power ratio T/P as a function of upper rotor collective pitch angle for $[RPM = 500 - 6000]$.

Figure B.7: c_T/c_P and T/P variation for the ALZRC 325mm blade with twisted blade configuration. Blade parameters: $L = 325$ mm, $c = 32.5$ mm, airfoil: Eppler E171, $r_0 = 100$ mm, $r_{end} = 425$ mm.



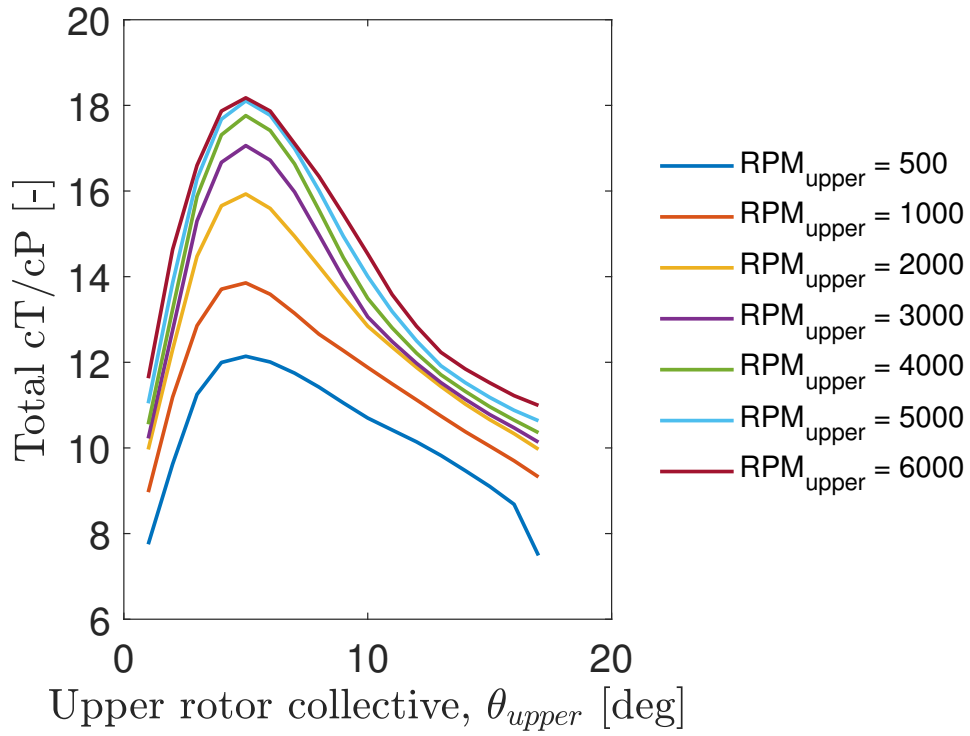
(a) Thrust-to-power ratio T/P as a function of total thrust for $[RPM = 500 - 6000]$.



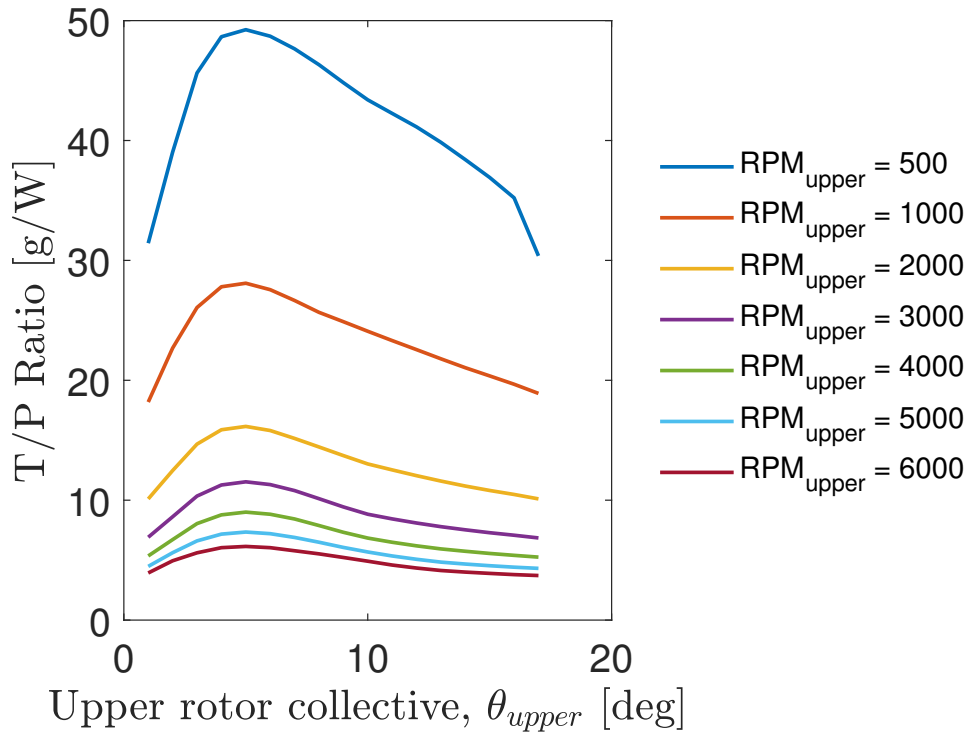
(b) Zoomed view of thrust-to-power ratio T/P as a function of total thrust.

Figure B.8: Performance improvement with twisted blade configuration for the ALZRC 325mm blade. Blade parameters: $L = 325$ mm, $c = 32.5$ mm, airfoil: Eppler E171, $r_0 = 100$ mm, $r_{end} = 425$ mm. The numbers 1 to 17 on the curves correspond to the collective pitch angles θ_{upper} of the upper rotor.

ALZRC 380 mm

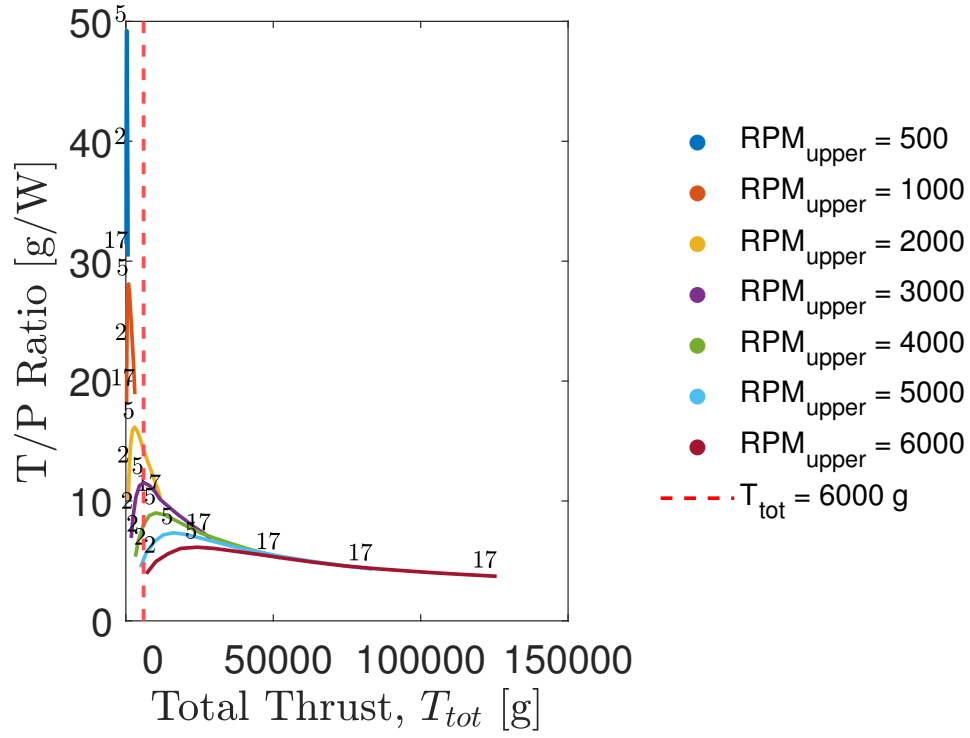


(a) c_T/c_P as a function of upper rotor collective pitch angle for $[RPM = 500 - 6000]$.

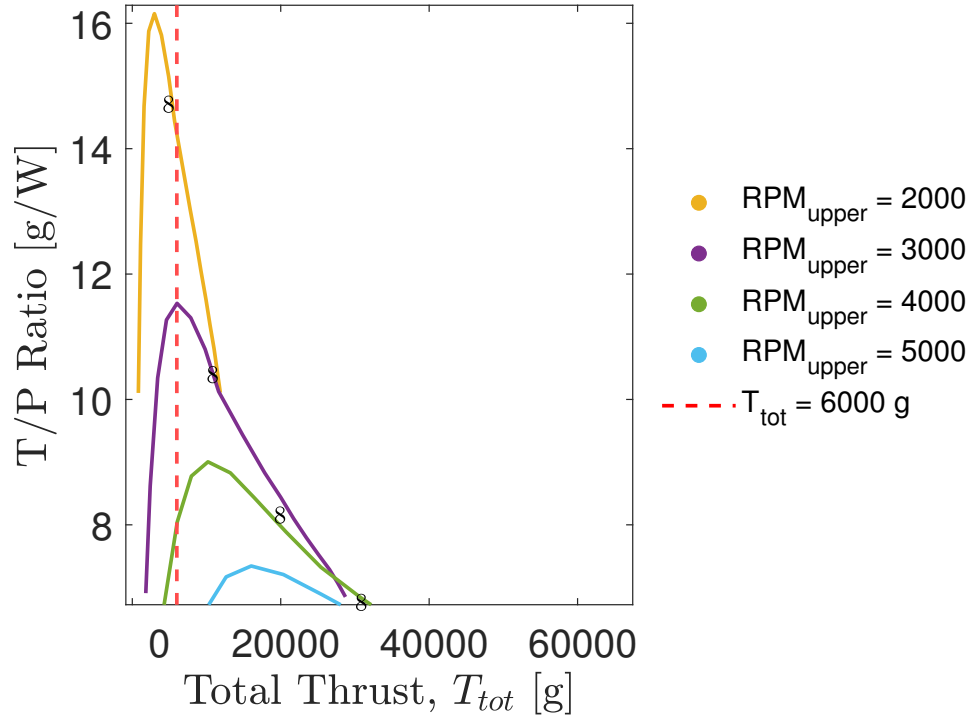


(b) Thrust-to-power ratio T/P as a function of upper rotor collective pitch angle for $RPM = 500 - 6000$.

Figure B.9: c_T/c_P and T/P variation for the ALZRC 380mm blade. Blade parameters: $L = 380\text{mm}$, $c = 33.5\text{mm}$, airfoil: St. CYR 172 (Royer), $r_0 = 100\text{mm}$, $r_{end} = 480\text{mm}$.

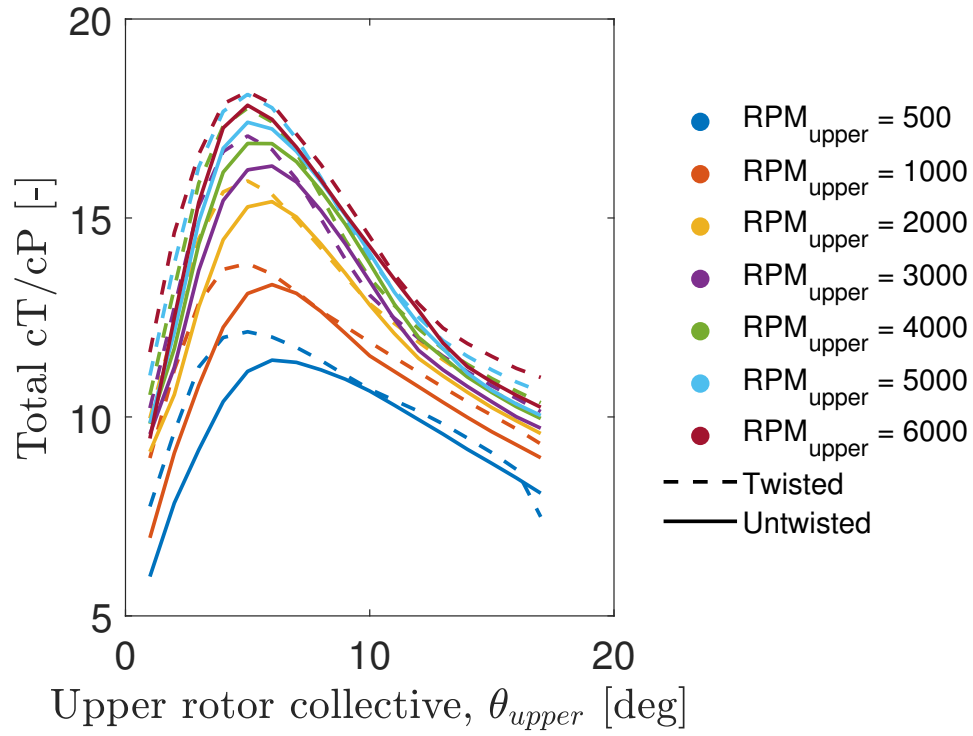


(a) Thrust-to-power ratio T/P as a function of total thrust for $[RPM = 500 - 6000]$.

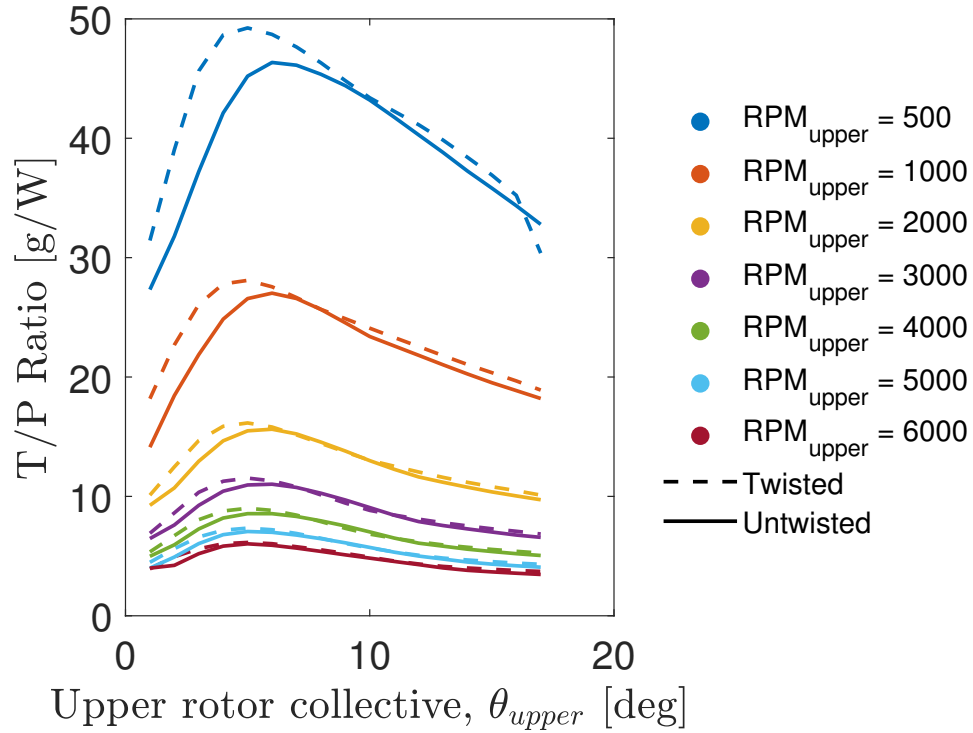


(b) Zoomed view of thrust-to-power ratio T/P as a function of total thrust.

Figure B.10: Thrust-to-power ratio T/P variation for the ALZRC 380mm blade at $\theta_{upper} = 1^\circ - 17^\circ$. Blade parameters: $L = 380$ mm, $c = 33.5$ mm, airfoil: St. CYR 172 (Royer), $r_0 = 100$ mm, $r_{end} = 480$ mm.

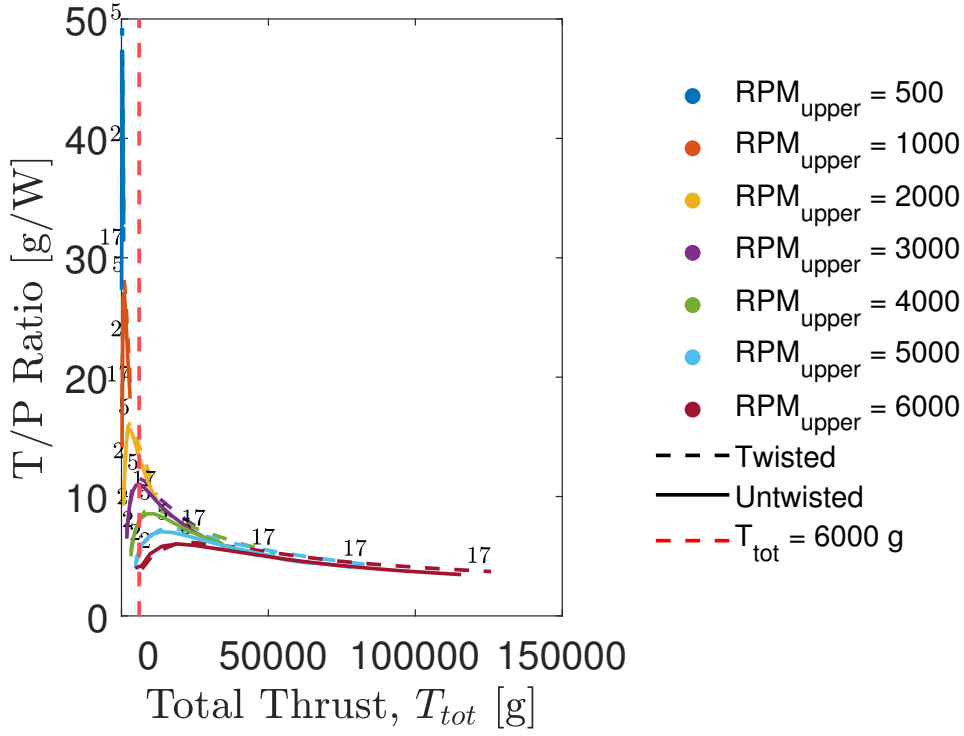


(a) c_T/c_P as a function of upper rotor collective pitch angle for $[RPM = 500 - 6000]$.

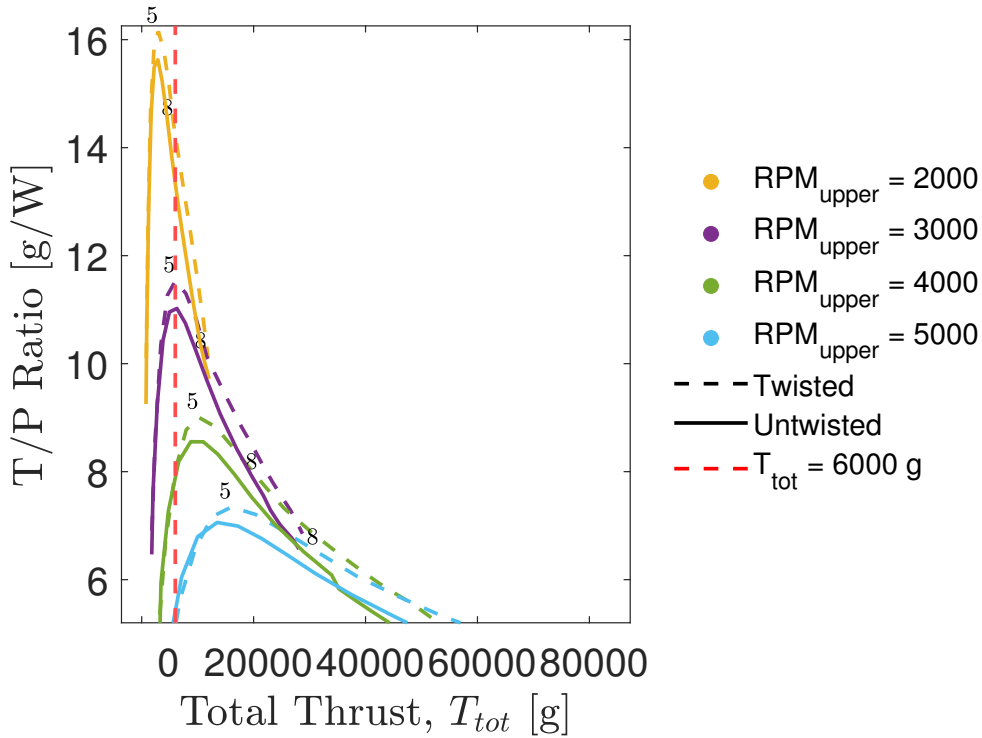


(b) Thrust-to-power ratio T/P as a function of upper rotor collective pitch angle for $[RPM = 500 - 6000]$.

Figure B.11: c_T/c_P and T/P variation for the ALZRC 380mm blade with twisted blade configuration. Blade parameters: $L = 380$ mm, $c = 33.5$ mm, airfoil: St. CYR 172 (Royer), $r_0 = 100$ mm, $r_{end} = 480$ mm.



(a) Thrust-to-power ratio T/P as a function of total thrust for $[RPM = 500 - 6000]$.



(b) Zoomed view of thrust-to-power ratio T/P as a function of total thrust.

Figure B.12: Performance improvement with twisted blade configuration for the ALZRC 380mm blade. Blade parameters: $L = 380\text{mm}$, $c = 33.5\text{mm}$, airfoil: St. CYR 172 (Royer), $r_0 = 100\text{mm}$, $r_{\text{end}} = 480\text{mm}$. The numbers 1 to 17 on the curves correspond to the collective pitch angles θ_{upper} of the upper rotor.

Bibliography

- [1] Airfoil tools. <http://www.airfoiltools.com/>. Accessed: 2024-08-17.
- [2] Kamov ka-27 (otan helix). <https://www.avmil.net/v3/kb/aircraft/show/2483/kamov-ka-27-otan-helix>. Accessed: 2024-08-17.
- [3] Kamov ka-52 alligator (otan hokum b). <https://www.avmil.net/v3/kb/aircraft/show/9727/kamov-ka-52-alligator-otan-hokum-b>. Accessed: 2024-08-17.
- [4] 1 paar 380 mm alzrc rc helikopteronderdelen glasvezel hoofdbladen. https://www.123materialen.com/products/1-paar-380-mm-alzrc-rc-helikopteronderdelen-glasvezel-hoofdbladen_1669328?gad_source=1&gclid=Cj0KCQjw2ou2BhCCARIsANAwM2Hl0W-kIuE3givgYc0qsRvJbBMft3Q_HgnSYrU48qMFM_LshyNgoWYaAlqTEALw_wcB, 2024. Accessed: 2024-08-19.
- [5] Freeday uk alzrc 325 mm carbon fiber main blades propeller props for devil 450 pro sport rigid fast align helicopter rc drone aircraft. <https://www.desertcart.co.zw/products/97318712-freeday-uk-alzrc-325-mm-carbon-fiber-main-blades-propeller-props-for-devil-450-pr>, 2024. Accessed: 2024-08-19.
- [6] Sab 280mm thunderbolt main blades - 280tb. https://www.hely-shop.co.uk/sab-280mm-thunderbolt-main-blades-280tb/?srsltid=AfmB0opyJqBcJ9LZ73meRiluUGFzi68P_P2_w83PesA3DFEAon6j6uAg, 2024. Accessed: 2024-08-19.
- [7] Airfoil Tools. E171 airfoil details. <http://airfoiltools.com/airfoil/details?airfoil=e171-il>, 2024. Accessed: 2024-07-31.
- [8] Airfoil Tools. Goe411 airfoil details. <http://airfoiltools.com/airfoil/details?airfoil=goe411-il>, 2024. Accessed: 2024-07-31.
- [9] Airfoil Tools. S8035 airfoil details. <http://airfoiltools.com/airfoil/details?airfoil=s8035-il>, 2024. Accessed: 2024-07-31.
- [10] Airfoil Tools. Stcyr172 airfoil details. <http://airfoiltools.com/airfoil/details?airfoil=stcyr172-il>, 2024. Accessed: 2024-07-31.
- [11] APC Propellers. Engineering information. <https://www.apcprop.com/technical-information/engineering/>, 2024. Accessed: 2024-08-07.
- [12] Avia Military Database. Kamov ka-10m. <https://www.avmil.net/v3/kb/aircraft/show/5750/kamov-ka-10m>, n.d. Accessed: 2024-07-23.
- [13] Albert Betz. Windmills in the light of modern research. Technical Memorandum 474, NACA, 1928.

- [14] David Biermann and Edwin P. Hartman. The aerodynamic characteristics of six full-scale propellers having different airfoil sections. Technical Report NACA-TR-650, NACA, Jan 1939. NTRS Document ID: 19930091725.
- [15] J. B. Brandt and M. S. Selig. Propeller performance data at low reynolds numbers. In *49th AIAA Aerospace Sciences Meeting including the New Horizons Forum and Aerospace Exposition*, Orlando, FL, 2011. American Institute of Aeronautics and Astronautics.
- [16] Tony Burton, Nick Jenkins, David Sharpe, and Ervin Bossanyi. *Wind Energy Handbook*. John Wiley & Sons, Chichester, UK, 2nd edition, 2011. Chapter7: Component design.
- [17] M. Drela and M.B. Giles. Viscous-inviscid analysis of transonic and low reynolds number airfoils. *AIAA Journal*, 25(10):1347–1355, 1987.
- [18] Mark Drela. Xfoil subsonic airfoil development system. <https://web.mit.edu/drela/Public/web/xfoil/>, 2024. Accessed: 2024-08-07.
- [19] S. Drzewiecki. *Théorie Générale de l’Hélice Propulsive*. Gauthier–Villars, Paris, 1920.
- [20] A. Gessow. Effect of rotor-blade twist and plan-form taper on helicopter hovering performance. Technical Note 1542, NACA, 1948.
- [21] A. Gessow and G. C. Myers. *Aerodynamics of the Helicopter*. MacMillan Co., New York, NY, 1952.
- [22] Alfred Gessow and Garry C. Myers. *Aerodynamics of the Helicopter*. Courier Corporation, 1985. pp. 99-120: Rotor Blade Motion.
- [23] Hermann Glauert. Airplane propellers. In William Frederick Durand, editor, *Aerodynamic Theory*. Springer Berlin Heidelberg, Berlin, Heidelberg, 1935.
- [24] Franklin D. Harris. An overview of coaxial rotorcraft technology. Technical Report NASA/TP–2010-216362, NASA, 2010.
- [25] Mostafa Hassanalian and Abdessattar Abdelkefi. Classifications, applications, and design challenges of drones: A review. *Progress in Aerospace Sciences*, 91, 05 2017.
- [26] Koen Hillewaert. Aerospace propulsion [course lecture], May 2023. Univertité de Liège.
- [27] Innovation Investment Opportunities. Space shots: First mars helicopter - nasa’s ingenuity. <https://innovationinvestmentopportunities.blogspot.com/2020/07/space-shots-first-mars-helicopter-nasas.html>, 2020. Accessed: 2024-07-23.
- [28] Muwanika Jdiobe, Kurt Rouser, Ryan Paul, and Austin Rouser. Validation of a wind tunnel propeller dynamometer for group 2 unmanned aircraft. *Applied Sciences*, 12(17):8908, 2022.
- [29] Wayne Johnson. *Helicopter Theory*. Dover Publications, 1980. pp. 373-400: Rotor Aerodynamics in Axial Flight.
- [30] Wayne Johnson. *Rotorcraft Aeromechanics*. Cambridge University Press, 2013. pp. 185-200: Blade Element Theory.

- [31] KDS RC Heli Shop. 1193-5 kds cf 325mm main blades. https://www.kds-rc-helishop.nl/index.php?id_product=513&rewrite=1193-5-kds-cf-325mm-main-blades&controller=product, n.d. Accessed: 2024-08-19.
- [32] Thomas Lambert. *Experimental and Numerical Analysis of Unsteady Rotating and Flapping Multi-Wing Systems*. PhD thesis, University of Liège, Liège, Belgium, 2024. To be published.
- [33] Thomas Lambert. ROTARE: Advanced blade element momentum theory (bemt) implementation. <https://tlambert.be/project/rotare/>, ongoing development. Accessed: June 2024.
- [34] J. G. Leishman and S. Ananthan. Aerodynamic optimization of a coaxial proprotor. In *American Helicopter Society 62nd Annual Forum Proceedings*, Phoenix, AZ, May 9–11 2006.
- [35] J. G. Leishman and M. Syal. Figure of merit definition for coaxial rotors. *Journal of the American Helicopter Society*, 53(3):290–300, July 2008.
- [36] J. Gordon Leishman. *Principles of Helicopter Aerodynamics*. Cambridge University Press, 2006. pp. 115-116: Blade Element Analysis.
- [37] J. Gordon Leishman. *Principles of Helicopter Aerodynamics*. Cambridge University Press, 2006.
- [38] J. Gordon Leishman. *Principles of Helicopter Aerodynamics*. Cambridge University Press, 2006. pp. 101-102: Coaxial Rotor Systems.
- [39] J. Gordon Leishman. *Principles of Helicopter Aerodynamics*. Cambridge University Press, 2006. pp. 55-61: Momentum Theory Analysis in Hovering Flight.
- [40] J. Gordon Leishman. *Principles of Helicopter Aerodynamics*. Cambridge University Press, 2006. pp. 141-145: Prandtl’s Tip-Loss Function.
- [41] J. Gordon Leishman. *Principles of Helicopter Aerodynamics*. Cambridge University Press, 2006. pp. 290-292: Blade Twist.
- [42] P.B.S. Lissaman. Low-reynolds-number airfoils. *Annual Review of Fluid Mechanics*, 15(1):223–239, 1983.
- [43] National Air and Space Museum. Early helicopter development. <https://airandspace.si.edu/explore-and-learn/topics/helicopters/>, 2024. Accessed: 2024-07-31.
- [44] National Air and Space Museum. Hiller xh-44 hiller-copter. https://airandspace.si.edu/collection-objects/hiller-xh-44-hiller-copter/nasm_A19530081000, n.d. Accessed: 2024-07-23.
- [45] Jean-Nicolas Passieux. Gyroplane labo. <http://jnpassieux.fr/www/html/GyroplaneLabo.php>, 2024. Accessed: 2024-08-17.
- [46] William Pearce. Dorand gyroplane g.20 / g.ii, 2015. Publisher: Old Machine Press. Accessed: 2024-08-17.
- [47] Michael S. Selig. Uiuc propeller data site. <https://m-selig.ae.illinois.edu/props/propDB.html>, 2022. University of Illinois at Urbana-Champaign, Department of Aerospace Engineering.

- [48] R. P. Sicard and K. Nguyen. Aerodynamic performance of coaxial rotors in forward flight. *Journal of Aircraft*, 53(3):645–657, 2016.
- [49] Conor W. Stahlhut and J. Gordon Leishman. Aerodynamic design optimization of proprotors for convertible-rotor concepts. pages 1–24. University of Maryland, May 2012.
- [50] W. Z. Stepniewski and C. N. Keys. *Rotary-Wing Aerodynamics*. Dover Publications, 1984. pp. 275-290: Rotor Performance.
- [51] G. A. Tokaty. *A History and Philosophy of Fluid Mechanics*. Foulis & Co., Henley-on-Thames, UK, 1971.
- [52] T. Valkov. Aerodynamic loads computation on coaxial hingeless helicopter rotors. In *28th Aerospace Sciences Meeting*, number AIAA 90-0070, Reno, NV, January 8–11 1990.
- [53] F. E. Weick. *Aircraft Propeller Design*. McGraw-Hill Book Co., Inc., New York, NY, 1930.
- [54] WikiMili. Kamov ka-8. https://wikimili.com/en/Kamov_Ka-8#Kamov_Ka-8.jpg, n.d. Accessed: 2024-07-23.